



UNIVERSITY OF ÉVORA

SCHOOL OF SCIENCE AND TECHNOLOGY

DEPARTMENT OF PHYSICS

**Modelling of volumetric solar receivers with
nanoparticle suspensions**

Tiago Emanuel Ramos Tidy

Supervision: Paulo Manuel Ferrão Canhoto, Ph.D.

Masters in Solar Energy Engineering

Dissertation

Évora, 2015



UNIVERSITY OF ÉVORA

SCHOOL OF SCIENCE AND TECHNOLOGY

DEPARTMENT OF PHYSICS

**Modelling of volumetric solar receivers with
nanoparticle suspensions**

Tiago Emanuel Ramos Tidy

Supervision: Paulo Manuel Ferrão Canhoto, Ph.D.

Masters in Solar Energy Engineering

Dissertation

Évora, 2015

“You never change things by fighting the existing reality. To change something, build a new model that makes the existing model obsolete.”

R. Buckminster Fuller

ACKNOWLEDGMENTS

I would like to express my gratitude to all who have directly or indirectly contributed in putting together this dissertation.

Firstly, I would like to express my sincere thanks and gratitude to my supervisor, Professor Paulo Canhoto, for his mentoring and feedback. The motivation he gave me to challenge myself and overcome many barriers must be recognized. I also acknowledge his constant availability, incentive and collaboration provided to this project, making these last few months an unforgettable experience.

I also gratefully thank the University of Évora and its Geophysics Centre for providing the space and necessary materials for this dissertation. The contribution of Sérgio Aranha from the physics department was of course invaluable and I am very grateful for the time and interest he invested in this project. Special thanks to Josué Figueira for all his dedication on the manufacturing and assembly of parts of the experimental apparatus. Dr. Miguel Potes also provided important equipment and helpful input and advice on the spectroradiometer functioning. I also thank Maria Helena from the chemistry department for providing indispensable equipment and for sharing her chemistry knowledge in the nanotechnology field.

I am very thankful to all my colleagues who shared the lab space with me, especially Germilly Barreto for helping me and motivating me to work harder and harder. I owe my sincere appreciation to my classmates and friends, who have supported, encouraged and guided me throughout my academic life. I would like to particularly thank Carlos Sousa for his truthful friendship and Cláudia Franco for her unconditional support and advice.

Finally, I would like to express my deepest gratitude to my family, in particular to my parents, for their extraordinary support and constant encouragement.

ABSTRACT

This work addresses the modelling of nanofluid-based volumetric receivers aiming the improvement of solar energy harvesting and conversion systems. A numerical heat transfer model (1-D) was developed to predict the energy gain in a non-flowing receiver, in which both receiver height and particles volume fraction were optimized. Various combinations of base fluids (water, mineral oils, ethylene glycol) and nanoparticles (graphite, carbon nanotubes) were considered by modelling their optical and thermodynamic properties. Specific characteristics and advantages of volumetric receivers were emphasized by comparing numerical results with those obtained for a surface-based receiver, and by experimental measurements. A two-dimensional numerical model was also developed to investigate the performance of a parallel plate volumetric receiver with a fully developed laminar flow under various operation conditions. It was found that a better performance was obtained when using solid particles of carbon nanotubes.

Keywords: Volumetric, direct absorption, nanofluid, volume fraction, performance, temperature profile.

RESUMO

Modelação de recetores solares volúmicos com nanopartículas suspensas

Este trabalho aborda a modelação de recetores volúmicos com nanofluidos tendo como objetivo o melhoramento de sistemas de captação e conversão de energia solar. Foi desenvolvido um modelo numérico de transferência de calor unidimensional para prever a energia ganha num recetor estagnado, onde a altura e a fração volúmica de partículas foram otimizadas. Várias combinações de fluidos (água, óleos minerais, etileno glicol) e nanopartículas (grafite, nanotubos de carbono) foram consideradas através da modelação das suas propriedades óticas e radiativas. As características específicas e vantagens dos recetores volúmicos foram destacadas através da comparação dos resultados numéricos com os obtidos num recetor de superfície, e através de medidas experimentais. Foi também desenvolvido um modelo numérico bidimensional para investigar o desempenho de um receptor volúmico com escoamento laminar e plenamente desenvolvido entre placas paralelas, sob várias condições de operação. Verificou-se que o melhor desempenho foi obtido usando partículas sólidas de nanotubos de carbono.

Palavras-Chave: Volumétrico, absorção direta, nanofluido, fração volúmica, desempenho, perfil de temperatura.

CONTENTS

List of Figures	ix
List of Tables	xi
Nomenclature	xiii
Acronyms	xvii
1. Introduction	1
1.1. Aim	5
1.2. Outline of the dissertation	5
2. Nanofluid preparation and properties	7
2.1. Preparation and stability	7
2.2. Thermodynamic and transport properties	9
2.3. Radiative properties	11
2.3.1. Experimental characterization of radiative properties	12
3. Nanofluid-based receiver modelling and optimization	15
3.1. Volumetric heat rate profile	16
3.1.1. Absorption efficiency	17
3.2. Temperature profile	17
3.3. Numerical model	18
3.3.1. Internal plane	20
3.3.2. Boundary conditions	21
3.4. Receiver efficiency	23
3.5. Numerical results	23
3.5.1. Heat release profile	24
3.5.2. Temperature profile	28
4. Comparison between surface-based and nanofluid-based receivers	35
4.1. Surface-based receiver modelling	35
4.2. Comparison of results	42
5. Experimental study on nanofluids	45
5.1. Equipment characteristics	45
5.1.1. Datalogger	45
5.1.2. Temperature sensors	46

5.1.3. Pyranometer.....	49
5.1.4. Volumetric receiver	50
5.1.5. Solar simulator	51
5.2. Nanofluid.....	56
5.2.1. Nanofluid properties	56
5.2.2. Nanofluid preparation.....	58
5.3. Results and experimental validation.....	59
6. Modelling of a volumetric flow receiver	63
6.1. Temperature profile	63
6.2. Numerical model.....	64
6.2.1. Internal points	66
6.2.2. Boundary points	67
6.3. Receiver efficiency	68
6.4. Numerical results	68
7. Conclusions and future work.....	75
8. References.....	77
9. Appendix.....	81

LIST OF FIGURES

Figure 1.1 – Temperature profile of a volumetric (a) and a surface-based receiver (b) [2].....	2
Figure 2.1 – Spectrum of ASD Pro-lamp.....	13
Figure 2.2 – Experimental setup for a transmissivity measurement.....	14
Figure 2.3 – Transmissivity of pure water [29] and Perfecto HT 5 thermal oil.....	14
Figure 3.1 – Schematic for model formulation of a volumetric solar receiver.....	15
Figure 3.2 – Comparison between AM0, AM1.5 Global and AM1.5 Direct spectra [30]	17
Figure 3.3 – One-dimensional mesh on a volumetric receiver	18
Figure 3.4 – One-dimensional mesh for internal plane on a volumetric receiver.....	20
Figure 3.5 – One-dimensional mesh for top plane on a volumetric receiver.....	21
Figure 3.6 – One-dimensional mesh for bottom plane on a volumetric receiver	22
Figure 3.7 – Heat release profile ($H = 0,01 \text{ m}$; $f_v = 0,01\%$)	24
Figure 3.8 – Effect of volume fraction on absorption efficiency	26
Figure 3.9 – Dimensionless heat release profile for different heights	27
Figure 3.10 – Effect of receiver height on absorption efficiency.....	28
Figure 3.11 – Temperature profile in transient regime for a graphite-based receiver	29
Figure 3.12 – Temperature profile in transient regime for a MWCNT-based receiver	29
Figure 3.13 – Coloured temperature profile in transient regime for a MWCNT-based receiver.....	30
Figure 3.14 – Variation of maximum temperatures with different concentration factors for a graphite-based receiver	31
Figure 3.15 – Variation of maximum temperatures with different concentration factors for a MWCNT-based receiver	31
Figure 3.16 – Variation of accumulated values of energy gain and loss	32
Figure 3.17 – Variation of efficiency on different nanofluids.....	33
Figure 4.1 – Schematic for model formulation of a surface-based solar receiver	35
Figure 4.2 – One-dimensional mesh for top plane on a surface-based receiver	36
Figure 4.3 – Temperature profile on transient regime for a selective surface-based receiver.....	37
Figure 4.4 – Three-dimensional temperature profile on transient regime for a selective surface- based receiver.....	38
Figure 4.5 – Variation of maximum temperatures with different concentration factors	39
Figure 4.6 – Variation of accumulated values of energy gain and energy loss	39
Figure 4.7 – Variation of efficiency on different fluids	40
Figure 4.8 – Variation of temperature on transient regime for a surface-based receiver.....	42
Figure 4.9 – Variation of temperature on transient regime for a nanofluid-based receiver	43
Figure 5.1 – Schematic of the experimental setup	45
Figure 5.2 – CR10 Datalogger [35]	46
Figure 5.3 – Thermocouple (type T).....	47
Figure 5.4 – Connection diagram of a 3 wire half bridge configuration of a PT100 [34]	47
Figure 5.5 – Eppley 8-48 pyranometer [37]	49
Figure 5.6 – Volumetric receiver schematic	50

Figure 5.7 – Volumetric receiver.....	50
Figure 5.8 – Spectrum of the extraterrestrial solar radiation compared to the spectrum of a 5777 K blackbody.....	51
Figure 5.9 – Comparison between AM0, AM1.5 Direct and solar simulator spectral distribution ...	53
Figure 5.10 – MWCNT structure [42].....	56
Figure 5.11 – Transmissivity of the different nanofluids	57
Figure 5.12 – Sonicating bath.....	58
Figure 5.13 – Fluid samples used in the experimental apparatus	59
Figure 5.14 – Experimental setup	59
Figure 5.15 – Spectrum of the lamp for solar simulator in the experimental setup.....	60
Figure 5.16 – Comparison of experimental and numerical results for graphite + water nanofluid..	61
Figure 5.17 – Comparison of experimental and numerical results for MWCNT + Perfecto HT 5 nanofluid.....	62
Figure 6.1 – Schematic for model formulation of a nanofluid-based solar receiver.....	63
Figure 6.2 – Bi-dimensional mesh for receiver domain discretization	65
Figure 6.3 – Velocity profile between parallel plates	65
Figure 6.4 – Flowchart of the numerical model formulation	66
Figure 6.5 – Boundary conditions schematic.....	67
Figure 6.6 – Temperature profile in transient regime at different points of the receiver length	69
Figure 6.7 – Mean outlet temperature under different solar concentration factors.....	69
Figure 6.8 – Mean outlet temperature for different nanofluids	70
Figure 6.9 – Efficiency of the volumetric flow receiver for different nanofluids	71
Figure 6.10 – Velocity impact on the receiver outlet temperature for different solar concentration factors.....	72
Figure 6.11 – Inlet temperature impact on the outlet temperature for different nanofluids	72
Figure 6.12 – Inlet temperature impact on the receiver efficiency for different nanofluids.....	73
Figure 6.13 – Inlet temperature impact on the receiver efficiency for different radiation levels ...	73
Figure 6.14 – Temperature profile in transient regime at different points of the receiver length ...	74
Figure 9.1 – Refractive index (n) and extinction coefficient (σ) of graphite [46]	83
Figure 9.2 – Extinction coefficient (σ) of Therminol VP1 [47]	83
Figure 9.3 – Transmissivity (τ) of Therminol VP1 using Eq. (2.11)	83
Figure 9.4 – Refractive index (n) and extinction coefficient (σ) of water [29]	84
Figure 9.5 – Transmissivity (τ) of water using Eq. (2.11).....	84
Figure 9.6 – Refractive index (n) of ethylene glycol [48]	84
Figure 9.7 – Extinction coefficient (σ) of ethylene glycol [47]	85
Figure 9.8 – Transmissivity (τ) of ethylene glycol using Eq. (2.11).....	85
Figure 9.9 – Print screen of the <i>RS3</i> software for spectrophotograms collection.....	86
Figure 9.10 – Function for volume fraction optimization through the Newton method.....	89
Figure 9.11 – Newton’s method implementation	90
Figure 9.12 – Programming window of CR10	92
Figure 9.13 – Solar simulator components	93

LIST OF TABLES

Table 2.1 – Thermodynamic properties of liquids	10
Table 2.2 – Thermodynamic properties of solids	10
Table 2.3 – Dynamic Viscosity of liquids	10
Table 3.1 – Comparison between absorption efficiency for different nanofluids ($H = 0,01$ m; $f_v = 0,01\%$).....	25
Table 3.2 – Numerical error for different nanofluids ($H = 0,01$ m; $f_v = 0,01\%$).....	25
Table 3.3 – Optimum volume fraction for 99,99% absorption efficiency ($H = 1$ cm; $\Delta y = 0,006$ cm).....	26
Table 3.4 – Numerical error for different nanofluids ($H = 1$ cm; $\Delta y = 0,006$ cm; $\eta_{abs} = 99,99\%$).....	27
Table 3.5 – Maximum temperature for different solar concentration factors ($H = 1$ cm; $\eta_{abs} = 99,99\%$; time = 1 hour).....	30
Table 3.6 – Numerical error for different nanofluids for $C = 1$	31
Table 3.7 – Receiver efficiency for different solar concentration factors ($H = 1$ cm; $\eta_{abs} = 99,99\%$; time = 1 hour)	33
Table 4.1 – Maximum temperatures for different concentration factors of a surface-based receiver	39
Table 4.2 – Comparison between fluids efficiency for different concentration factors for a surface-based receiver after 1 hour of operation.....	41
Table 5.1 – Classification criteria for spectral match.....	54
Table 5.2 – Spectral match classification for the solar simulator	54
Table 5.3 – Results for temporal instability of irradiance.....	55
Table 5.4 – Classification criteria for irradiance temporal instability.....	55

NOMENCLATURE

A	Area [m ²]
Bi	Biot number [-]
c_p	Specific heat capacity [J/(kg K)]
C	Solar concentration factor [-]
D	Diameter [m]
f_v	Volume fraction of nanoparticles [m ³ /m ³]
Fo	Fourier number [-]
G	Irradiance [W/m ²]
h	Heat transfer coefficient [W/(m ² K)]
H	Height [m]
$J_\lambda(y)$	Spectral intensity [W/(m ² nm)]
k	Thermal conductivity [W/(m K)]
L	Length [m]
m	Relative refractive index [-]
\dot{m}	Mass flow rate [Kg/s]
n	Refractive index [-]
Pe	Péclet number [-]
Pr	Prandtl number [-]
$P(y)$	Radiative flux [W/m ²]
q	Heat rate [W]
q'''	Volumetric heat rate [W/m ³]
R	Resistance [Ω]
Re	Reynolds number [-]

t	Time [s]
T	Temperature [°C]
U	Wind speed [m/s]
v	Velocity [m/s]
V	Volume [m ³]
V	Electric potential [V]

Greek letters:

α	Absorptivity [-]
α	Thermal diffusivity [m ² /s]
ε	Emissivity [-]
η	Efficiency [-]
θ	Angle [°]
κ	Absorption Coefficient [1/m]
λ	Wavelength [nm]
μ	Dynamic viscosity [kg/(m s)]
ρ	Density [Kg/m ³]
σ	Extinction coefficient [-]
σ	Stefan–Boltzmann constant [W/(m ² K ⁴)]
τ	Transmittance [-]

Subscripts:

<i>abs</i>	absorption
<i>amb</i>	ambient
<i>conv</i>	convection

f final
h hydraulic
i initial
max maximum
rad radiation
ref reference
scat scattering

Superscripts:

— average value
* dimensionless variable

ACRONYMS

AM Air Mass

ASTM American Society for Testing and Materials

HTF Heat Transfer Fluid

IR Infrared

MWCNT Multi-Walled Carbon Nanotubes

PRT Platinum Resistance Thermometer

RTD Resistance Temperature Detectors

TC Thermocouple

UV Ultraviolet

1. INTRODUCTION

The shortage of fossil fuels, environmental concerns and increasing demand of energy shown in the past years make urgent the use of alternative energy sources. Renewable energies have proven to be a good and viable alternative since they are sustainable, free and abundant. In particular, efforts on the development of solar energy technologies have been made over the last years. One of the principal methods of harvesting and converting solar energy into thermal energy for subsequent use is through solar thermal collectors, which may vary drastically in their collecting and converting mechanisms. Nowadays, solar thermal technologies are used in a large variety of applications, such as water heating, electricity generation, drying, desalinization, etc. However, most of these technologies use an absorbing surface to harvest and convert solar radiation into thermal energy. This means that their efficiency is limited, not only by the absorber capability on capturing solar energy, but also by the quantity of energy (heat) that is transferred to a working fluid through conduction and convection. On one hand, selective coatings can be applied on the absorber surface in order to enhance absorptivity across the spectrum of incident solar radiation and decrease its emissivity in the thermal radiation spectrum. However, a thermal resistance is always present between the absorbing surface and the working fluid, resulting in a temperature difference between them, which is even bigger at high levels of solar concentration. This temperature difference leads to significant losses and therefore to lower conversion efficiencies.

On the other hand, and as an alternative, volumetric receivers can be used, in which solar radiation is directly absorbed in the volume of a nanofluid without directly heating any other structures within the receiver. A nanofluid is a fluid containing nanoparticles (nanometer-sized particles, usually 1 to 100 nm in diameter size [1]) suspended in a base fluid. Generally, the base fluid is transparent to solar radiation and the nanoparticles are responsible for the absorption and scattering of the incoming solar radiation passing through the medium. Since thermal conductivity of nanoparticles is substantially higher compared to the base fluid, absorbed energy is more uniformly distributed in the surrounding fluid, which decreases the temperature difference between the absorber particles and the base fluid.

Figure 1.1 illustrates the potential advantage of a volumetric receiver compared to an ideal selective surface, for the same mean fluid temperature (\bar{T}_f), incoming concentrated solar irradiance (CG_S) and height (H). It is clear that the highest temperature occurs within the fluid in the direct

absorption solar collector (a), while for indirect absorption (b) the highest temperature occurs at the absorber surface, leading to higher emission losses [2].

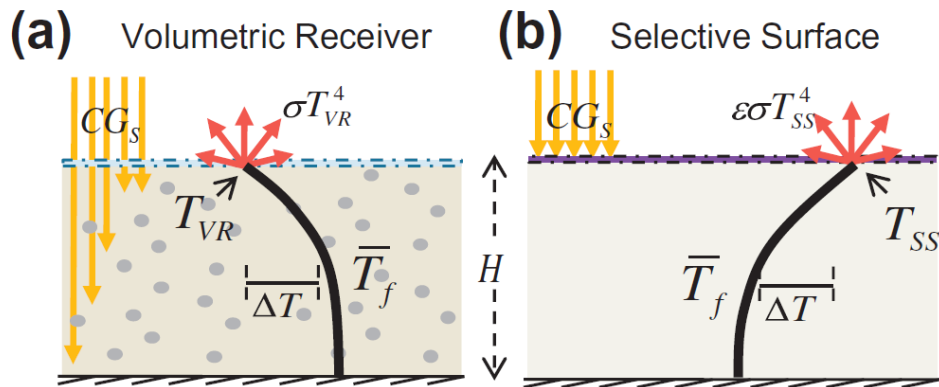


Figure 1.1 – Temperature profile of a volumetric (a) and a surface-based receiver (b) [2]

According to M. A. Sadique and A. Verma [1] the use of nanofluids can increase the collector's efficiency by 10% to 15%, yet, efficiency is still limited by the maximum allowable temperature of the heat transfer fluid (HTF). Depending on many factors, the performance of volumetric receivers may vary from these efficiency improvements. On this matter, O. Mahian et. al. [3] carried out a review on the different applications of nanofluids in solar energy, in which the assessment on the receiver performance obtained by each author is presented. One can highlight some of the state of the art developments:

A. Veeraragavan et. al. [4], developed an analytical model for the design of volumetric solar flow receivers and used graphite nanoparticles suspended in Therminol VP1 as a case of study. The volume fraction and receiver length were optimized where the total efficiency is maximized. Some similarities can be found in comparison to this dissertation, however, when calculating the heat release profile in the receiver, it was used the sun spectrum instead of the equivalent black body spectrum at 5800 K, and the optical properties of this nanofluid were modelled as a function of wavelengths, instead of using constant values. Also, a fully developed flow was considered in this dissertation as opposite to a plug flow.

To what concerns experimental apparatus, T. Otanicar et. al. [5] investigated the performance of graphite spheres, carbon nanotubes and silver spheres suspended in water as base fluid, on a micro-solar thermal collector. The authors demonstrated efficiency improvements up to 5% due to the influence of the nanofluid absorption mechanisms. A similar configuration to the one used on this dissertation was carried out by V. Khullar et. al. [6], in which amorphous carbon nanoparticles were

dispersed in ethylene glycol and multi-walled carbon nanotubes (MWCNTs) dispersed in distilled water. The authors also compared the obtained results with a solar selective surface-based receiver and concluded that higher stagnation temperatures were obtained with volumetric receivers. A. Lenert [7] also performed similar experiments to investigate the efficiency of nanofluid-based receivers for high temperature applications, such as power generation, using carbon-coated nanoparticles suspended in Therminol VP1. The results with nanofluids, considering the respective receiver design, suggested a major benefit for concentration levels superior to 100 and a receiver height superior to 10 cm.

In another way, studies regarding low temperature solar collectors have also been investigated, in which H. Tyagi and P. Phelan [8] compared the performance of two types of non-concentrating solar collectors: a typical flat-plate collector and a thin flowing film of nanofluid (mixture of water and aluminum nanoparticles). Under similar operating conditions the nanofluid-based receiver showed an increase of efficiency up to 10%. As an example of another low temperature configuration, R. Nasrin and M. A. Alim [9] investigated the heat transfer performance in a wavy solar collector, using silver and copper oxide nanoparticles suspended in water, in which the silver-based nanofluid performed the best.

A rather different approach to the one presented on this dissertation was developed by V. Khullar and H. Tyagi [10], in which an attempt to harvest solar energy through the usage of nanofluid-based concentrating parabolic solar collectors was carried out. A numerical model was implemented using the finite difference technique and results were compared with the experimental performance of conventional concentrating parabolic solar collectors under similar conditions. The authors concluded that a nanofluid-based collector with aluminum nanoparticles dispersed in Therminol VP1 improved efficiency in about 5 to 10%. No experimental study on this matter was found.

Very recently, D. C. Hernandez Aita [11] developed a two-dimensional model to predict the temperature profile and performance of volumetric receivers using supercritical carbon dioxide as base fluid and carbon nanoparticles suspended in that medium. A comparison of this base fluid with Therminol VP1 was carried out for low inlet temperatures, in which the system performance improved 20%, and the outlet temperature increased approximately 250°C when using supercritical carbon dioxide. The optical thickness, receiver height and solar concentration factor parameters were optimized, which allowed to conclude that volumetric receivers have the potential to collect solar energy more efficiently when compared to surface-based receivers. However, surface-based

receivers with Therminol VP1 showed better system efficiencies for concentration factors lower than 7 and nanofluid height lower than 2,5 cm. The author also evaluated the performance of this technology when integrated into a Brayton cycle for concentrating solar plants. At a high inlet temperature of 675 K and considering an ideal Brayton cycle, the system proved to have potential to achieve efficiencies up to 68% for concentration factors higher than 30 and nanofluid height superior to 15 cm.

The developments carried out until now, have shown that volumetric receivers can be a more efficient way of collecting and converting solar energy. But how can these improvements be quantified as to the impact on the environment? Very few studies have been made on this matter. Concerning the non-concentrating technologies, T. Otanicar and J. Golden [12] demonstrated that in comparison to a conventional solar collector, the nanofluid-based receiver presents less emissions of carbon dioxide on both manufacturing and operating levels. As for the concentrating systems, V. Khullar and H. Tyagi [13] also showed considerable emission reductions and fuel savings if nanofluid-based concentration solar water heating systems are adopted.

In this dissertation, two different types of concentrating solar volumetric receivers were investigated. A first model under non-flowing conditions, in which the purpose was to study the temperature profile and performance of eight different nanofluids that result from a combination of two solid particles (graphite and MWCNTs) and four base fluids (water, Therminol VP1, Perfecto HT 5 and ethylene glycol). As part of this study, an experimental apparatus was prepared and results were compared with the numerical model. Similar temperature profiles were obtained which validated the numerical model. Under comparable operating conditions, the numerical model was also compared to a selective surface-based receiver to emphasize the different absorbing mechanisms of solar radiation. A second model was numerically developed in which the same nanofluids were tested under flowing conditions in a parallel plate geometry. An analysis on the impact of solar concentration factor, velocity and inlet temperature on such receiver was carried out.

1.1. Aim

The aim of this dissertation is to contribute to the development and optimization of volumetric receivers with nanoparticle suspensions. One of the main purposes of this work is to investigate the mechanisms that are responsible for sun light absorption due to nanofluids, and develop a numerical and experimental analysis under transient and stationary regimes of a solar receiver with stagnated fluid. A second objective is to improve the performance of volumetric flow receivers through the development of a numerical model for both transient and stationary conditions.

1.2. Outline of the dissertation

This dissertation is structured in seven distinct chapters organized as follows:

In Chapter 1, a general introduction to the subject-matter is presented.

Chapter 2 introduces the nanofluids concept and features that allow enhancing the performance of volumetric receivers. A review on their preparation and stability issues is presented, and the radiative, thermal and transport properties are analyzed in detail.

Chapter 3 addresses the modelling of a non-flowing volumetric receiver in which only heat diffusion is considered. The volume fraction of nanoparticles is optimized to further determine the temperatures and efficiencies for eight different nanofluids under various conditions. Results are discussed and compared.

Chapter 4 concerns the comparison of the numerical results from Chapter 3 with those obtained for a surface-based receiver using a similar numerical model and considering four different fluids.

Chapter 5 addresses an experimental study in which a volumetric receiver was designed and built. Four nanofluids were studied with the purpose of validating the numerical results of Chapter 3.

Chapter 6 features the modelling of a volumetric flow receiver in which both diffusion and convection heat transfer are considered. An assessment of the receiver performance under different conditions is carried out for the same nanofluids studied in the previous chapters.

Finally, in Chapter 7, the main conclusions are presented and future work suggestions and improvements are proposed.

2. NANOFUID PREPARATION AND PROPERTIES

A nanofluid is composed by nanometer sized particles (usually 1 to 100 nm in diameter size [1]) suspended or dispersed in a fluid. Nanofluids have some uncommon features that give them a great potential on solar energy applications. Therefore, efforts for better understanding on how such fluids work should be made. The study of their preparation, stability and properties are of course a matter of concern, and will be analyzed in this chapter.

The enhancement on solar energy absorption by a nanofluid can be maximized with the change of particle size, shape, material and volume fraction. In respect to the material, different types of solid particles may be used in nanofluids [14]:

- Metals: Ag (silver), Al (aluminum), Au (gold), Cu (copper), Fe (iron).
- Oxides: Al₂O₃ (aluminum oxide), CuO or Cu₂O (copper oxides), Fe₂O₃ (iron oxide), SiO₂ (silicon dioxide), TiO₂ (titanium dioxide).
- Carbon: graphite, single-walled nanotubes, double-walled nanotubes, or multi-walled carbon nanotubes.
- Other particles: Si (silicon) compounds

Concerning the most commonly used base fluids, they can be categorized as follows:

- Liquids: water, organic and mineral fluids (such as thermal oils), glycols, molten salts.
- Gases: air (gas-particle suspensions)

2.1. Preparation and stability

There are two major challenges in preparing a nanofluid, which is to get a uniform particle distribution and a uniform particle size diameter within the base fluid volume. The problem lies in the aggregation process that occurs due to the interaction between the particles, which may lead to the generation of large aggregates. This process causes the settling of the larger particles, originating a very uneven distribution that can alter the properties of the nanofluid. However, chemical compounds such as surfactants, dispersants, and coatings can be added to the base fluid to prevent particle aggregation [14]. On one hand, these compounds do ensure that the particles

are uniformly distributed in the suspension, but on the other hand, the thermo-physical properties of the nanofluid may alter [15].

Although the methods and procedures to prepare a nanofluid vary significantly, in general, they can be classified as a one-step process or a two-step process. In the one-step process, the synthesis of the nanofluid is made when the nanoparticles and the base fluid are simultaneously formed. It is adequate to use this process for nanoparticles that may change their composition or aggregate if not in contact with the base fluid. The oxidation of some metals when exposed to air serves as an example [14]. In the two-step process, the synthesis of the nanofluid is obtained by mixing the already prepared nanoparticles with the base fluid. The preparation of the nanoparticles (step one) can be obtained from different mechanical, physical or chemical processes, such as, milling, grinding, sol-gel and vapor phase methods [15]. The mixing of the nanofluidic suspension (step two) may be performed by a mechanical method such as vibration and (ultra)sonification [14].

The main advantage of the one-step process lies on the purity and size uniformity achieved when the nanoparticles are formed. However, compared to the industrial mass production scale, only small quantities of nanofluid can be produced. By opposition, in the two-step process, the nanoparticles can be separately produced on a mass and cost-effective way. The main concern of the process is to obtain a homogenous and uniform suspension of solid particles [14].

As mentioned before, the use of surfactants for the stabilization of the nanoparticles in the base fluid can be benefic. Yet, most available surfactants degrade significantly at temperatures above 60°C [16] and may also alter the thermo-physical properties of the nanofluid. A review carried out by S. Mukherjee and S. Paria [15] refer other stability enhancements procedures besides adding surfactants and ultrasonic agitation, such as, the surface modification techniques and the pH control of nanofluids. The study also presents the different stability evaluation methods for nanofluids, which include the zeta potential analysis, the sedimentation method, the centrifugation method, the spectral analysis method and the 3 omega method.

2.2. Thermodynamic and transport properties

Nanofluids have unique properties that may enhance their performance when compared to other heat transfer fluids. The correct determination of these properties according to the type, shape, and volume fraction of nanoparticles is essential. Throughout this work, the estimate values of these properties were determined as follows:

- Density (ρ):

The density of a nanofluid must consider the solid and liquid volume fraction balance [14]:

$$\rho = f_v \rho_{nanoparticles} + (1 - f_v) \rho_{basefluid} \quad (2.1)$$

- Specific heat capacity (c_p):

The specific heat capacity of nanofluids should also consider the volumetric proportion of nanoparticles and base fluid, and it can be determined in the following way [14]:

$$c_p = \frac{f_v c_p \rho_{nanoparticles} + (1 - f_v) c_p \rho_{basefluid}}{\rho} \quad (2.2)$$

- Thermal conductivity (k):

The thermal conductivity of a nanofluid may be calculated as an approximation [14] using Eq. (2.3) which is valid not only for spherical but also for irregular particles, such as carbon nanotubes. This equation also takes into account the difference in the order of magnitude between the solid and the liquid thermal conductivities, given by the ratio $k_{nanoparticles}/k_{basefluid}$.

$$k = k_{basefluid} \left(1 + \frac{f_v k_{nanoparticles}}{3 k_{basefluid}} \right) \quad (2.3)$$

- Dynamic viscosity (μ):

The dynamic viscosity is a transport property that can be determined for nanofluids using the following equation [14]:

$$\mu = \mu_{basefluid} (1 + 2,5 f_v + 6,5 f_v^2) \quad (2.4)$$

- Thermal diffusivity (α):

The thermal diffusivity can be calculated using the previous estimated properties as follows:

$$\alpha = \frac{k}{\rho c_p} \quad (2.5)$$

Throughout this dissertation, constant values of thermodynamic properties were used, which are summarized below.

Table 2.1 – Thermodynamic properties of liquids

	Boiling Temperature [°C] at 1 atm	Maximum Temperature [°C]	Density * [kg/m ³]	Specific heat capacity * [J/(kg K)]	Thermal conductivity [W/m K] *	Reference
Pure water	100	374,14	996,999	4180,3	0,6096	[17]
Therminol VP1	257	400	1061,0	1561,6	0,1356	[18]
Perfecto HT 5	-	420 (320**)	868,412	1860	0,1330	[19]
Ethelyne glycol	197	-	1114,5	2405,6	0,2512	[17]

* at 25 °C

** maximum recommended by supplier

Table 2.2 – Thermodynamic properties of solids

	Density *		Specific heat capacity *		Thermal conductivity **	
	[Kg/m ³]	Reference	[J/(kg K)]	Reference	[W/m K]	Reference
Graphite	2210	[17]	709	[17]	30	[20]
MWCNT	2600	[21]	750	[22]	3350	[14]

* at 25 °C

** typical values

Table 2.3 – Dynamic Viscosity of liquids

	Dynamic Viscosity [kg/(m s)] *	Reference
Pure water	0,000891	[17]
Therminol VP1	0,0037	[18]
Perfecto HT 5	0,0554	[19]
Ethelyne glycol	0,0166	[23]

* at 25 °C

2.3. Radiative properties

The study of the radiative properties of nanofluids is extremely important to what concerns solar energy applications. When an electromagnetic wave, such as the solar radiation, interacts with a medium, two distinct situations can occur, simultaneously or not: absorption and scattering. These phenomena may change the intensity and direction of the radiation, depending on the radiative properties of the medium. The intensity change is caused by the absorption and the scattering is caused either by reflection, refraction or diffraction of the radiation due to the solid particles. To quantify these phenomena when a nanofluidic medium is at stake, an absorption coefficient can be considered, which is calculated as an approximation by simply adding the absorption coefficients of the base fluid and its suspended nanoparticles [24]:

$$\kappa_{\lambda, nanofluid} = \kappa_{\lambda, basefluid} + \kappa_{\lambda, nanoparticles} \quad (2.6)$$

The absorption coefficient of the base fluid depends only on the complex component of the refractive index (σ_{λ}) and incident wavelength of incident radiation (λ) [25]:

$$\kappa_{\lambda, basefluid} = \frac{4 \pi \sigma_{\lambda, basefluid}}{\lambda} \quad (2.7)$$

However, when concerning the nanoparticle effect of absorption and scattering, the absorption coefficient reads as [25]:

$$\kappa_{\lambda, nanoparticles} = \frac{3 f_v Q_{\lambda, nanoparticles}}{2 D_{nanoparticle}} = \frac{3 f_v (Q_{\lambda, scat} + Q_{\lambda, abs})}{2 D_{nanoparticle}} \approx \frac{3 f_v Q_{\lambda, abs}}{2 D_{nanoparticle}} \quad (2.8)$$

in the limit of low volume fraction ($f_v < 0,006$) and assuming a uniform particle size distribution through the nanofluid, although in reality, particles tend to agglomerate over time. In this case, $Q_{\lambda, scat}$ and $Q_{\lambda, abs}$ are, respectively, the scattering and absorption efficiencies, and $D_{nanoparticle}$ is the mean diameter of the nanoparticles. According to the theory of Rayleigh scattering, neglecting $Q_{\lambda, scat}$ is a valid approximation since the particle size diameter in the nanofluids (usually 10 to 50 nm) is very small compared to most of the solar radiation wavelength (400 to 600 nm). The absorption efficiency factor $Q_{\lambda, abs}$ can be determined as an approximation by [25]:

$$Q_{\lambda, abs} = \frac{4 \pi D_{nanoparticle}}{\lambda} IM \left\{ \frac{m^2 - 1}{m^2 + 2} \right\} \quad (2.9)$$

where m is the ratio of complex refractive index of the particles to the refractive index of the base fluid:

$$m = \frac{n_{\lambda, nanoparticles} + i\sigma_{\lambda, nanoparticles}}{n_{\lambda, basefluid}} \quad (2.10)$$

The radiative and optical properties of the nanofluids studied in this work are presented in appendix I, except for Perfecto HT 5, in which optical properties were considered the same as Therminol VP 1, and the radiative properties as function of wavelength were experimentally determined as follows.

2.3.1. Experimental characterization of radiative properties

A spectroradiometer allows the absolute or relative measurement of light energy. This means that not only spectral irradiance levels can be investigated, but also spectral transmissivity of materials can be obtained. These features will prove to have an extremely important role in the study of the radiative properties of fluids, in which, a FieldSpec® HandHeld spectroradiometer model from *ASD Inc.* [26] was used for all spectral measurements collected throughout this work. This particular model has a wavelength range that goes from 325 to 1075 nm, with a spectral resolution of 1 nm. This equipment should be operated when connected to a computer with an appropriate ASD software (*RS3*) that controls the spectroradiometer readings. A complete spectrum recording was set to be 1,09 seconds (integration time) and the white reference is set as the mean of 10 measurements of a reference medium or reference surface. The spectroradiometer automatically also takes a dark current measurement to later discount on the registered values the offset current of the internal circuits. Appendix II presents the software operating window. Collected data can then be post-processed by *ViewSpec* (ASD software).

• Measuring transmissivity

To determine the transmissivity of a particular material, any illumination source is appropriate as long as it doesn't have null values of irradiance in the wavelength range that transmissivity is to be studied. A steady light flux should also be used, since the results will be affected if flux changes over time. Due to its stable behaviour with no major oscillations, an ASD Pro-Lamp model [27] was used for all indoor measurements concerning transmissivity of base fluids and nanofluids. Its emitting spectrum over the 350-2500 nm range was measured with the spectroradiometer placed at a distance of 40 cm and the collected data (percentage of total area) can be observed in Figure 2.1.

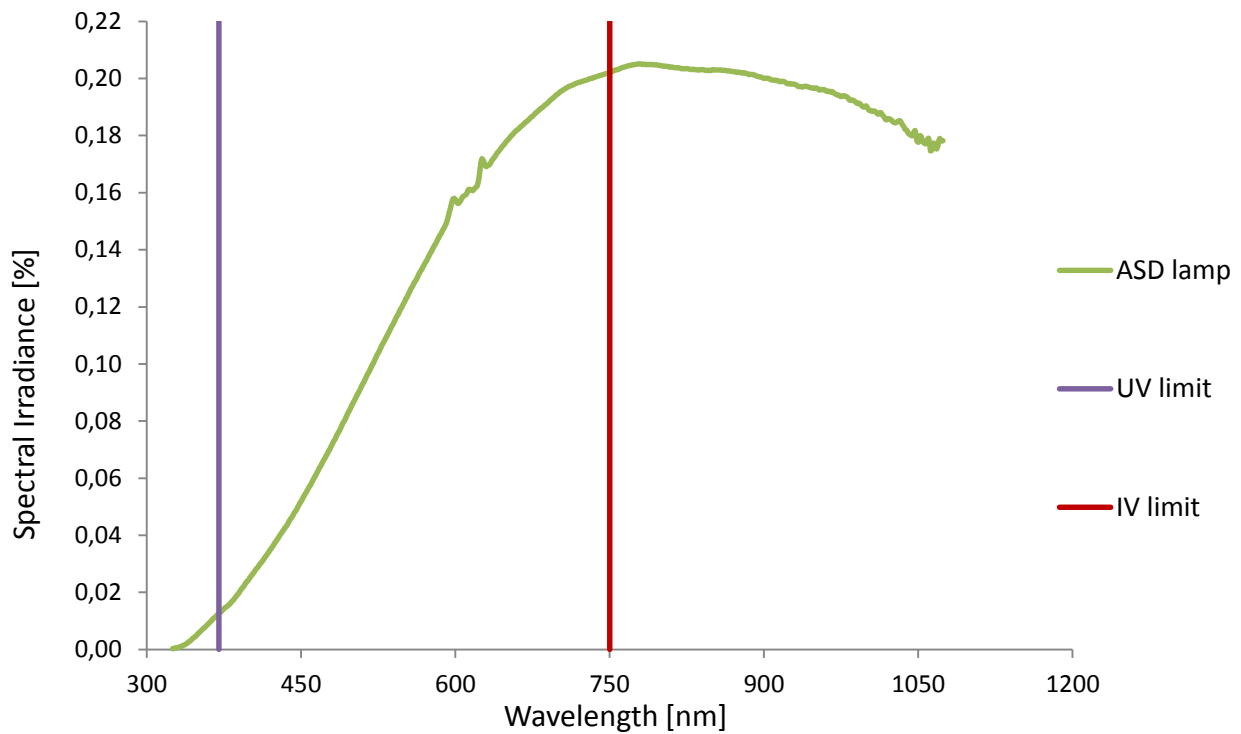


Figure 2.1 – Spectrum of ASD Pro-lamp

An optic accessory was attached to the spectroradiometer to narrow its field of view to 1 degree, so that the effect of diffuse light is minimized during the measurements. To ensure that a steady full light output was obtained, the lamp was turned on and ran continuously for 30 minutes to warm-up before any readings were taken. Measurements were also performed under controlled conditions, where only the direct light from the lamp reaches the spectroradiometer field of view.

Measuring transmissivity consists in the comparison of a sample with a white reference. Once the white reference option is set in the RS3 software, the spectrum received by the spectroradiometer will have its transmissivity set equal to one. These readings should include, not only the lamp's spectrum, but also the influence of the cuvette or any other instruments that modify the light spectrum and intensity. In this case, the cuvettes used in this work had an optimal transmissivity over the 340 - 800 nm range, with an optical path of 1 cm [28]. With this procedure, when the sample in the cuvette is placed in the cuvette support, only the sample's transmissivity is measured. An illustration of the setup is shown in Figure 2.2, which was equally used on every other transmissivity measurements.

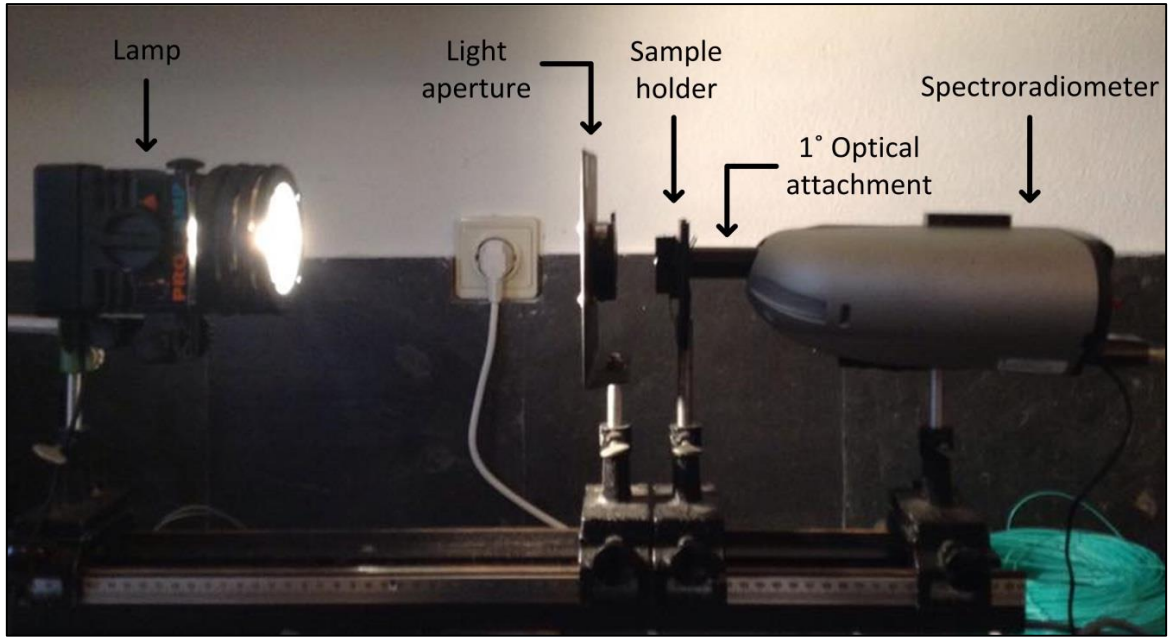


Figure 2.2 – Experimental setup for a transmissivity measurement

The measured spectral transmittance of Perfecto HT 5 is shown in Figure 2.3 together with the transmissivity of pure water for comparison.

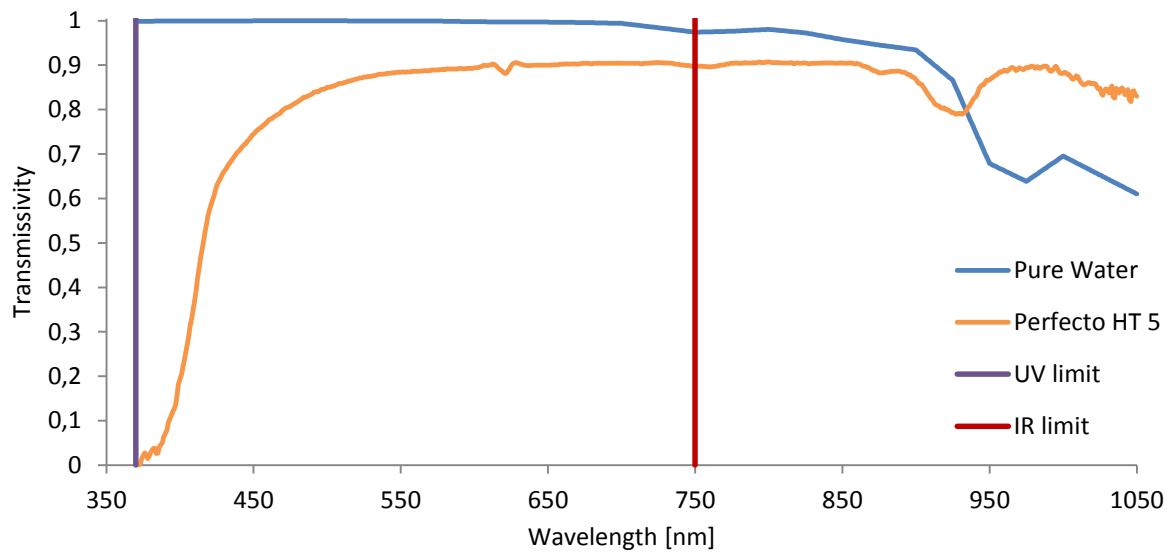


Figure 2.3 – Transmissivity of pure water [29] and Perfecto HT 5 thermal oil

The transmissivity of the samples is a function of its optical properties through the following expression:

$$\tau = e^{\left(-\frac{\kappa L}{\cos(\theta)}\right)} \quad (2.11)$$

where κ is the absorption coefficient, L is the normal path length of light through the sample and θ is the angle formed between the incident rays and the normal to the sample's surface.

3. NANOFUID-BASED RECEIVER MODELLING AND OPTIMIZATION

The main purpose of this chapter is to model the temperature profile, absorbed heat and efficiency, in transient and stationary regimes, of a volumetric solar receiver as schematized in Figure 3.1.

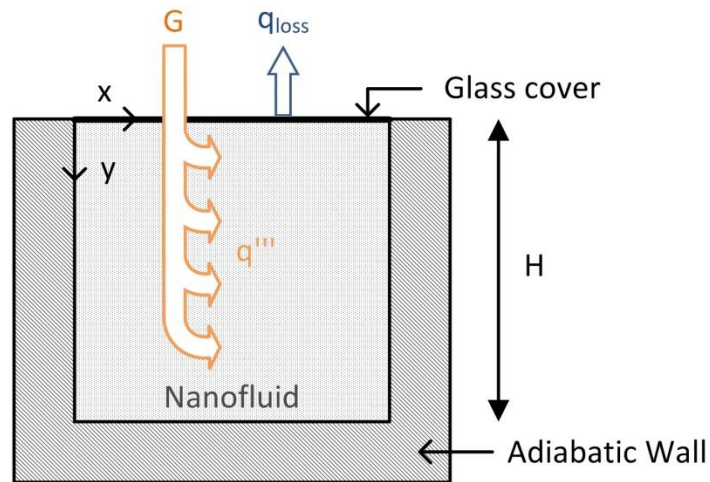


Figure 3.1 – Schematic for model formulation of a volumetric solar receiver

In this schematic, G represents the incident radiation flux, q''' is the absorbed volumetric heat rate, q_{loss} is the heat loss in the upper surface and H is the height of the receiver.

Some assumptions were made in order to simplify the modelling of the receiver:

- Uniform initial temperature of nanofluid;
- Constant ambient temperature;
- Nanofluid velocity equals zero over x and y directions, therefore, convection is neglected;
- Nanoparticles are uniformly distributed in the base fluid volume;
- Side and bottom walls are adiabatic;
- Collimated incident solar radiation in the top surface ($y = 0$);
- Constant incident solar radiation over time on the top surface ($y = 0$);
- Heat losses only through the top surface ($y = 0$);
- Glass thickness is neglected;
- Glass transmissivity equals one;
- Reflection and absorption of sunlight at the bottom of the receiver is neglected.

The first step to obtain the temperature profile is to determine the heat release profile due to the solar radiation absorption which corresponds to the volumetric heat rate in the nanofluid.

3.1. Volumetric heat rate profile

The volumetric heat release q''' as function of y can be determined by an energy balance assuming that the change in the y direction of the incident spectral flux $J_\lambda(y)$ due to attenuation by the nanofluid is dissipated as a local heat release:

$$q'''(y) = -\frac{dP(y)}{dy} \quad (3.1)$$

in which the radiative flux (P) at a given depth (y) is obtained by integrating $J_\lambda(y)$ over the wavelength range of incident radiation:

$$P(y) = \int_{\lambda=0}^{\lambda=+\infty} J_\lambda(y) dy \quad (3.2)$$

The spectral intensity, $J_\lambda(y)$, as function of y is obtained through the Beer-Lambert law [25]:

$$\frac{dJ(y)}{dy} = -\kappa_{\lambda, nanofluid} J(y) \quad (3.3)$$

resulting in:

$$J_\lambda(y) = J_\lambda(0) e^{-y \kappa_{\lambda, nanofluid}} \quad (3.4)$$

where $\kappa_{\lambda, nanofluid}$ represents the absorption coefficient of the nanofluid, obtained from the base fluid and solid particle properties as described in Chapter 2. The spectral intensity at the top surface, $J_\lambda(0)$, corresponds to the incident solar spectral distribution, that can be one of the three cases if defined by the ASTM [30]: AM0, AM1.5 global and AM1.5 direct. As shown in Figure 3.2, the total area values are a result of the integration of the respective spectral intensity, considering one sun ($C=1$).

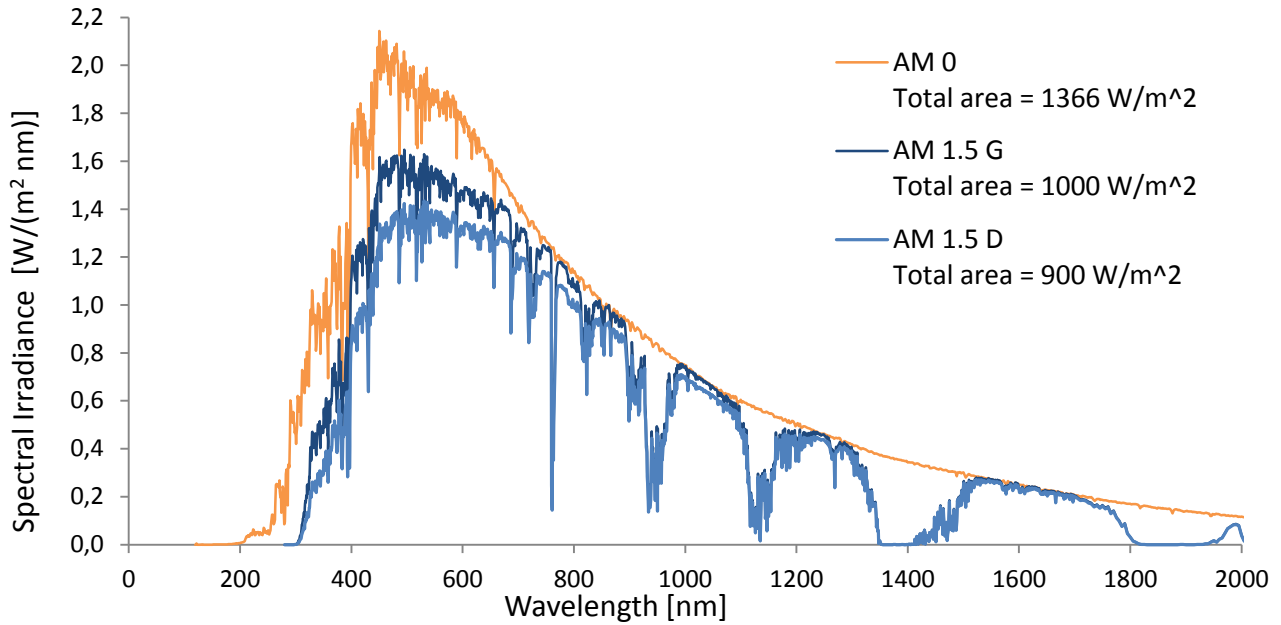


Figure 3.2 – Comparison between AM0, AM1.5 Global and AM1.5 Direct spectra [30]

3.1.1. Absorption efficiency

For a given volume fraction (f_v) and receiver height (H), the absorption efficiency is defined as:

$$\eta_{abs} = 1 - \frac{P(y = H)}{P(y = 0)} \quad (3.5)$$

where $P(y)$ is the radiative flux as function of height, see Eq. (3.2). Analyzing this equation, one can see that if all incident solar radiation is absorbed through the nanofluid before reaching the bottom surface ($y = H$), the radiative flux $P(y = H)$ equals zero, thus the absorption efficiency becomes 100%. This means that the nanofluid has an excess of nanoparticles, or that the height of the receiver is over dimensioned. Special attention should be paid on this matter and, if possible, an optimization should be done to find the correct trade-off between volume fraction and receiver height. Note that absorption efficiency is independent of incident solar flux.

3.2. Temperature profile

The temperature profile of a nanofluid that directly absorbs solar radiation can be obtained by solving the energy equation in an elementary volume that results by balancing the heat absorbed over time, heat conduction effect, and volumetric heat generation (already demonstrated on section 3.1):

$$\rho c_p \frac{\partial T}{\partial t} + k \nabla^2 T + q'''(y) = 0 \quad (3.6)$$

where,

$$\nabla^2 T = \frac{\partial}{\partial x} \left(\frac{\partial T}{\partial x} \right) + \frac{\partial}{\partial y} \left(\frac{\partial T}{\partial y} \right) + \frac{\partial}{\partial z} \left(\frac{\partial T}{\partial z} \right) = \frac{\partial^2 T}{\partial x^2} + \frac{\partial^2 T}{\partial y^2} + \frac{\partial^2 T}{\partial z^2} \quad (3.7)$$

Since no thermal flux on x and z directions are considered in the present model, heat transfer modelling becomes one-dimensional (y direction), and so, energy balance equation reads as:

$$\rho c_p \frac{\partial T}{\partial t} + k \frac{\partial^2 T}{\partial y^2} + q'''(y) = 0 \quad (3.8)$$

where ρ , c_p and k are the thermodynamic properties of the nanofluid under study.

Note that Eq. (3.8) is only valid when thermal conductivity is constant (not temperature dependent).

This equation was numerically solved in transient regime as described in section 3.3.

3.3. Numerical model

The explicit method [32] was used to numerically solve the energy equation, Eq. (3.8), which is a second order differential equation. This method consists on the approach of the continuous conduction heat transfer area on a set of discrete points, given by the intersection of horizontal and vertical lines. However, once there is no heat transfer on x direction, to simplify the model, a one-dimensional mesh on y direction can be created, as shown in Figure 3.3, in which j represents the position of the horizontal planes on y direction, and these planes were assumed equidistant and parallel to the receiver's borders.

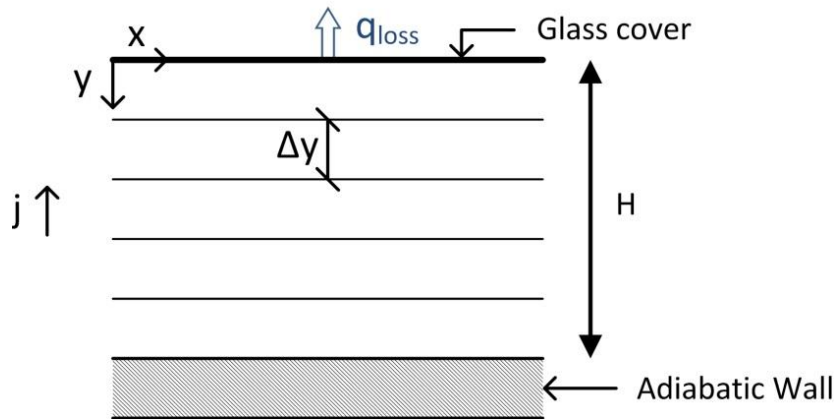


Figure 3.3 – One-dimensional mesh on a volumetric receiver

As a result of the space discretization, the temperature distribution is now represented by a finite number of temperatures. However, to determine the temperature in transient regime, temporal domain also needs to be discretized. The simplest way is to divide time on a set of constant intervals (Δt). The explicit method approximates the temporal derivative of temperature from Eq. (3.8) on a finite difference, by comparing the temperature at the moment k and the temperature on the consecutive instant, represented by $k + 1$:

$$\frac{\partial T}{\partial t} = \frac{T_j^{k+1} - T_j^k}{\Delta t} \quad (3.9)$$

One of the problems related to explicit method is that oscillations can occur in the numerical solution when using a large step time (Δt). For a one-dimensional mesh, a stable result can be obtained if step time is set to be smaller than [32]:

$$\Delta t \leq \frac{\Delta y^2}{\alpha (2 + 2 Bi)} \quad (3.10)$$

where α is thermal diffusivity and Bi is Biot number.

Finally, the temperature profile of the receiver in transient regime can be determined by solving the energy balances on each horizontal plane ($\Delta x \times \Delta w$) and on each time step. Note that each temperature does not represent the temperature over a particular horizontal plane but the temperature associated to a small region around the plane (shaded areas). Considering the stipulation where index j increases in the bottom-to-top direction, and that the flux on energy balance is positive when pointing to the shaded area, three different situations can occur according to the geometry of Figure 3.3: surface with convection (top), adiabatic surface (bottom), and internal plane.

3.3.1. Internal plane

To determine the fluid temperature in an internal plane j as schematized in Figure 3.4, an energy balance should be done maintaining energy conservation:

$$m c_p \frac{dT}{dt} = q_N + q_S + q''' \Delta x \Delta y \Delta w \quad (3.11)$$

where,

$$q_N = \frac{k \Delta x \Delta w (T_{j+1} - T_j)}{\Delta y} \quad (3.12)$$

$$q_S = \frac{k \Delta x \Delta w (T_{j-1} - T_j)}{\Delta y} \quad (3.13)$$

and $m = \rho \Delta x \Delta y \Delta w$ is the mass of nanofluid in the volume.

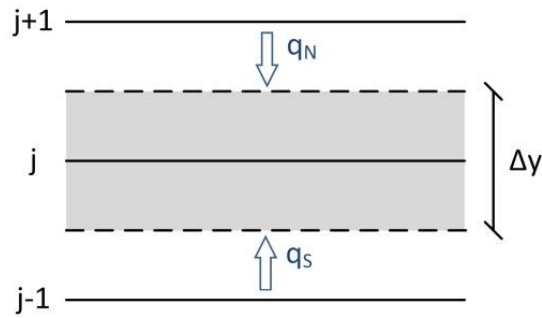


Figure 3.4 – One-dimensional mesh for internal plane on a volumetric receiver

By substituting Eq. (3.12) and Eq. (3.13) into Eq. (3.11), the temperature in the node j for the instant $t + \Delta t$ (corresponding to the supraindix $k+1$) is given by:

$$T_j^{k+1} = \frac{q_j''' \Delta t}{\rho_j^k c_{p_j}^k} + Fo(T_{j+1}^k + T_{j-1}^k) + T_j^k(1 - 2Fo) \quad (3.14)$$

where Fo is the Fourier number that is calculated by:

$$Fo = \frac{\alpha \Delta t}{\Delta y^2} \quad (3.15)$$

and α is the thermal diffusivity.

3.3.2. Boundary conditions

In the case of a one-dimensional mesh, the boundary conditions to restrict the model are just necessary on the top and bottom surfaces.

- Surface with convection ($y=0$)

Applying the heat energy balance to the top surface zone, see Figure 3.5, results the following equation:

$$m c_p \frac{dT}{dt} = q_{loss} + q_s + q''' \frac{\Delta x \Delta y \Delta w}{2} \quad (3.16)$$

where,

$$q_{loss} = (h_{conv} + h_{rad}) \Delta x \Delta w (T_{amb} - T_j) \quad (3.17)$$

$$q_s = \frac{k \Delta x \Delta w (T_{j-1} - T_j)}{\Delta y} \quad (3.18)$$

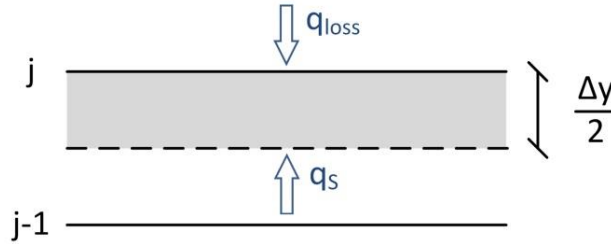


Figure 3.5 – One-dimensional mesh for top plane on a volumetric receiver

Solving energy balance equation in order to the temperature at the instant $k + 1$, we obtain:

$$T_j^{k+1} = \frac{q_j'''^k \Delta t}{\rho_j^k c_{p_j}^k} + 2 Fo (T_{j-1}^k + Bi T_{amb}) + T_j^k (1 - 2 Fo - 2 Fo Bi) \quad (3.19)$$

where Fo is the Fourier number, and Bi the Biot number that is calculated by:

$$Bi = \frac{(h_{conv} + h_{rad}) \Delta y}{k} \quad (3.20)$$

The convection heat transfer coefficient depends on the air speed and receiver length (L) on x direction, while the radiation heat transfer coefficient is temperature dependent [33]:

$$h_{conv} = \frac{8,6 U^{0,6}}{L^{0,4}} \quad (3.21)$$

$$h_{rad} = \varepsilon \sigma (T_{plate} + T_{amb}) (T_{plate}^2 + T_{amb}^2) \quad (3.22)$$

- Adiabatic surface ($y=H$)

The energy balance for a general configuration of a bottom surface as schematized according to Figure 3.6 is given by:

$$m c_p \frac{dT}{dt} = q_N + q_S + q''' \frac{\Delta x \Delta y \Delta w}{2} \quad (3.23)$$

where,

$$q_N = \frac{k \Delta x \Delta w (T_{j+1} - T_j)}{\Delta y} \quad (3.24)$$

$$q_S = (h_{conv} + h_{rad}) \Delta x \Delta w (T_{amb} - T_j) \quad (3.25)$$

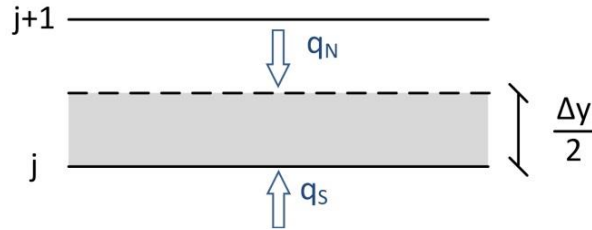


Figure 3.6 – One-dimensional mesh for bottom plane on a volumetric receiver

Solving Eq. (3.23) in order to the temperature at the instant $k + 1$ we get:

$$T_j^{k+1} = \frac{q_j'''^k \Delta t}{\rho_j^k c_{p_j}^k} + 2 Fo (T_{j+1}^k + Bi T_{amb}) + T_j^k (1 - 2 Fo - 2 Fo Bi) \quad (3.26)$$

However, since the bottom surface of the receiver is adiabatic, Biot number equals zero, and equation (3.26) results in:

$$T_j^{k+1} = \frac{q_j'''^k \Delta t}{\rho_j^k c_{p_j}^k} + 2 Fo T_{j+1}^k + T_j^k (1 - 2 Fo) \quad (3.27)$$

3.4. Receiver efficiency

For the particular case where a fluid is stationary, undergoing transient heating, and considering heat transfer on one dimension (y), the receiver's efficiency can be calculated by the ratio of the total absorbed thermal energy to the total incident energy over a period of time:

$$\eta = \frac{\sum_j^{n_j} \rho(j) c_p(j) (T_f(j) - T_i(j)) \Delta y}{C G t} \quad (3.28)$$

where $\rho(j)$ and $c_p(j)$ are the local density and specific heat capacity of the fluid. $T_f(j)$ represents the local temperature at the last instant, and T_i the initial temperature as function of y position. Finally, t is the total time that the receiver is exposed to solar radiation ($C G$).

3.5. Numerical results

The numerical model to determine the temperature profile on a volumetric receiver described in the previous section was implemented in *Matlab*. The developed program allows the comparison between eight distinct nanofluids that result from the different combinations between two carbon-based nanoparticles (graphite and multi-walled carbon nanotubes) and four base fluids (pure water, Therminol VP1, Perfecto HT 5 and ethylene glycol). With such program it is also possible to insert the desired nanoparticle volume fraction (f_v) and receiver height (H), as well as optimize one of these two variables, according to the optical properties discussed in Chapter 2.

The following outputs were obtained from simulations considering a constant input of solar radiation at the top of the receiver ($y = 0$). Since collimated rays were assumed, it is more adequate to use the solar spectral distribution defined in AM1.5 Direct, where the numerical integration of Eq. (3.2) and derivative of Eq. (3.1) are calculated using the discrete values between a wavelength range from 280 nm to 2500 nm. As to the parameters that affect heat loss, air speed was set to be 0,5 m/s, ambient temperature to 25°C, and glass emissivity to 0,95. The initial temperature of the different nanofluids was 25°C, which was also used to determine their thermodynamic properties according to the model presented in Chapter 2.

3.5.1. Heat release profile

- Heat release profile for fixed volume fraction and height:

As an example, the heat release profile on y direction for a 1 cm height volumetric receiver and with $\Delta y = 7E-5 \text{ m}$, containing either graphite or MWCNT nanoparticles suspended on different base fluids with a volume fraction of 0,01%, is shown in Figure 3.7.

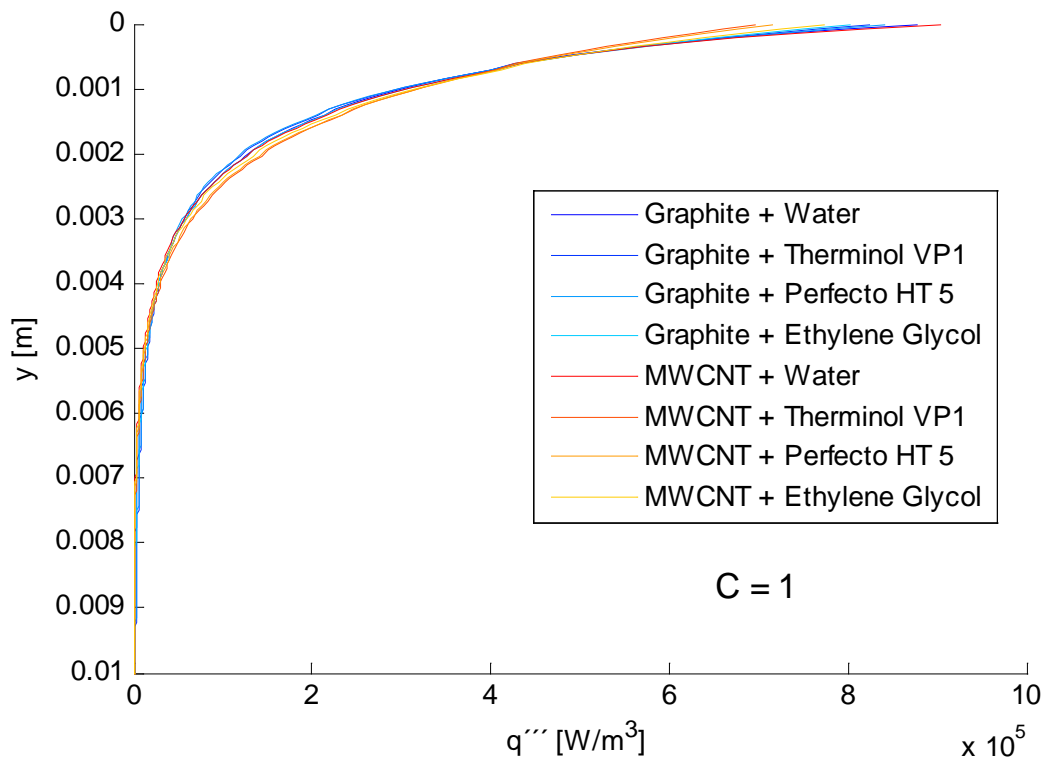


Figure 3.7 – Heat release profile ($H = 0,01 \text{ m}$; $f_v = 0,01\%$)

The results show that heat release decreases with increasing depth. This decrease was expected, since light is attenuated as it is absorbed by the nanofluid along the path. It is also visible that the different nanofluids have a very similar variation to what concerns light extinction. Note that, if solar concentration factor increases, a similar profile is obtained but the magnitude of heat release would increase while absorption efficiency remains the same. For the previous conditions of volume fraction and receiver height, Table 3.1 presents the obtained absorption efficiencies. We conclude that solid particles have the most impact on energy absorption because higher efficiencies are attained when comparing to the ones registered for different base fluids. Results also indicate that amongst the eight nanofluids, using MWCNT suspensions with water as base fluid is more convenient because the highest absorption efficiencies are achieved.

Table 3.1 – Comparison between absorption efficiency for different nanofluids (H = 0,01 m; $f_v = 0,01\%$)

$\eta_{abs}[\%]$	Graphite	MWCNT
Water	99,869	99,969
Therminol VP1	99,314	99,960
Perfecto HT 5	99,322	99,965
Ethelyne glycol	99,826	99,966

The numerical error associated to this methodology was also determined (see Eq. (9.2) in appendix III) and the obtained numerical residue values are shown in Table 3.2. Since the magnitude of the error depends on the calculated absorption efficiency, as a consequence, its impact will alter the temperature values of the volumetric receiver. Nonetheless, the numerical error reveals to be relatively small.

Table 3.2 – Numerical error for different nanofluids (H = 0,01 m; $f_v = 0,01\%$)

R [%]	Graphite	MWCNT
Water	0,1314	0,1469
Therminol VP1	0,0911	0,0484
Perfecto HT 5	0,0966	0,0521
Ethelyne glycol	0,0810	0,0695

- Heat release profile for fixed height (optimize volume fraction):

In Figure 3.8 it is shown that increasing nanoparticle's volume fraction will result in an increase of absorption efficiency, until a point where adding nanoparticles to the base fluid will not significantly increase absorption efficiency or it will reach 100%. Therefore, an optimization of volume fraction will enable to greatly reduce a lot the quantity of nanoparticles that are needed to achieve a certain absorption efficiency for a particular receiver's height.

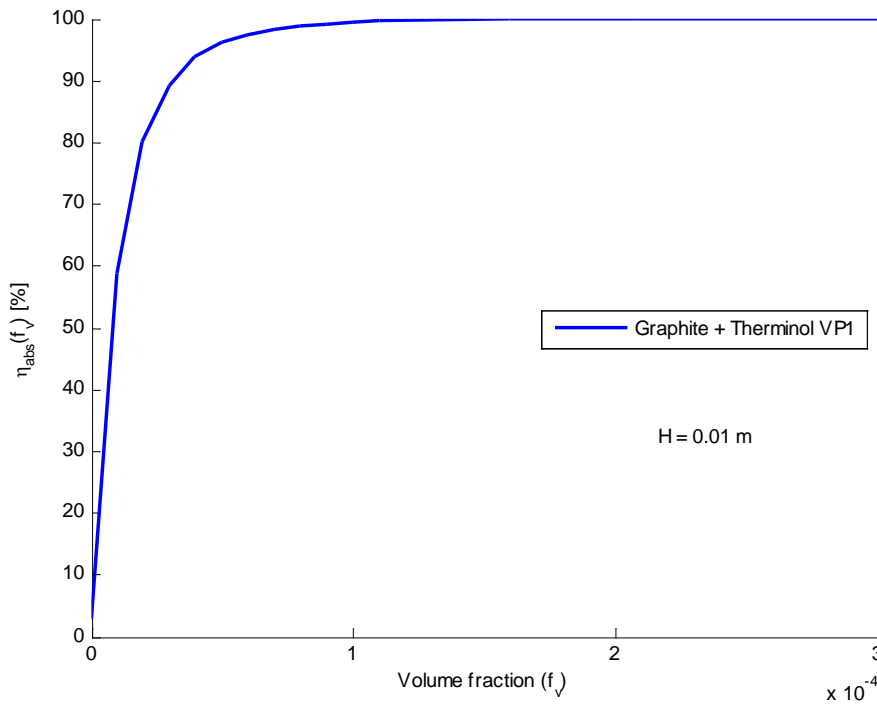


Figure 3.8 – Effect of volume fraction on absorption efficiency

Note that optimum values of volume fraction are characteristic of the receiver height and the nanofluid composition, but not the magnitude of the incident flux. To numerically determine this optimum volume fraction, both receiver height and absorption efficiency were set as independent parameters so that Newton’s method (see appendix IV) could be implemented. As expected, according to the results shown in Table 3.3, MWCNT suspended in water revealed to have properties that allow better absorption, and thus, lower volume fraction is required to achieve a given absorption efficiency.

Table 3.3 – Optimum volume fraction for 99,99% absorption efficiency (H = 1 cm; Δy = 0,006 cm)

$f_{v\ opt}[\%]$	Graphite	MWCNT
Water	0,015296	0,011499
Therminol VP1	0,027664	0,011817
Perfecto HT 5	0,027666	0,011629
Ethelyne glycol	0,016896	0,011596

As to the numerical error, calculated using Eq. (9.2) in appendix III, it is possible to realize that the residual of graphite nanoparticles is higher than the ones obtained with MWCNT. However, these values are always below 1%, so the impact is relatively small, as shown in Table 3.4.

Table 3.4 – Numerical error for different nanofluids (H = 1 cm; Δy = 0,006 cm; η_{abs} = 99,99%)

R [%]	Graphite	MWCNT
Water	0,16901	0,12471
Therminol VP1	0,54229	0,049455
Perfecto HT 5	0,55128	0,050405
Ethelyne glycol	0,1733	0,064125

The volumetric heat rate can also be represented in dimensionless form in the following way:

$$q_r = \frac{q H}{P(y = 0)} \quad (3.29)$$

where $P(y)$ is the radiative flux as function of height, see Eq. (3.2).

The impact of different heights on q_r , while maintaining a fixed absorption efficiency, has also been tested. From the example given in Figure 3.9 with an absorption efficiency of 99,99%, we conclude that the dimensionless heat release profile is invariant with channel height. The small difference between the results can be explained by the numerical residual error.

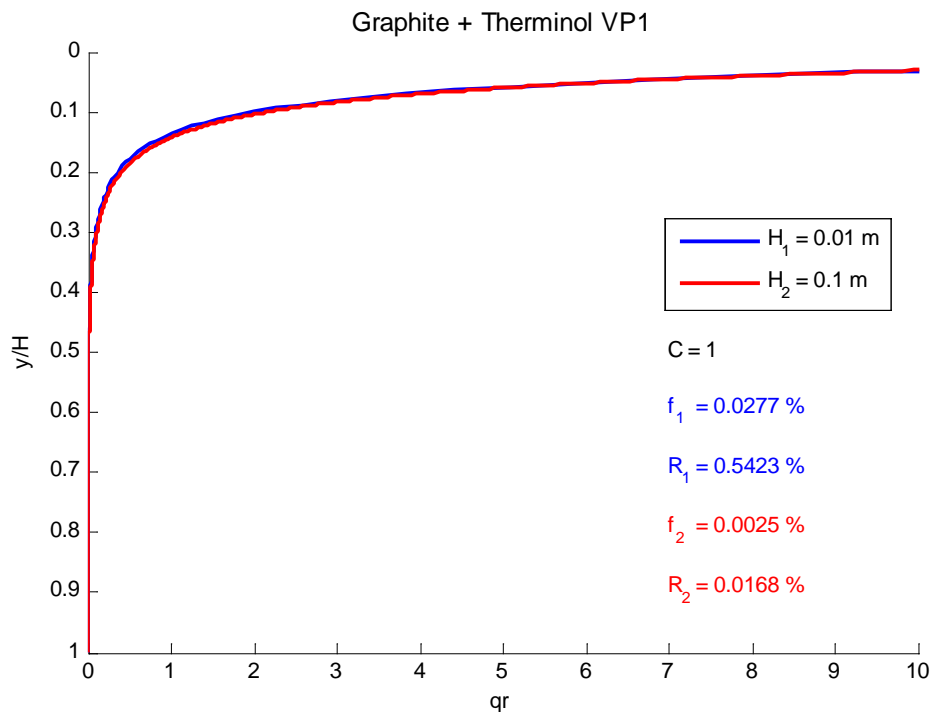


Figure 3.9 – Dimensionless heat release profile for different heights

- Heat release profile for fixed volume fraction (optimize height):

Since thermal loss was only considered through the top surface, increasing the receiver height will also increase the absorption efficiency, as shown on Figure 3.10.

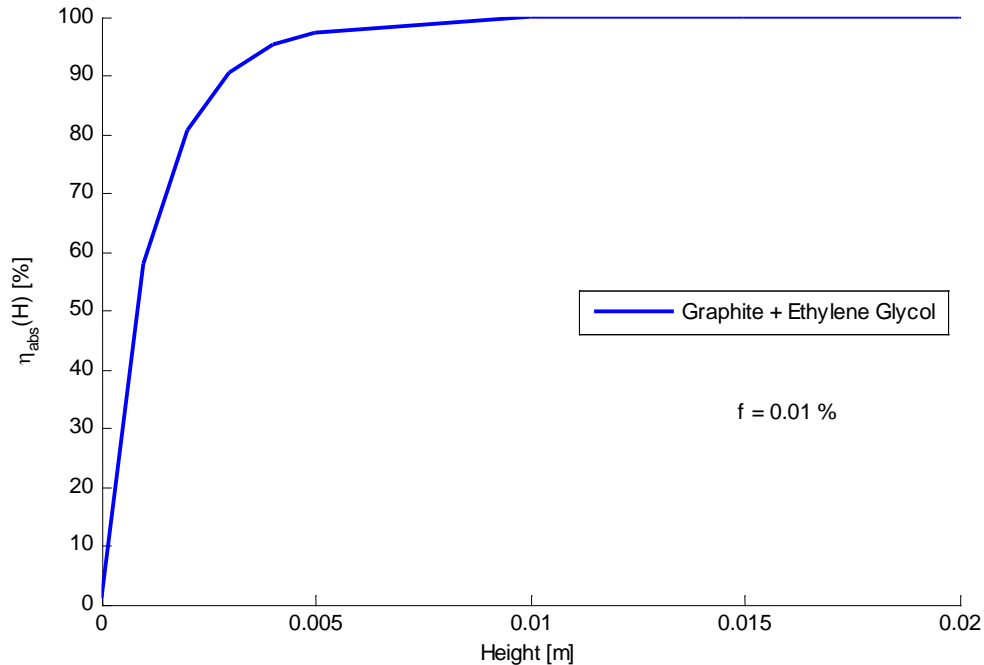


Figure 3.10 – Effect of receiver height on absorption efficiency

However, to reduce as much as possible the receiver’s size without compromising efficiency and still maintaining the same volume fraction, the same numerical method used before (see appendix IV) can also be applied, in this case, to determine the ideal receiver height (H). Results lead to the same conclusions as in Table 3.3, in which the numerical residue for the eight combinations of base fluid and particles is lower than 1% in all those cases.

3.5.2. Temperature profile

As seen until now, there are a lot of variables which, either related to the receiver geometry, nanofluid properties or atmospheric conditions, can originate a significant divergence between simulated results. To try and study the mechanisms of heat transfer inside a volumetric receiver, some variables were set as constant inputs while varying others to evaluate their impacts. Hence, the following outputs were obtained from simulations using the model described in section 3.2 and in section 3.3, by considering that 99,99% of solar radiation is absorbed by each nanofluid for a fixed receiver height of 1 cm ($\Delta y = 6E-5 m$) and for the optimum values of volume fraction of Table 3.3.

The temperature profile on a volumetric receiver is perceptible by analyzing Figure 3.11 which represents, as an example, temperature distribution on transient regime for graphite nanoparticles suspended in HTF Therminol VP1 under constant solar radiation. From these results, we can point out that before 1200 seconds (approximately), the temperature on the top surface is higher than the one on the bottom surface. However, after this instant, the temperature on the top surface becomes lower than the bottom one. This happens not only due to heat loss on the top surface, but also because the lower fluid layers keep absorbing solar radiation. Thus, conduction flux changes direction and heat transfer starts to go upwards.

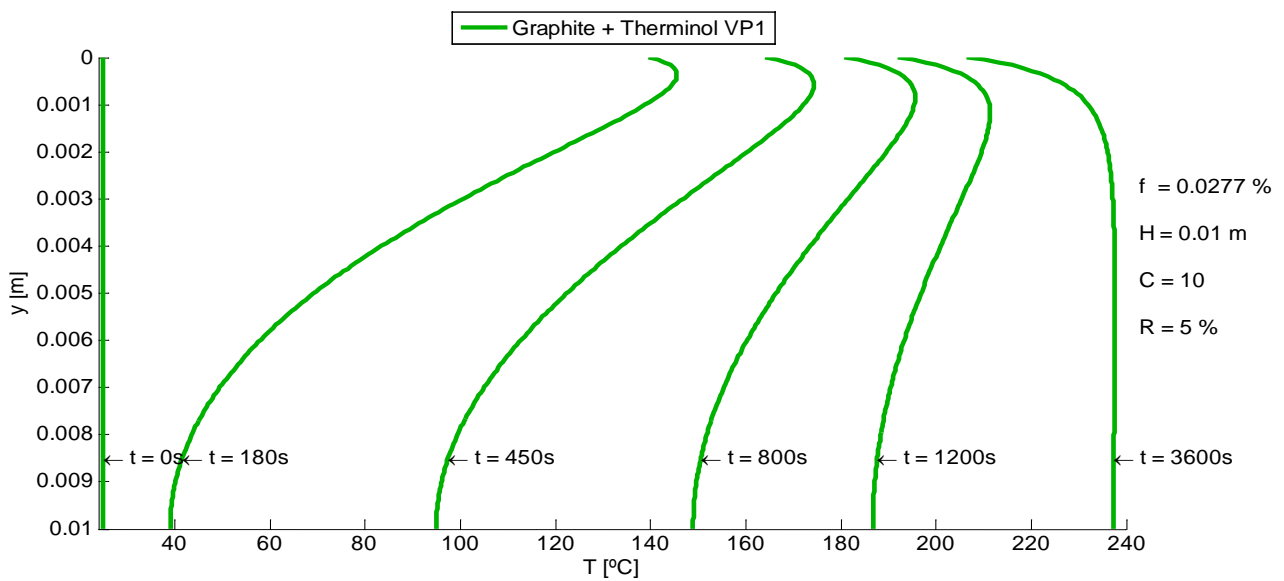


Figure 3.11 – Temperature profile in transient regime for a graphite-based receiver

Similar profiles were obtained for the remaining nanofluids, in which another example is shown in Figure 3.12, with MWCNT suspended in Perfecto HT 5 for a lower solar concentration factor.

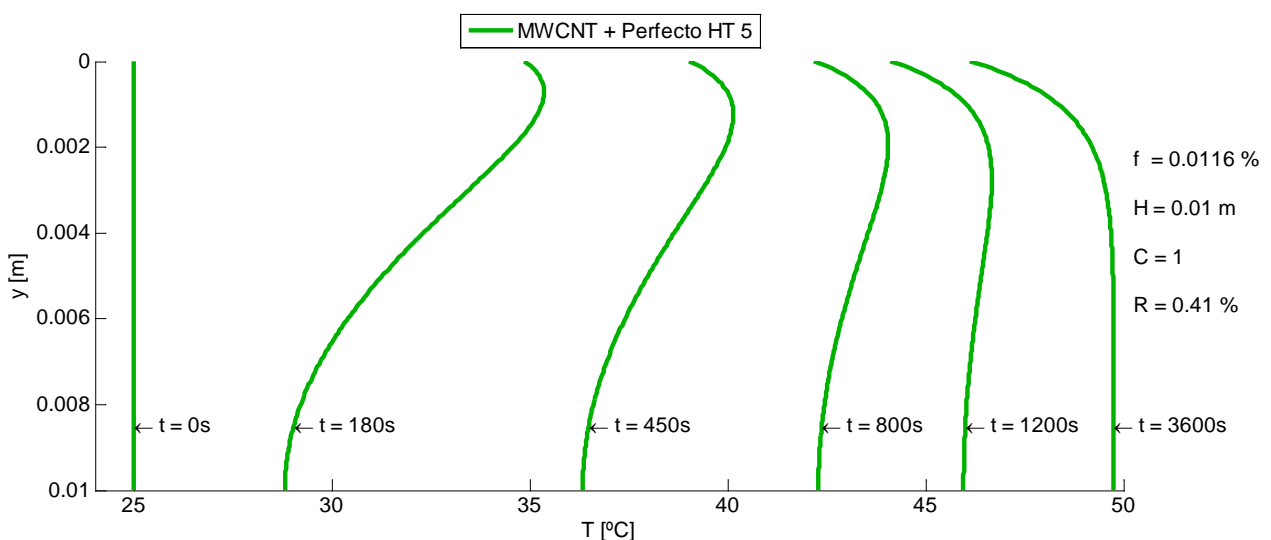


Figure 3.12 – Temperature profile in transient regime for a MWCNT-based receiver

For this case, the conduction flux changes direction approximately at 800 seconds. The temperature distribution was also represented on a coloured plot:

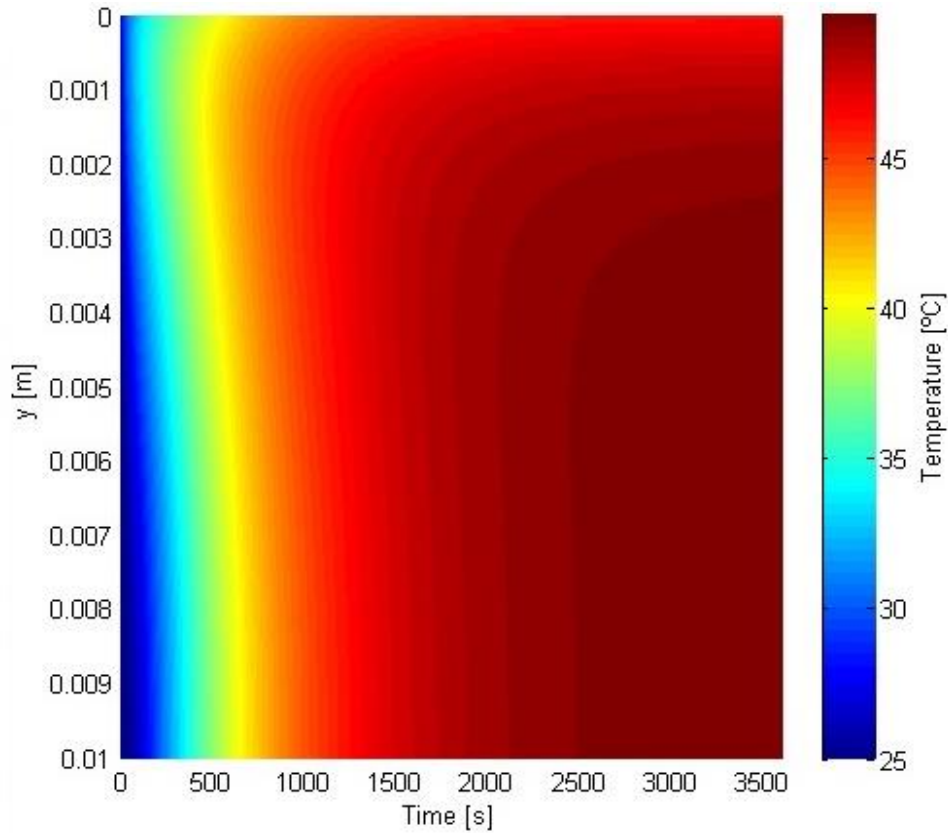


Figure 3.13 – Coloured temperature profile in transient regime for a MWCNT-based receiver

At the end of the simulated time (3600 seconds) the maximum temperatures obtained for different solar concentration factors are shown in Table 3.5.

Table 3.5 – Maximum temperature for different solar concentration factors (H = 1 cm; $\eta_{abs} = 99,99\%$; time = 1 hour)

T_{max} [°C]	C = 1	C = 2	C = 5	C = 10	C = 14
Graphite + Water	46,28	67,07	126,29 *	214,14 *	275,24 *
Graphite + Therminol VP1	49,16	72,69	139,35	237,70	306,35 *
Graphite + Perfecto HT 5	49,23	72,82	139,66	238,27	307,11
Graphite + Ethelyne glycol	48,28	71,00	135,55 *	231,19 *	298,06 *
MWCNT + Water	46,36	67,23	126,64 *	214,69 *	275,84 *
MWCNT + Therminol VP1	49,72	73,78	141,95	242,51	312,77 *
MWCNT + Perfecto HT 5	49,78	73,90	142,22	243,04	313,50
MWCNT + Ethelyne glycol	48,21	70,83	134,96 *	229,53 *	295,27 *

* Valid when considering saturated liquid (no phase change)

Although there is a numerical error associated as shown in Table 3.6, calculated using Eq. (9.4), MWCNT suspended in HTF Perfecto HT 5 present the highest values for all concentration factors. In fact, except for ethylene glycol as a base fluid, solid particles of MWCNT allow higher temperatures to be reached when compared to graphite nanoparticles.

Table 3.6 – Numerical error for different nanofluids for C = 1

R [%]	Graphite	MWCNT
Water	0,620	0,4583
Therminol VP1	4,381	0,3929
Perfecto HT 5	4,556	0,4090
Ethylene glycol	0,9086	0,3377

From these results we can also point out that by increasing the concentration factor of solar radiation it will increase the steady state or stagnation temperature on all nanofluids. For lower concentration factors, the difference between maximum temperatures of each fluid is relatively small. However, for higher values of solar concentration, this difference is amplified and it can reach values as high as 40°C. This can be easily perceived by looking at the results shown below.

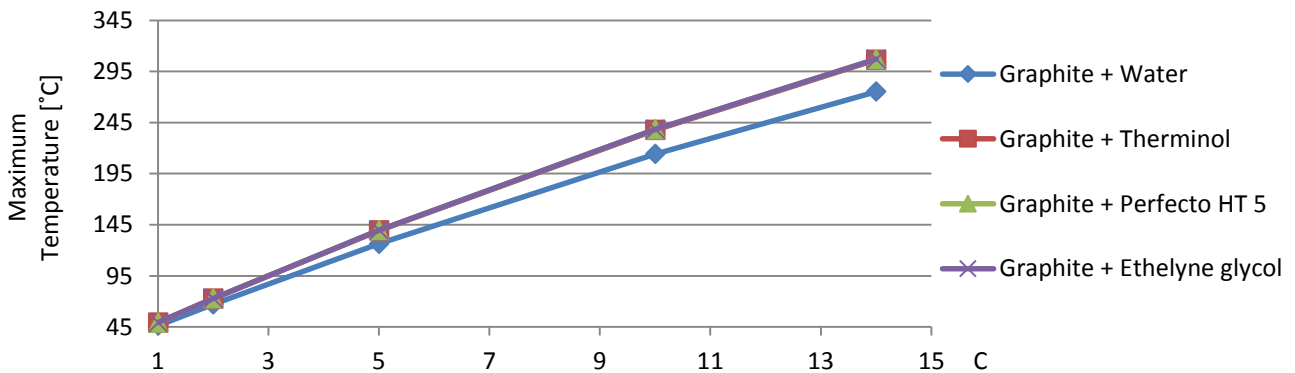


Figure 3.14 – Variation of maximum temperatures with different concentration factors for a graphite-based receiver

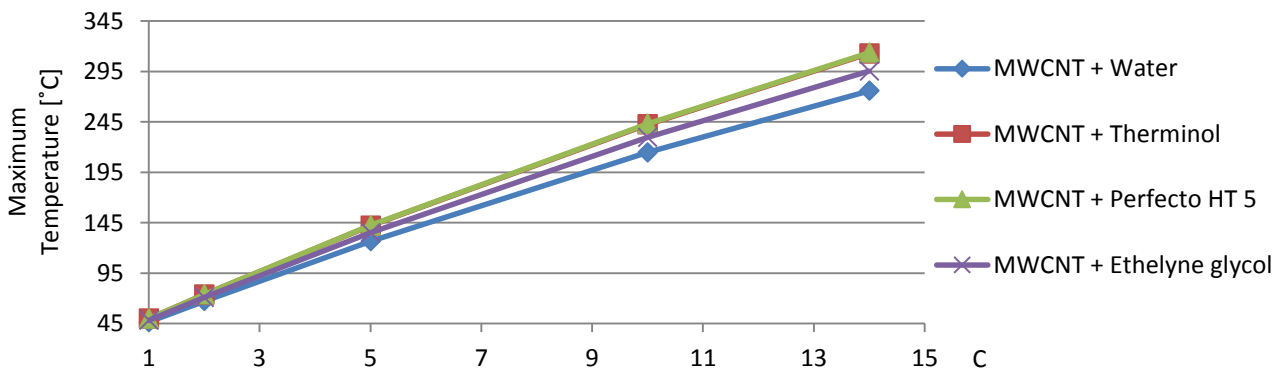


Figure 3.15 – Variation of maximum temperatures with different concentration factors for a MWCNT-based receiver

Having the temperatures of each nanofluid on transient regime, we can now study the variation of the total accumulated energy gain on the receiver and the total accumulated energy loss through the top surface. It is important to recall that on every instant, the sum of these energies equals the integrated solar radiation absorbed. As an example, obtained results are shown in Figure 3.16. Since the absorption efficiency is 99,99%, the absorbed energy line is almost over the incident radiation line. Note that energy gain over time leans towards a horizontal line and, as a consequence, heat losses will also become constant and thus accumulated energy loss tends to be parallel to the accumulated absorbed solar radiation.

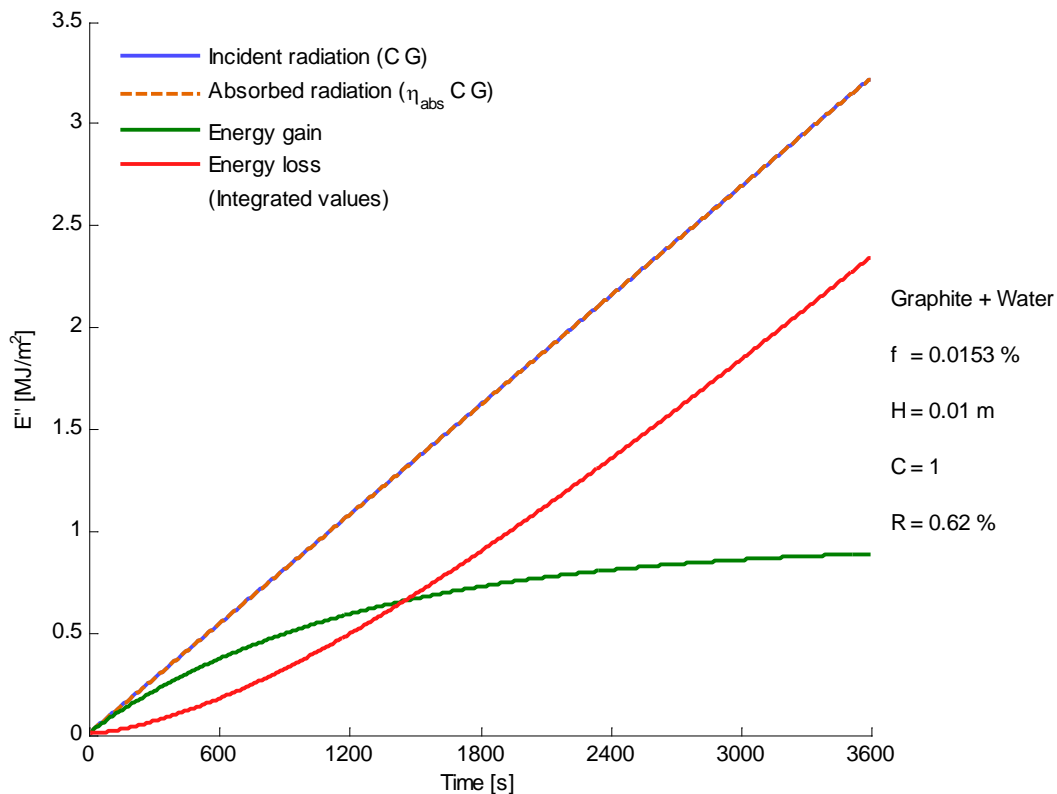


Figure 3.16 – Variation of accumulated values of energy gain and loss

According to the nanofluid at stake, the magnitude of both integrated energy gain and energy loss will determine the collector's efficiency. When comparing these efficiencies in transient regime (see Figure 3.17), during a long period of time, base fluids with MWCNT suspensions present higher efficiencies than those with graphite nanoparticles. As to the base fluids, thermal oils reveal to have less efficiency compared to water and ethylene glycol. Note that, for the first instant ($t = 0$ s) efficiency equals zero since the temperatures of nanofluids are equal to ambient temperature.

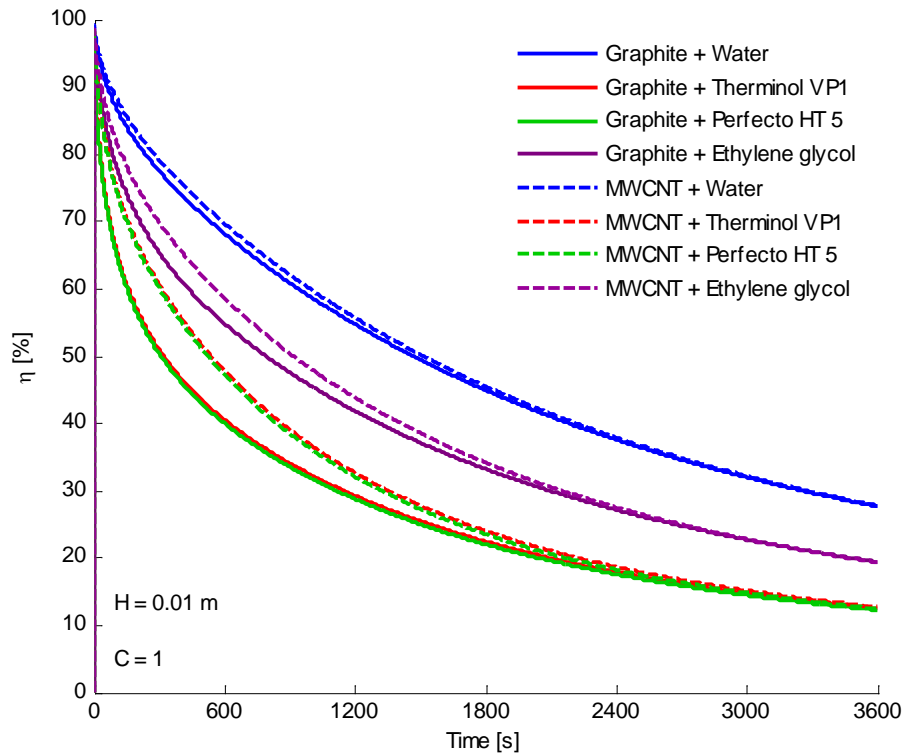


Figure 3.17 – Variation of efficiency on different nanofluids

However, when analyzing efficiencies obtained in the last second of the simulation time, results shown in Table 3.7 demonstrate a great similarity between solid particles with the same base fluid. Once again, MWCNT present the highest efficiencies, except when suspended on ethylene glycol.

Table 3.7 – Receiver efficiency for different solar concentration factors ($H = 1 \text{ cm}$; $\eta_{\text{abs}} = 99,99\%$; time = 1 hour)

η [%]	C = 1	C = 2	C = 5	C = 10	C = 14
Graphite + Water	27,522	27,206	26,204 *	24,464 *	23,133 *
Graphite + Therminol VP1	12,393	12,230	11,725	10,897	10,289 *
Graphite + Perfecto HT 5	12,114	11,954	11,461	10,651	10,057
Graphite + Ethylene glycol	19,298	19,060	18,316 *	17,069 *	16,133 *
MWCNT + Water	27,632	27,311	26,292 *	24,524 *	23,153 *
MWCNT + Therminol VP1	12,582	12,413	11,893	11,044	10,425 *
MWCNT + Perfecto HT 5	12,292	12,127	11,620	10,791	10,187
MWCNT + Ethylene glycol	19,226	18,977	18,202*	16,907 *	15,942 *

* Valid when considering saturated liquid (no phase change)

From these results, we can also point out that when increasing the solar concentration factor, the receiver's efficiency decreases. This behaviour is consistent in all eight fluids. As a matter of fact, efficiency will tend to zero as the solar concentration factor or the simulation time are increased. The reason for this can be explained by the fluid that will reach a stagnation point of temperature. That is, when the thermal heat losses to ambient become equal to the energy absorption from incident solar radiation. As a result, from that instant ahead the fluid has no energy gain and its temperature remains constant over time. Since efficiency was calculated using Eq. (3.28), under stationary conditions the numerator is constant (on every point of the receiver), but the denominator value increases with time. Therefore, efficiency tends to zero.

When comparing both maximum temperatures and efficiencies, according to the results, using MWCNT revealed not only a temperature gain but also an efficiency increase, except for ethylene glycol as base fluid, where graphite nanoparticles demonstrate better performance than MWCNT.

4. COMPARISON BETWEEN SURFACE-BASED AND NANOFUID-BASED RECEIVERS

In this chapter a comparison is made between the numerical results of a nanofluid-based receiver and a surface-based receiver, both in transient regime under stationary conditions.

4.1. Surface-based receiver modelling

The surface-based receiver model is similar to that of the previous chapter, since it was adapted from that case. A schematic is shown in Figure 4.1, in which the incident radiation flux (G), heat loss to the environment (q_{loss}) and receiver height (H) represent the same quantities as in Figure 3.1.

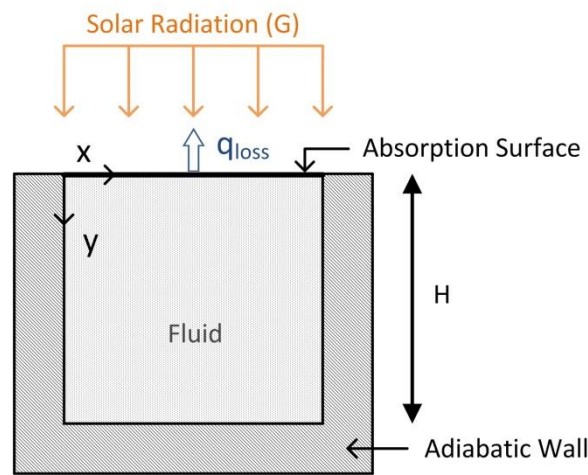


Figure 4.1 – Schematic for model formulation of a surface-based solar receiver

Similarly to the studied case of a volumetric receiver, in the absence of nanoparticles, the same assumptions are valid except for the glass cover that is now replaced by an absorption surface. The surface thickness was neglected on the numerical model and its transmissivity was assumed equal to zero.

Given these assumptions, the fluid temperature profile on a surface-based receiver can be obtained by solving the same energy balance equation obtained before, Eq. (3.8). However, in this model there is no heat generation to consider, resulting in:

$$\rho c_p \frac{\partial T}{\partial t} + k \frac{\partial^2 T}{\partial y^2} = 0 \quad (4.1)$$

where ρ is the density, c_p the specific heat capacity, and k the thermal conductivity of the fluid.

The explicit method and the resulting equations used on the volumetric receiver model can also be applied to numerically solve the second order differential equation (4.1) in the case of a surface-based receiver. However, some particularities should be considered in this model besides neglecting the heat generation. Since there are no solid particles at stake, the volume fraction should be set equal to zero when determining the thermodynamic and transport properties of the fluid. Additionally, in the energy balance equation regarding the boundary condition of the top surface, a constant heat flux must be imposed in order to consider the solar radiation absorption by the plate (q_{plate}), as shown in Figure 4.2:

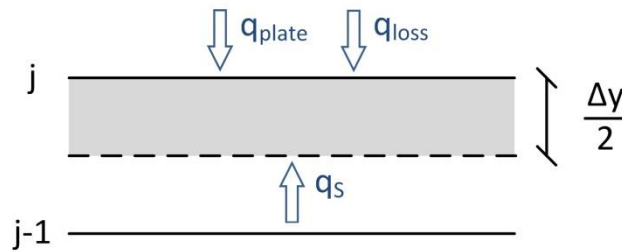


Figure 4.2 – One-dimensional mesh for top plane on a surface-based receiver

In this way, Eq. (3.16) becomes as follows:

$$m c_p \frac{dT}{dt} = q_{plate} + q_{loss} + q_s \quad (4.2)$$

where,

$$q_{plate} = G \alpha \quad (4.3)$$

$$q_{loss} = (h_{conv} + h_{rad}) \Delta x \Delta w (T_{amb} - T_j) \quad (4.4)$$

$$q_s = \frac{k \Delta x \Delta w (T_{j-1} - T_j)}{\Delta y} \quad (4.5)$$

Substituting the plate flux, heat loss flux and q_s in Eq. (4.2) an equation to determine temperature for the top surface is deduced resulting in the following form:

$$T_j^{k+1} = \frac{q_{plate} 2 \Delta t}{\rho c_p \Delta y} + 2 Fo (T_{j-1}^k + Bi T_{amb}) + T_j^k (1 - 2 Fo - 2 Fo Bi) \quad (4.6)$$

where Fo is the Fourier number, and Bi is the Biot number, calculated respectively using Eq. (3.15) and Eq. (3.20).

- Numerical results for a surface-based receiver:

The numerical method was implemented in *Matlab* in order to obtain the temperature profile on a 1 cm height surface-based receiver ($\Delta y = 6E-5 \text{ m}$) under constant radiation conditions and during a time period of 3600 seconds (1 hour). It was considered that the absorption surface has a selective coating of blackened nickel with an absorptivity that can go as high as 0,97 and an emissivity of 0,18 [33]. The model was solved for a receiver containing one of four different fluids (pure water, Therminol VP1, Perfecto HT 5 and Ethelyne glycol) and the efficiency for each one was determined. The following outputs result from simulations considering an input of collimated solar radiation at the top of the receiver ($y = 0$) equal to AM1.5 Direct distribution [30] for a wavelength range from 280 nm to 2500 nm. As to the environmental conditions, air speed and ambient temperature were set to be constant over time, with a magnitude of, respectively, 0,5 m/s and 25°C. The initial temperature of the different fluids was 25°C, which was also used to determine their thermodynamic properties.

According to the simulation outputs (for constant solar radiation), under no circumstance the temperature on the bottom surface was superior to the one on the top surface, and hence, heat flux always points downwards. As an example, Figure 4.3 presents the temperature profile for a receiver containing Therminol VP1 at different moments of the simulation. It is clearly shown that maximum temperatures are located at the top of the receiver ($y = 0$), and minimum temperatures at the bottom ($y = H$).

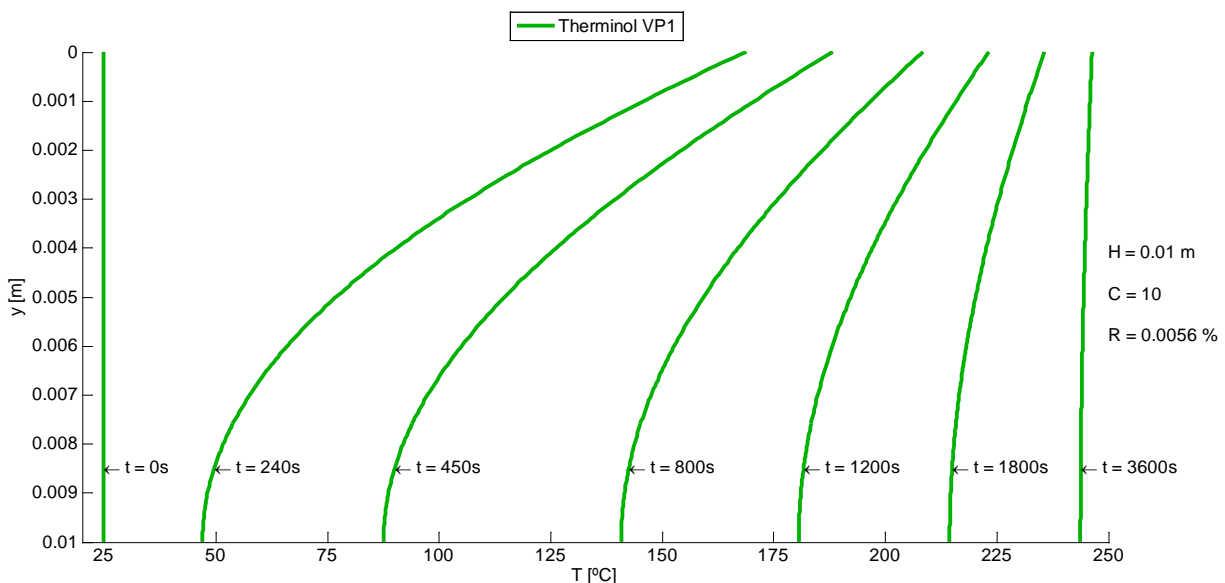


Figure 4.3 – Temperature profile on transient regime for a selective surface-based receiver

Equally, in Figure 4.4 the same result is demonstrated, but temperature is represented on a coloured surface in a three-dimensional graph.

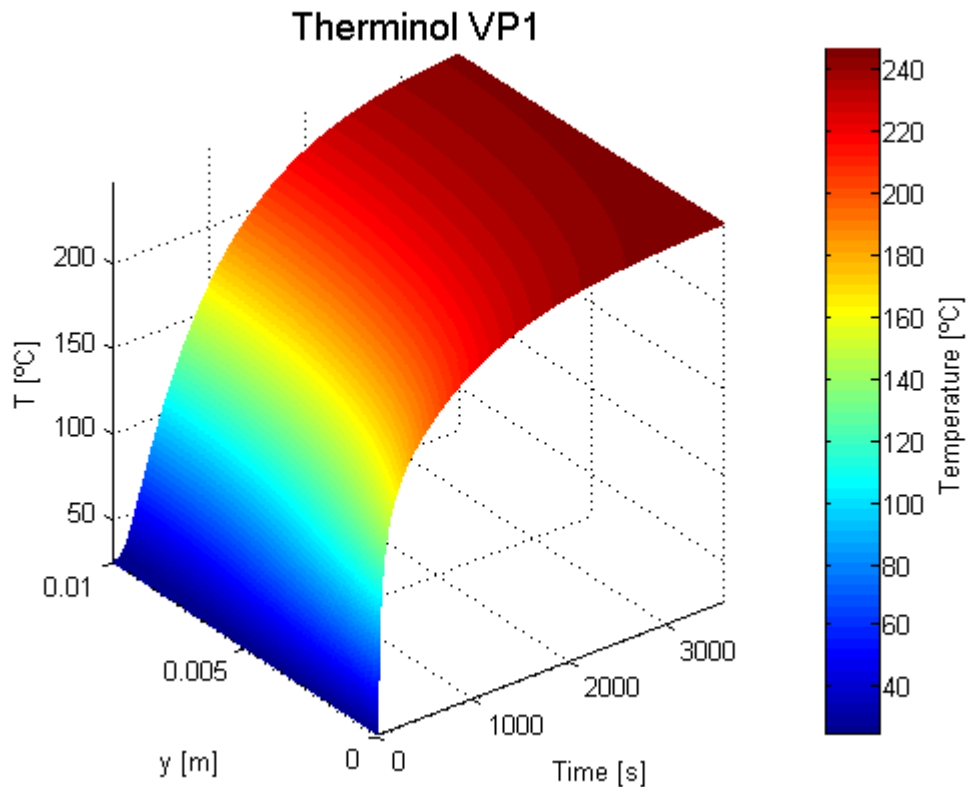


Figure 4.4 – Three-dimensional temperature profile on transient regime for a selective surface-based receiver

For a given moment on the transient regime, there will also be a minimum temperature of the fluid. The location of both maximum and minimum temperatures will determine the temperature profile and respective efficiency. As said before, convection heat transfer was neglected on this model, mainly because heat transfer through conduction is the predominant mechanism which is responsible for transferring the absorbed energy from the surface to the fluid. Since the thermal conductivity of the fluids at study is relatively low, this energy transfer process is not very effective, resulting in a notable temperature distribution along the y direction.

Results presented in Table 4.1 demonstrate a great similarity between each fluid maximum temperature at the end of the simulation time. This resemblance occurs in all the different solar concentration factors, where Perfecto HT 5 thermal oil reaches the highest temperatures and pure water the lowest temperatures. It is also possible to notice that increasing the solar concentration factor will cause the maximum temperature to rise in a linear way, as shown in Figure 4.5.

Table 4.1 – Maximum temperatures for different concentration factors of a surface-based receiver

T_{max} [°C]	C = 1	C = 2	C = 5	C = 10	C = 14
Pure water	47,01	68,90	133,63 *	237,56 *	316,22 *
Therminol VP1	48,18	71,18	138,92	246,47	326,64 *
Perfecto HT 5	48,19	71,21	138,98	246,58	326,76 *
Ethelyne glycol	47,80	70,44	137,23	243,68 *	323,42 *

* Valid when considering saturated liquid (no phase change)

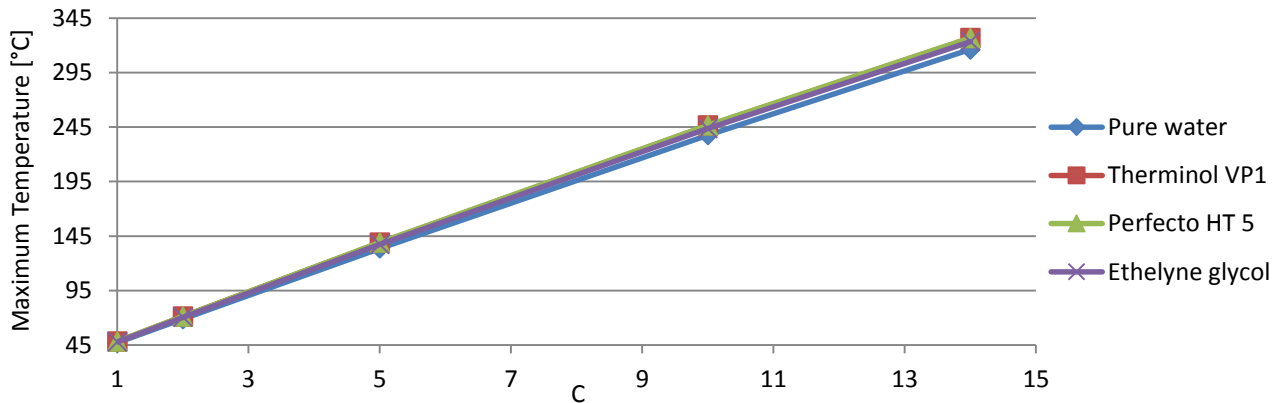


Figure 4.5 – Variation of maximum temperatures with different concentration factors

Now, taking water as an example, in Figure 4.6 it is possible to see the variation of the total absorbed solar radiation, the accumulated energy gain and total accumulated losses of energy to ambient through convection and radiation heat transfer.

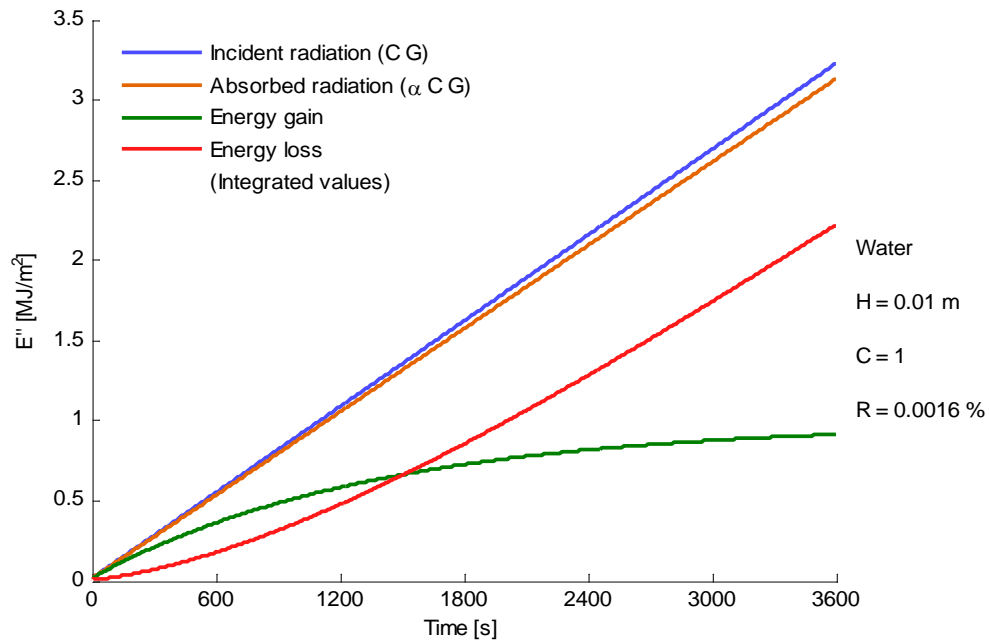


Figure 4.6 – Variation of accumulated values of energy gain and energy loss

These results suggest that before the intersection of energy gain and energy loss curves, efficiency is superior to 50%, and after that moment, efficiency starts to become lower than 50% because energy loss is higher than accumulated energy. This decrease of efficiency over time is verified on all fluids by looking at the outputs from the numerical simulation shown on Figure 4.7. When comparing efficiencies between each fluid, results show a significant discrepancy. On every instant, pure water presents the highest efficiency values and Perfecto HT 5 the lowest. This happens because the specific heat capacity of water is higher when compared with the other fluids in this study. Thus, we can conclude that the fluid with more stored energy (higher specific heat capacity) is the most efficient. It was also verified that at the initial instant ($t = 0$ s) efficiency equals zero for every fluid because their temperatures are equal to ambient temperature (energy accumulated equals zero).

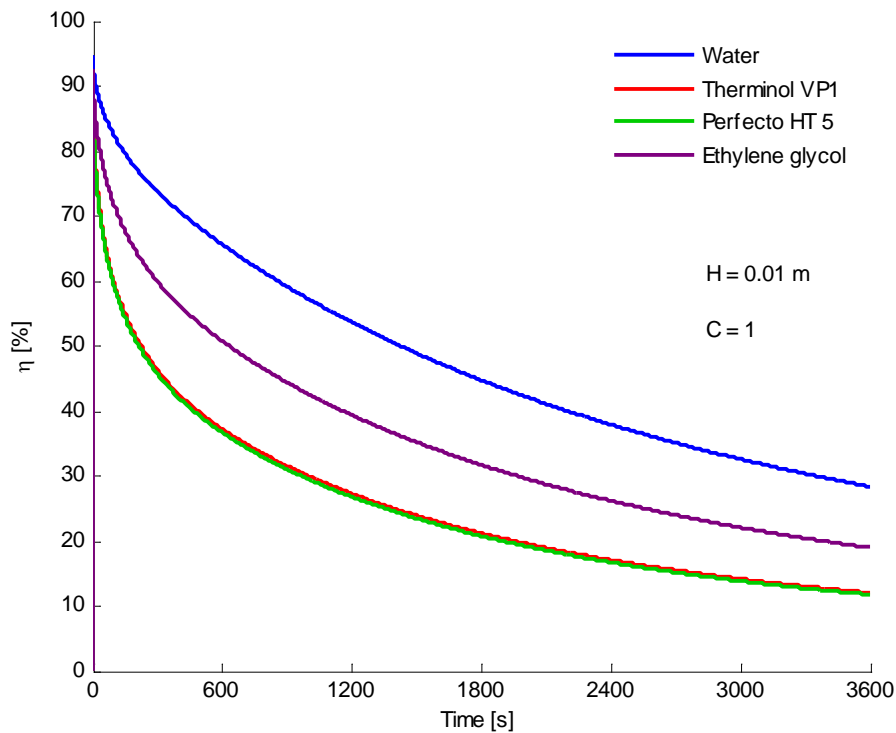


Figure 4.7 – Variation of efficiency on different fluids

To study the impact of solar concentration factor on the receiver's efficiency, Table 4.2 shows the efficiencies obtained for the different fluids at the last instant (3600 seconds) of the simulation. As verified before, the increase of solar concentration factor is responsible for the diminishing of efficiency because the nanofluid temperature is reaching a stagnation point.

Table 4.2 – Comparison between fluids efficiency for different concentration factors for a surface-based receiver after 1 hour of operation

η_{abs} [%]	C = 1	C = 2	C = 5	C = 10	C = 14
Pure water	28,25	28,17	27,90 *	27,32 *	26,76 *
Therminol VP1	11,88	11,83	11,68	11,36	11,06 *
Perfecto HT 5	11,59	11,55	11,40	11,09	10,79 *
Ethelyne glycol	18,82	18,76	18,54	18,08 *	17,64 *

* Valid when considering saturated liquid (no phase change)

Although it is important to convert solar radiation into thermal energy as efficiently as possible, the aim should be to achieve the highest possible temperature while maintaining high efficiency. Note that when comparing fluids from Table 4.1 and Table 4.2, the ones with higher temperatures have the lower efficiencies and vice versa.

The previous results have a numerical error associated which is consequent from the explicit method. This error was determined using Eq. (9.4) and it was found that, although it increases with solar concentration factor, the highest value amongst all fluids corresponds to 0,0056%.

4.2. Comparison of results

It is important to clarify that for the comparison between volumetric and surface-based receivers, the same conditions were maintained, that is, receiver height, environmental conditions, simulation time and mesh discretization. Though, once volumetric receivers allow adjusting how much solar energy is absorbed, simulated results were compared considering an absorption efficiency of 99,99%, while for surface-based receivers absorption efficiency was set to be 97%, which is the typical value of a blackened nickel selective surface [33].

Solar selective surface-based receivers are highly efficient in capturing the incident solar energy due to high absorptivity of the surface. However, in the absence of convective heat transfer, the distribution of this absorbed energy into the HTF as thermal energy is not a very efficient process because of the low thermal conductivities of the studied fluids ($0,13 - 0,61 \text{ W/m K}$). As presented in Figure 4.8, higher temperatures are located on the top surface of the receiver and lower temperatures on the bottom.

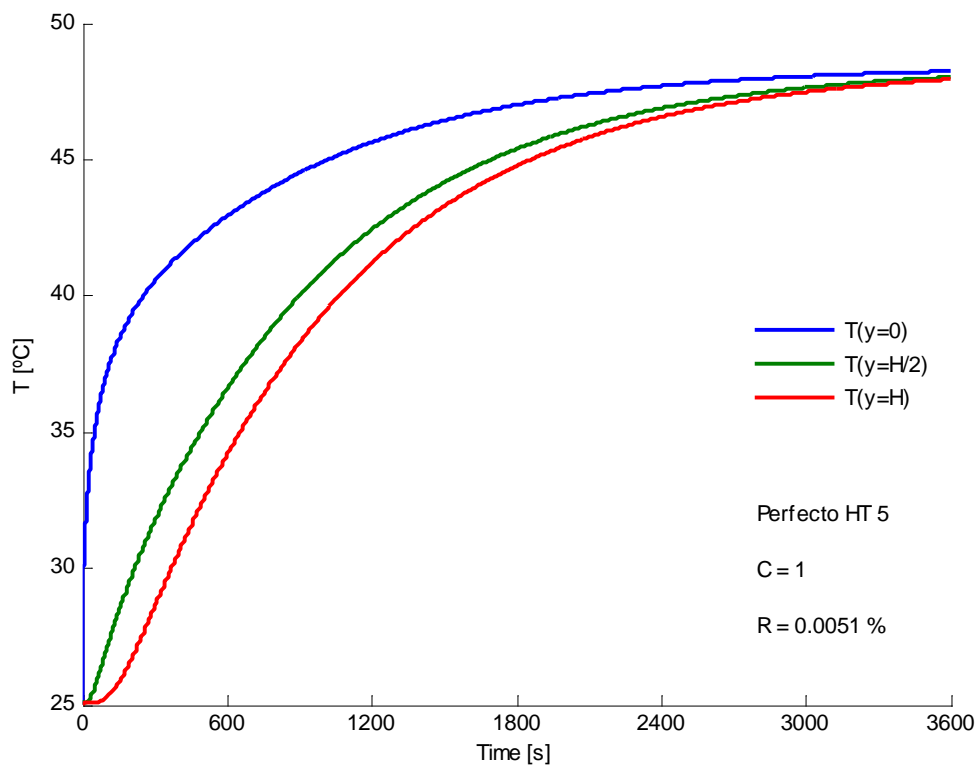


Figure 4.8 – Variation of temperature on transient regime for a surface-based receiver

On the other hand, although the thermal conductivity of solid particles on a volumetric receiver is significantly higher when compared to the ones that are characteristic of the base fluids under study, the impact on the thermal conductivity of the nanofluid is relatively small. This happens

because the solid particles volume fraction is also small. Therefore, the main factor responsible for the higher temperatures near the bottom surface (see Figure 4.9) is due to the volumetrical absorption of solar radiation.

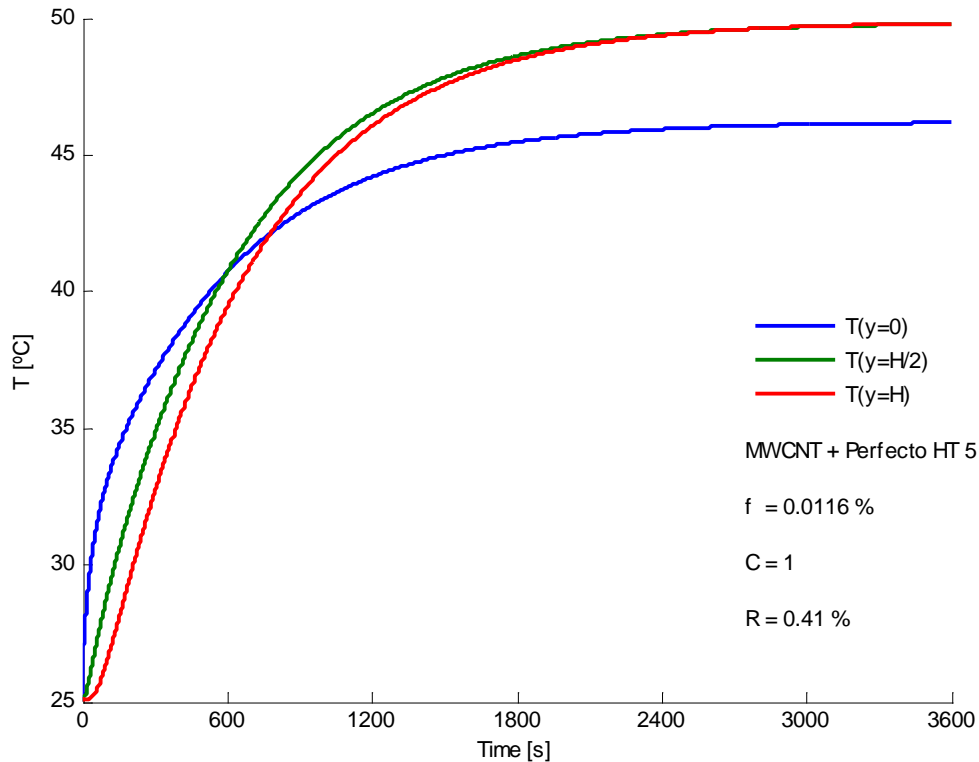


Figure 4.9 – Variation of temperature on transient regime for a nanofluid-based receiver

These receivers not only absorb most of the solar radiation but, as opposite to surface-based receivers, they can efficiently distribute the thermal heat on the working fluid. However, when comparing Table 3.7 (for optimal values of volume fraction) with Table 4.2, the difference between efficiencies on these two types of receivers is almost negligible. This similarity also occurs when comparing temperatures at the end of the simulation. The reason for these results can be explained by the fact that the emissivity of a selective surface-based receiver is significantly lower than that of a nanofluid-based receiver ($0,18 \ll 0,95$). Nonetheless, the thermal heat distribution on a volumetric receiver suggests that better performance could be obtained under flowing conditions.

5. EXPERIMENTAL STUDY ON NANOFLUIDS

The aim of this experimental study was not to replicate the environmental conditions and solar concentration levels that would be typical of a central-receiver design in real applications, but to experimentally demonstrate the concept of a nanofluid volumetric receiver, study the effect of solar radiation collection and investigate the temperature profile in different nanofluids. There is a great variety of nanofluids that can be used on volumetric solar receivers, however, in this chapter, special focus was given to four of the nanofluids previously studied in the numerical model. Analyzing the performance of each nanofluid on a similar configuration used in the one-dimensional heat transfer model, will allow the comparison between the experimental and numerical models. Figure 5.1 shows the main components of the experimental setup, including the solar simulator, cylindrical volumetric receiver, thermocouple array and data acquisition system.

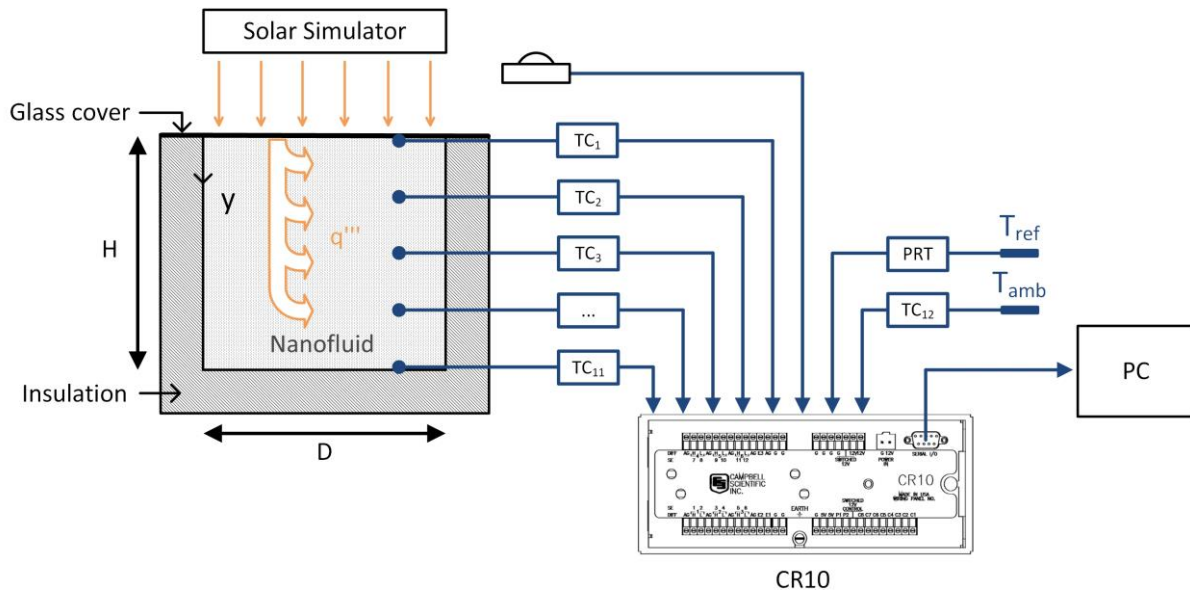


Figure 5.1 – Schematic of the experimental setup

5.1. Equipment characteristics

5.1.1. Datalogger

The data acquisition system used for the experimental study measurements is composed by a CR10 measurement and control module (datalogger) from *CAMPBELL SCIENTIFIC, INC.* and a computer with the appropriate software to communicate with the CR10. On one hand we have the CR10 module which is responsible for the measurement and storage of all signals on its internal memory. A AM416 multiplexer was added and connected to the CR10 to increase the number of available

channels [34]. On the other hand, we have the *PC200W* software running in a computer which is necessary to program the reading configurations, as well as to program the desired wiring configuration. This software can also retrieve data from the CR10 internal memory and effectuate calculations.

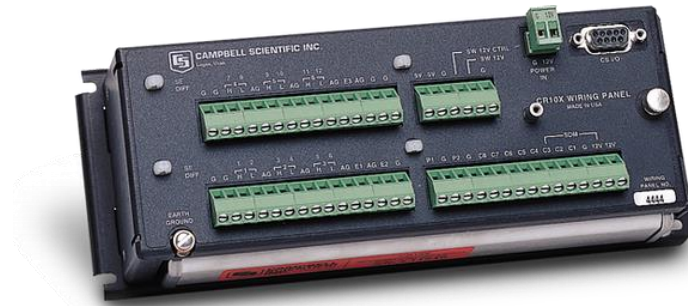


Figure 5.2 – CR10 Datalogger [35]

Although the readings step time was set to be 5 seconds, the output of the CR10 is a 1 minute and 10 minutes average. For more details on measurement configurations, see appendix V.

5.1.2. Temperature sensors

- **Thermocouple (TC):**

A thermocouple is a simple device with the objective of measuring temperatures. It is composed of two dissimilar conductor wires that contact each other typically in two points, thus forming two junctions. When one of these junctions is exposed to a temperature that is different from the temperature of the other junction, an electric potential difference is produced. This voltage can be measured by the datalogger and then converted to a temperature. In this experimental study, the thermocouples were made by using a copper and constantan alloy (type T), as shown in Figure 5.3, which are suitable for measurements in the -200 to 350°C range [36]. All the reference temperature junctions of the different TCs are immersed in the same water container. In this way, the reference temperature oscillations can be minimized. The container is also protected from light and exposed to relatively stable indoor ambient temperature. The TCs were calibrated by comparing the measured values with the ones obtained with a Platinum Resistance Thermometer (PRT).

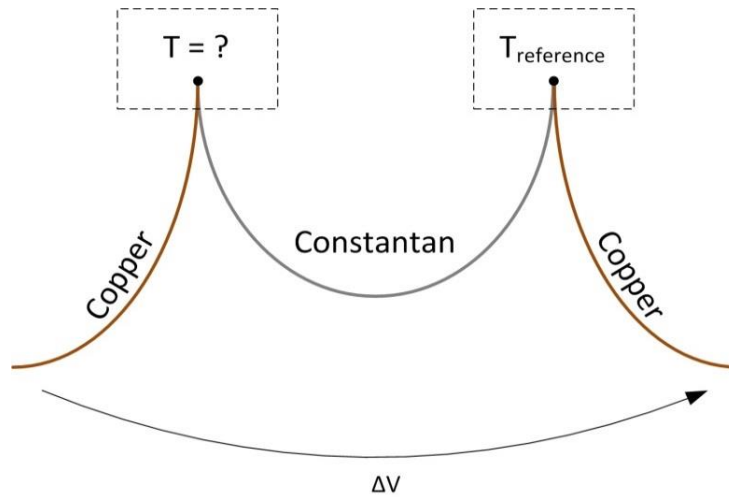


Figure 5.3 – Thermocouple (type T)

• **Resistance temperature detector (RTD):**

To measure the reference temperature for the TCs, a RTD was used because it has greater stability, accuracy and repeatability when compared to TCs. The principle of operation of these types of thermometers is to measure the electrical resistance of the RTD metallic element and convert it into a temperature value. For this experimental apparatus a platinum sensor (PRT) was used with a resistance of 100 ohms at 0°C (PT100). In order to determine the resistance, an electric difference potential also called excitation voltage, has to be imposed. In one way, excitation voltage should be increased to maximize the measurement resolution but, on the other hand, it should be decreased to minimize self-heating of the platinum wire. To compensate for lead wire resistance, the PRT was connected to the datalogger with a 3 wire half bridge configuration, as shown on Figure 5.4.

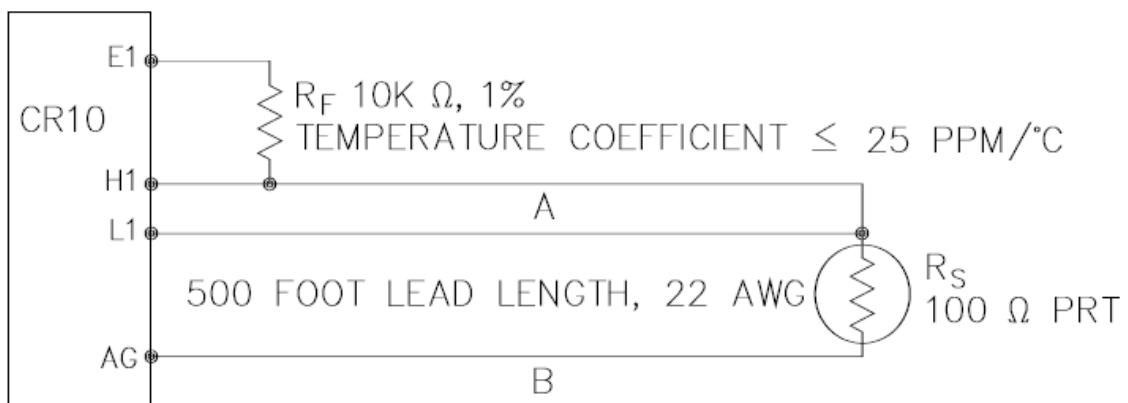


Figure 5.4 – Connection diagram of a 3 wire half bridge configuration of a PT100 [34]

When programming this connection on the datalogger, the range of sensor voltage (V_{range}), the multiplier value, and the excitation voltage (V_x) must be introduced. A standard value of 25 mV was found to be adequate for the measurement range of the sensor voltage, while the multiplier value was obtained by the ratio:

$$\frac{R_{F\ measured}}{R_0} = \frac{9980\ \Omega}{100\ \Omega} = 99,8 \quad (5.1)$$

In which R_F is the resistance value measured on the 10 k Ω resistor and R_0 is the resistance of platinum at a temperature of 0°C.

The maximum allowable excitation voltage to tolerate a 25 mV measurement range can be determined using the following expression [34]:

$$V_{range} > V_x \frac{R_{S\ max}}{R_{F\ min} + R_{S\ max}} \quad (5.2)$$

where $R_{S\ max}$ represents the PT100 resistance at the predicted maximum temperature that the probe is going to measure, and $R_{F\ min}$ represents the lowest resistance given by the resistor tolerance. Since the PT100 is measuring the temperature of the water that is exposed to indoor ambient temperature, the predicted maximum temperature is 30°C which corresponds to a resistance of 111,67 Ω . The 10 k Ω resistor has a tolerance of 1%, therefore the minimum resistance is 9900 Ω . Using Eq. (5.2) it was found that excitation voltage should be lower than 2232,1 mV.

The output from the CR10 is actually the ratio between R_S and R_0 so it is necessary to use Eq. (5.3) defined in IPTS-68 standard to convert this value on a temperature.

$$T = \frac{-a + \sqrt{a^2 - 4 b \left(\frac{R_S}{R_0}\right)}}{2 b} \quad (5.3)$$

where,

$$a = 3,90802 * 10^{-3} [^{\circ}\text{C}^{-1}]$$

$$b = -5,80195 * 10^{-7} [^{\circ}\text{C}^{-2}]$$

5.1.3. Pyranometer

A pyranometer is a device with a 180 degrees field of view, used to measure the global solar irradiance on a planar surface. When connected to a datalogger, the output signal is a voltage measurement that is directly proportional to the incoming irradiance. Therefore, dividing the measured signal by the calibration constant (pyranometer sensitivity provided with each instrument) will result on irradiance in power per square meter.

In this experiment, the pyranometer is placed between the receiver and the solar simulator, on a horizontal position, in order to measure the solar simulator irradiance. An Eppley 8-48 pyranometer model from *The Eppley Laboratory, Inc.* was used [37]. It is classified as a second class pyranometer for global radiation measurements according to ISO 9060 (1990) [38]. This model has a glass cover that is capable of uniformly transmit radiation from wavelengths between 285 and 2800 nm [37].



Figure 5.5 – Eppley 8-48 pyranometer [37]

This particular instrument has been recalibrated according to the ISO 9847:1992 standard [39], using a Kipp & Zonen CMP11 (secondary standard) calibrated reference pyranometer. Sixteen calibration series were taken on 27/02/2015 and the obtained calibration constant was $11,50 \mu V / (W / m^2)$.

5.1.4. Volumetric receiver

The volumetric receiver has a cylindrical shape with a total capacity of 300 ml. It is thermally isolated in the side and bottom surfaces, however, a space was left in the insulation so that the thermocouples could penetrate horizontally through the receiver. The thermocouples are equally distributed in the vertical direction and take measurements of the nanofluid temperature in the center of the receiver. Figure 5.6 shows the geometrical dimensions and Figure 5.7 the receiver used in the experimental setup. Note how a piece of black cardboard was placed on the top of the container to make sure that thermocouples are not heated by direct radiation.

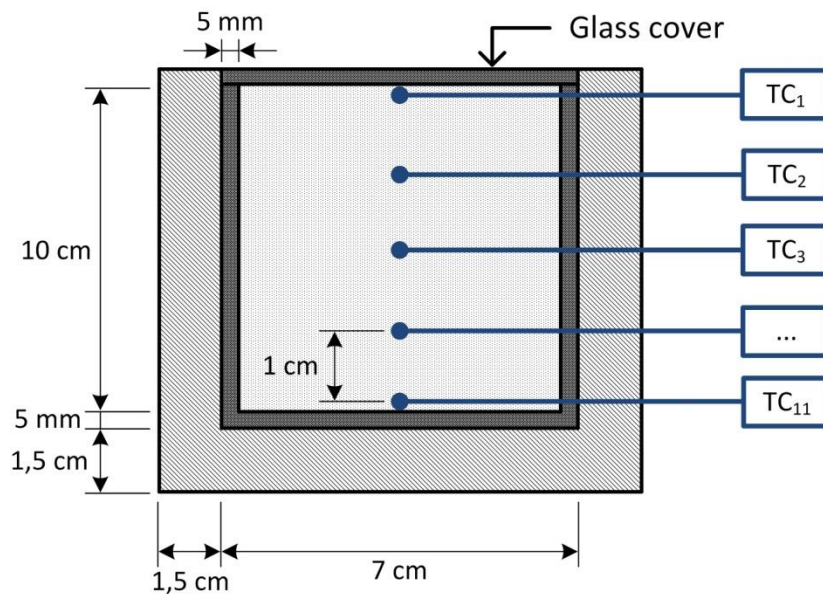


Figure 5.6 – Volumetric receiver schematic

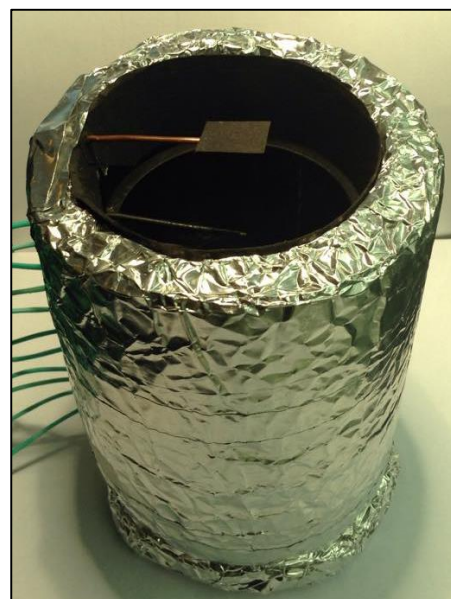
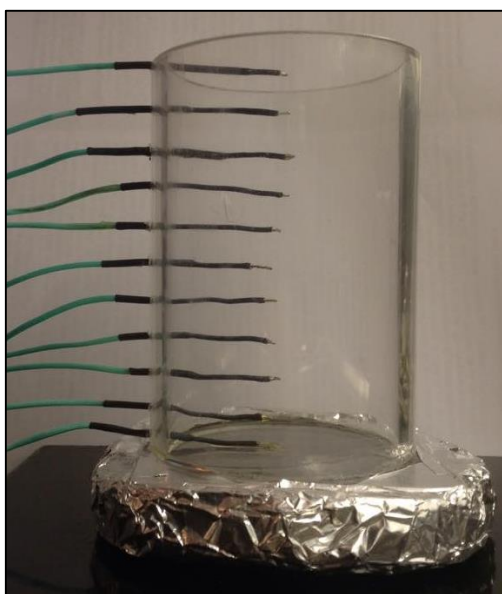


Figure 5.7 – Volumetric receiver

5.1.5. Solar simulator

In order to have more realistic results, the indoor solar simulator should have its light energy emitting spectrum as identical as possible to the solar spectrum. In the top of the Earth atmosphere, at mean Earth-Sun distance, the spectral distribution of the solar radiation closely matches a blackbody radiator with a temperature of about 5777 K, as shown in Figure 5.8.

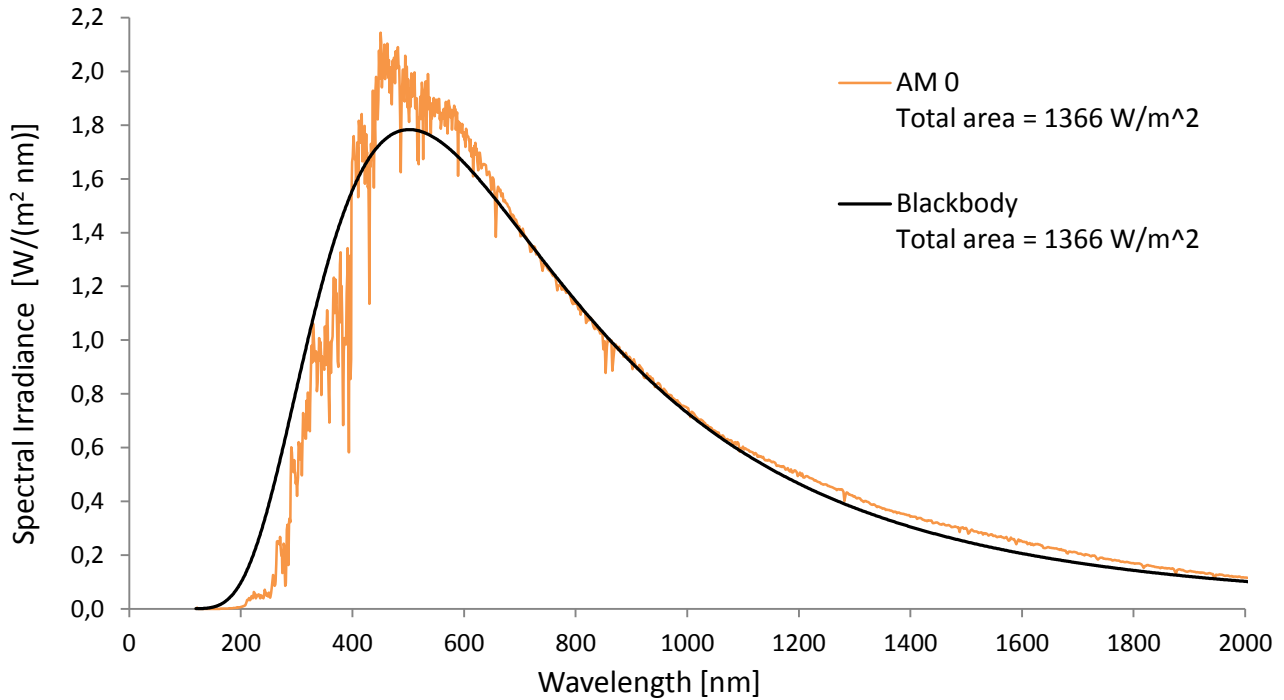


Figure 5.8 – Spectrum of the extraterrestrial solar radiation compared to the spectrum of a 5777 K blackbody

The spectrum curve of extraterrestrial solar radiation was based on a set of data included in the ASTM E-490 (AM0: Air Mass Zero, 2000) [40], while the curve that describes the blackbody radiation spectra was obtained from Plank's equation:

$$E_{b,\lambda} = \frac{C_1}{\lambda^5 (e^{C_2/\lambda T} - 1)} \quad (5.4)$$

where,

$E_{b,\lambda}$ = emissive power of a blackbody [W/(m² μm)]

T = temperature of the body [K]

λ = wavelength [μm]

$C_1 = 3,47 \times 10^8$ [W μm⁴/m²]

$C_2 = 1,44 \times 10^4$ [μm K]

In this case, $E_{b,\lambda}$ represents the spectral power radiated in all directions from the blackbody's surface, and not the spectral power from the Sun's surface that reaches Earth. So, the following equation was used to obtain the curve on Figure 5.8:

$$E_{\lambda} = E_{b,\lambda} \frac{r_s^2}{d_{s-e}^2} \quad (5.5)$$

where,

$r_s = \text{solar disk mean radius} = 695\,980 \text{ Km}$

$d_{s-e} = \text{mean Earth - Sun distance} = 149\,597\,890 \text{ Km}$

To calculate the emissive power over all wavelengths, E_{λ} needs to be integrated:

$$E_{total} = \int_{\lambda=0}^{\lambda=+\infty} E_{\lambda} d\lambda = \frac{r_s^2}{d_{s-e}^2} \int_{\lambda=0}^{\lambda=+\infty} \frac{C_1}{\lambda^5 (e^{C_2/\lambda T} - 1)} d\lambda = \frac{r_s^2}{d_{s-e}^2} \sigma T^4 \quad (5.6)$$

With this equation, we can easily obtain the equivalent total power per unit area that the Earth would receive if the Sun was considered to be a blackbody with a temperature of 5777 K.

$$E_{total} = \frac{695\,980^2}{149\,597\,890^2} \times 5,67 \times 10^{-8} \times 5777^4 \approx 1366 \text{ [W/m}^2\text{]} \quad (5.7)$$

However, as sunlight passes through the atmosphere, it is attenuated by scattering and absorption. Therefore, two standard solar spectral irradiance distributions for terrestrial use have been defined in the ASTM G173-03 (AM1.5, 1992) [30]. The air mass coefficient of 1.5 defines the direct optical path length through the Earth's atmosphere that corresponds to a solar zenith angle of 48,2 degrees. The AM1.5 Global Tilt spectrum is designed for flat plate modules and includes the spectral radiation from the solar disk, plus the sky diffuse radiation, and the diffuse reflected from the ground (30%), on a south facing surface tilted 37° from horizontal. The AM1.5 Direct spectrum is the reference defined for solar concentrating technologies and it includes the direct beam from the sun, plus the circumsolar component in a disk of 2,5° around the sun. The comparison of the spectral distribution of AM0, AM1.5 Global and AM1.5 Direct is shown in Figure 3.2.

The illumination source used in the experimental analysis was an ASD Pro-Lamp model [27] that corresponds to the same used for measuring transmissivity in section 2.3.1. In Figure 5.9 is presented the comparison between AM0, AM1.5 Direct and the solar simulator relative spectra in terms of percentage of the total AM0 spectral irradiance (1366 W/m²).

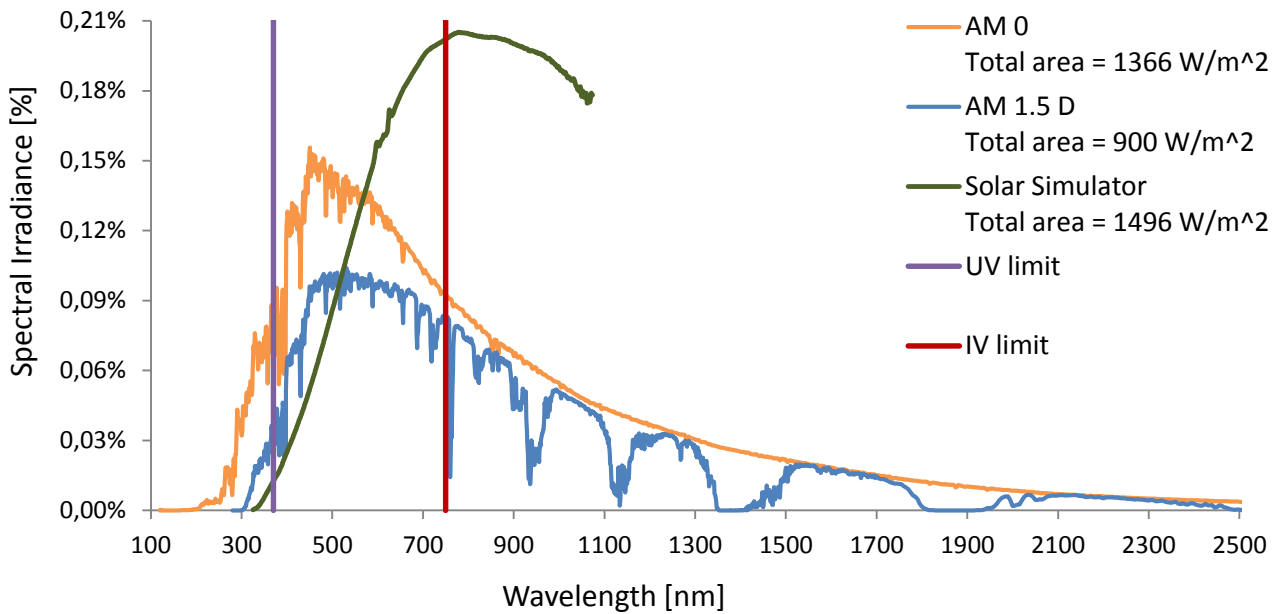


Figure 5.9 – Comparison between AM0, AM1.5 Direct and solar simulator spectral distribution

The trapezoidal integration method [31] was used to calculate the total area for any of the previous spectra. Note that, due to the power and distance of the solar simulator from the spectroradiometer, its absolute total irradiance value is bigger when compared to the sun's AM0 spectra (1496 W/m² > 1366 W/m²). A short arc discharge xenon lamp or metal halide high intensity discharge lamp is preferable as its spectrum matches more closely the solar spectrum.

In practice, a solar simulator should have other components besides the lamp, as described in appendix VI. However, an assessment on its performance was still carried out. To quantify and qualify the resemblance between a solar simulator and the sun's spectra, a standard has been defined [41]. Its purpose is to attribute classifications (A, B or C) of indoor measurements for solar simulators in three categories: spectral distribution match, irradiance non-uniformity on the test plane and temporal instability.

• **Spectral distribution match**

The spectral match of a solar simulator is defined by the deviation from AM1.5 Global reference spectral irradiance [30] on 6 wavelength intervals. The classification for each interval is done according to Table 5.1.

Table 5.1 – Classification criteria for spectral match

Classification	Spectral match to all intervals
A	0,75 - 1,25
B	0,6 - 1,4
C	0,4 - 2,0

The first step to obtain the spectral match is to integrate the spectral irradiance measured in the range of 400 nm to 1 100 nm. Then the percentage contribution (ratio between spectral irradiance and integrated value) of each wavelength interval should be calculated. Finally, the percentage on each wavelength interval divided by the percentage of the correspondent interval on the AM1.5 Global will result on the spectral match. The obtained classifications are presented in Table 5.2.

Table 5.2 – Spectral match classification for the solar simulator

Interval	Wavelength [nm]	Percentage of total irradiance of AM1.5 Global	Spectral match of Solar Simulator	Classification
1	400 – 500	18,4 %	0,263	C
2	500 – 600	19,9 %	0,557	C
3	600 – 700	18,4 %	0,883	A
4	700 - 800	14,9 %	1,242	A
5	800 - 900	12,5 %	1,496	C
6	900 - 1100	15,9 %	1,931	C

• **Non-uniformity irradiance on the test plane**

According to the solar simulator performance requirements [41], non-uniformity of irradiance should be tested by dividing the designated test area into at least 64 equally sized blocks. However, due to the small area at stake, approximately 38,48 cm², this measurement was not carried out, and it was assumed total uniformity of irradiance, which corresponds to an A classification.

• **Temporal instability of irradiance**

Temporal instability of irradiance is defined by the following equation:

$$Temporal\ instability\ (\%) = \left[\frac{max\ irradiance - min\ irradiance}{max\ irradiance + min\ irradiance} \right] \times 100\% \quad (5.8)$$

For a short term period of 1 second and a long term period of 5 hours, the obtained maximum and minimum irradiances are presented in Table 5.3.

Table 5.3 – Results for temporal instability of irradiance

	Short term instability (STI)	Long term instability (LTI)
Maximum irradiance [W/m^2]	1600	1601,52
Minimum irradiance [W/m^2]	1600	1597,36
Temporal instability [%]	0	0,13

Since short term and long term instabilities are, respectively, below 0,5% and 2%, a classification of A is obtained for the solar simulator temporal instability

Table 5.4 – Classification criteria for irradiance temporal instability

Classification	Temporal instability	
	Short term instability (STI)	Long term instability (LTI)
A	0,5%	2%
B	2%	5%
C	10%	10%

• **Overall classification of the Solar Simulator**

The classification concerning each of the three categories previously analyzed is attributed by one of these three classes: A (best), B, and C (worst). For the spectral match category, the ranking is determined by the worst classification registered in all 6 wavelength intervals. As for the solar simulator, its rate is defined by three letters in order of spectral match, non-uniformity of irradiance in the test plane and temporal instability. In this case, the solar simulator overall classification obtained was CAA.

5.2. Nanofluid

In this work, four different nanofluids were prepared and studied in order to analyze their impacts on solar radiation collection. To what concerns the solid suspension, two carbon based particles were used: graphite-based and carbon nanotube-based (multi-walled). Regarding the base fluids, pure water and a thermal oil were used.

5.2.1. Nanofluid properties

Water is a widely available fluid, and as proven before, it has physical properties that are suitable enough for low temperature nanofluidic applications on solar thermal energy conversion. On the other hand, thermal oils allow much higher temperatures to be reached, however, there are also some environmental concerns that have to be taken into account. Perfecto HT 5 is a heat transfer oil based upon highly refined mineral oil, selected for its high thermal stability, resistance to oxidation and low volatility [19]. In Figure 5.13 it is possible to visually notice the colour difference between these two fluids (A and B), which is caused by the different spectral absorption of light. In Figure 2.3 a comparison is made on the fluids transmissivity in the visible and near infrared wavelength range. Pure water presents an almost constant transmissivity of 100% in the visible wavelengths, while the thermal oil transmits less than 50% before 400 nm, according to the measurement procedure described in section 2.3.1. Note that only after the 950 nm does the thermal oil absorb less radiation than pure water.

When comparing the structure of the two carbon solid particles, the difference lies in their arrangement. Graphite has spherical shaped nanoparticles in opposite to a multi-walled carbon nanotube arrangement, as shown in Figure 5.10.

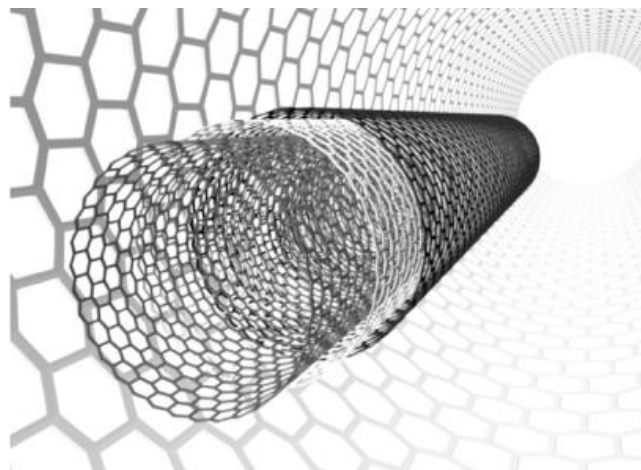


Figure 5.10 – MWCNT structure [42]

The particle size diameter can have some impact on the nanofluid performance [3] however, in the present experimental study, this influence was not investigated. The used graphite spheres have a particle size diameter below 37 micrometers, while the MWCNT present nominal diameters from 10 to 30 nm and nominal lengths from 5 to 20 μm . Purity level was assured by the manufacturer to be higher than 85 weight percent [43]. Although producing MWCNT is a more complex process compared to graphite nanoparticles, their properties suggest a higher potential for the purposes of nanofluids used in volumetric receivers, and therefore, promise a better performance.

Immediately after the nanofluid preparation, the spectral transmissivity of the dispersion was studied. Results are presented in Figure 5.11, in which the fluid used as white reference corresponds to the base fluid in which nanoparticles are suspended in. From a comparison considering the same base fluid, MWCNTs revealed to achieve lower transmissivities, while simultaneously presenting a lower volume fraction. This may suggest a better performance by these particular nanoparticles. Some oscillations are perceptible near the 400 and 1000 nm that result from the spectroradiometer limitations.

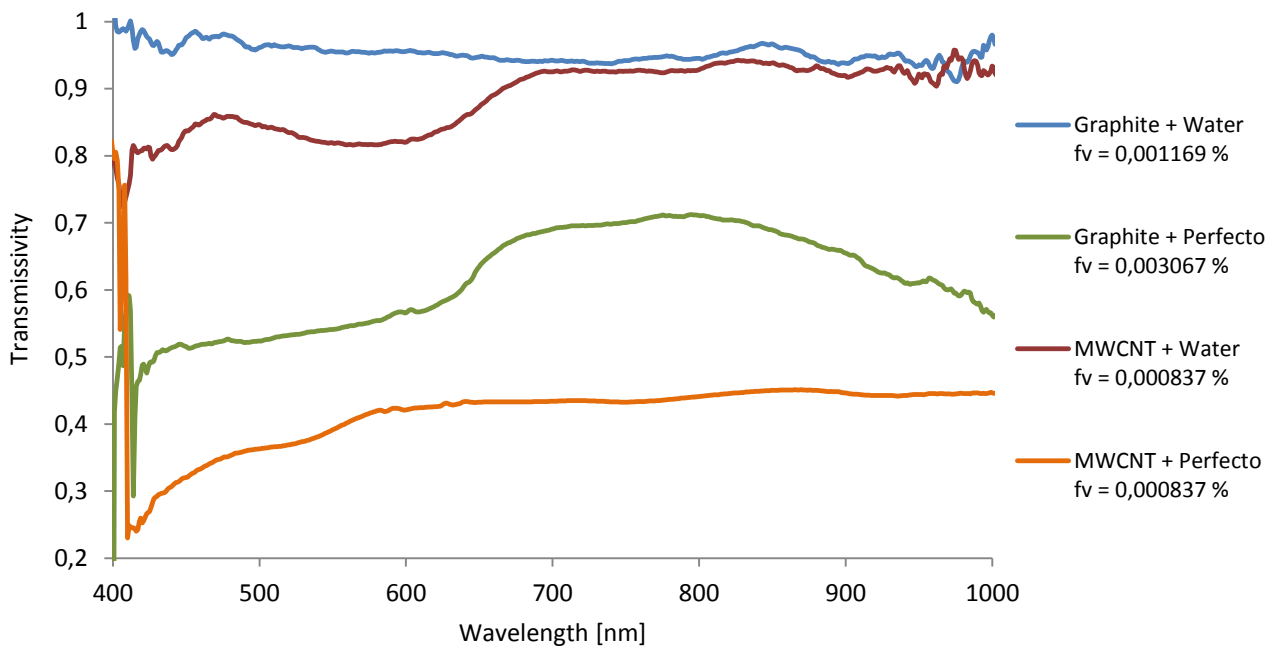


Figure 5.11 – Transmissivity of the different nanofluids

5.2.2. Nanofluid preparation

Both graphite nanoparticles and MWCNT suspended on a base fluid were prepared through a two-step process. That is, the solid nanoparticles were first mixed with the base fluid using the desired volume fraction, in which the mass was measured using a precision balance with a resolution of 0,00001 g. Then, the dispersion was subjected to a sonication bath during 2 hours, which was found to be an acceptable time considering that no stabilizers or surfactants were added to the suspensions. The sonicating bath consists in immersing the fluid into a water tank that is under the vibrating effect caused by ultrasound frequency. Figure 5.12 shows the preparation of a nanofluid using a Branson 2510 [44] type sonicator with an ultrasound frequency of 40 kHz.



Figure 5.12 – Sonicating bath

Note that during the sonication bath, the nanoparticle dispersion significantly raises its temperature. For this reason, the fluid should be allowed to cool down before temperature measurements are taken.

Figure 5.13 shows representative samples of the base fluids and nanofluids prepared. Once the density of the solid particles is higher than the density of the base fluids used, it was expected that the nanoparticles would settle towards the bottom of the container after several hours of rest. Accordingly, nanoparticles started to show a visible sedimentation after 12 hours of preparation.

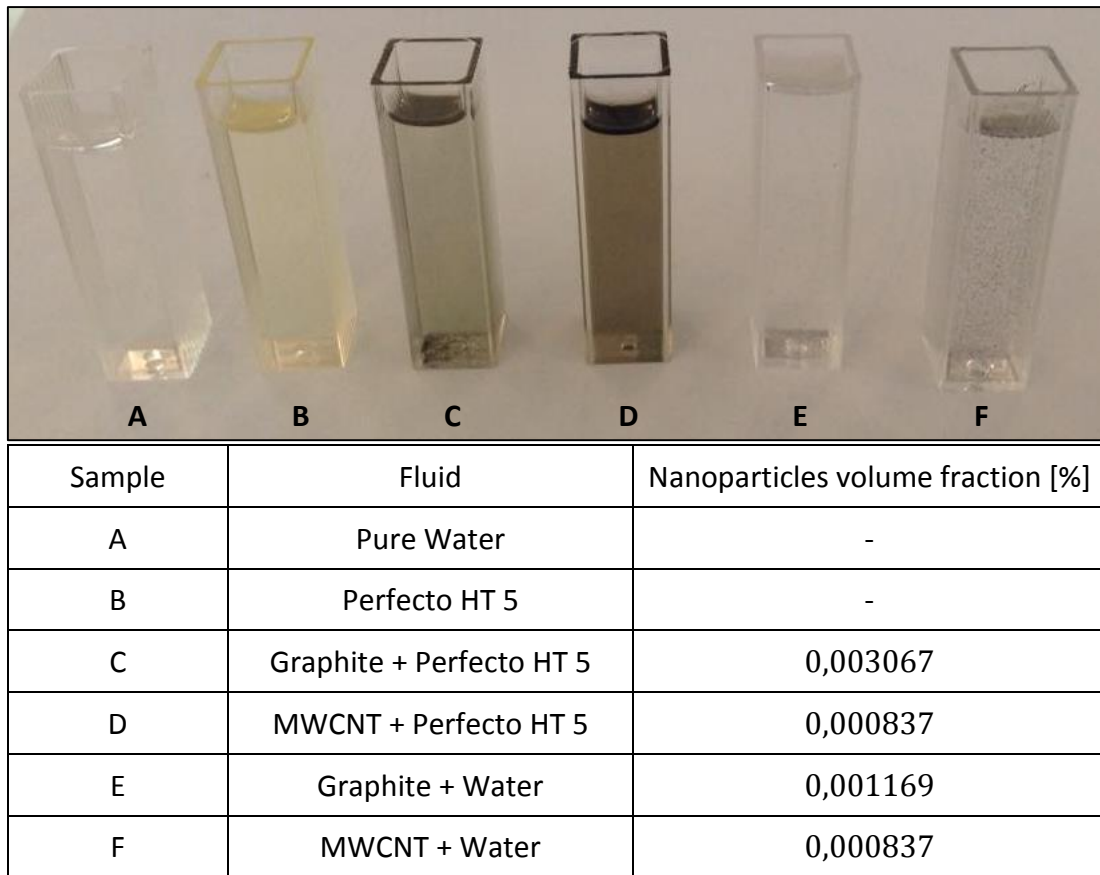


Figure 5.13 – Fluid samples used in the experimental apparatus

5.3. Results and experimental validation

The experimental analysis on the nanofluid performance was developed according to the experimental apparatus as shown in Figure 5.14.

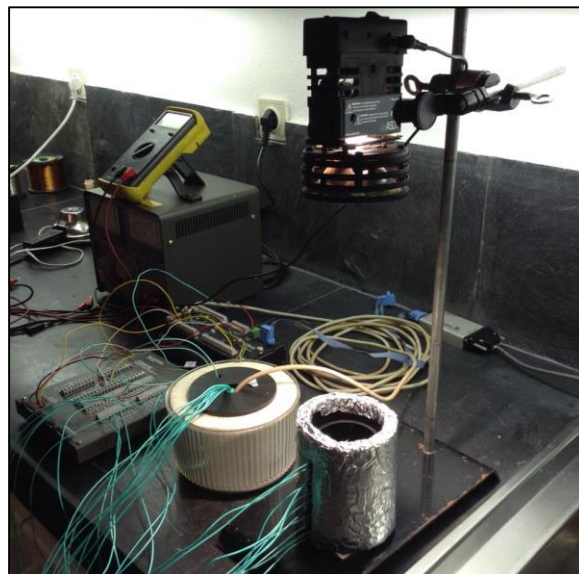


Figure 5.14 – Experimental setup

Although not illustrated, four metal boards were attached to the structure so that the receiver is only illuminated by the stabilized direct light from the solar simulator, and not by diffuse light from other light sources. Measurements were made under indoor conditions, however, not under a controlled environment, which means that the heat loss magnitude and initial fluid temperatures may change due to ambient temperature fluctuations.

According to the nanofluid height and spectrum of the solar simulator, the experiment was performed using an optimized volume fraction of nanoparticles. After 5 hours of collecting data, the experimental results were compared with the numerical model outputs. To try to keep this comparison as balanced as possible, the measured values of ambient temperature and average initial temperature of the nanofluid were set as inputs on the numerical model. The remaining inputs of wind speed and glass emissivity were set respectively equal to 0,01 m/s and 0,95. The thermodynamic properties of the nanofluid were determined for a constant temperature of 25°C, as described in Chapter 2. To what concerns the radiation input for the numerical model, no fluctuations over time were considered and radiation was assumed to be collimated. Note that the simulation was made for a wavelength range from 280 nm to 2500 nm. However, due to the spectral range limitation of the spectroradiometer, the spectrum of the solar simulator was approximated to a blackbody with a temperature of 3550 K. Figure 5.15 presents the two spectra in terms of percentage of AM0 distribution spectrum.

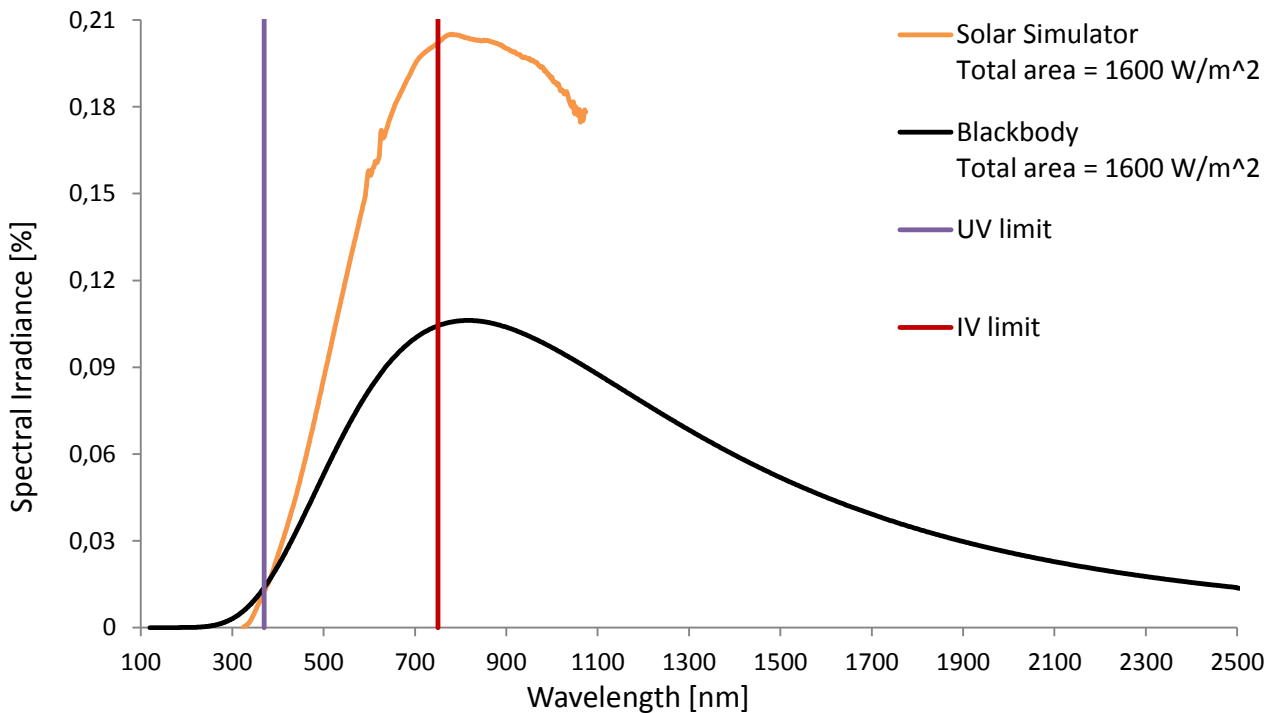


Figure 5.15 – Spectrum of the lamp for solar simulator in the experimental setup

Four different nanofluids were tested, however, the results obtained in the case of graphite nanoparticles suspended in thermal oil were not satisfactory. Also, due to a major particle agglomeration when dispersing MWCNT in water, the results were not as expected, therefore, this case was not considered valid for this study too. When testing the remaining nanofluids, the main discrepancy between the numerical model and the experimental results is evident in the lower stagnation temperatures and efficiencies. However, this is not surprising once adiabatic walls were considered in the numerical model. Additionally, during transient regime some energy is accumulated in the walls of the experimental apparatus, thus affecting the temperature profile, which phenomena was not included in the 1-D numerical model. Also, errors associated to the measurement of the mass of nanoparticles and incident radiation may have also altered the performance of the receiver. To what concerns the comparison of the temperature profile in transient regime, the experimental results demonstrate a similar behaviour as the numerical model. For the two cases of graphite suspended in water, and MWCNT suspended in Perfecto HT 5, such comparison is presented, respectively, in Figure 5.16 and Figure 5.17, in which the horizontal axis was adimensionalized as follows:

$$\theta = \frac{(T - T_{initial})}{(T_{max} - T_{initial})} \quad (5.9)$$

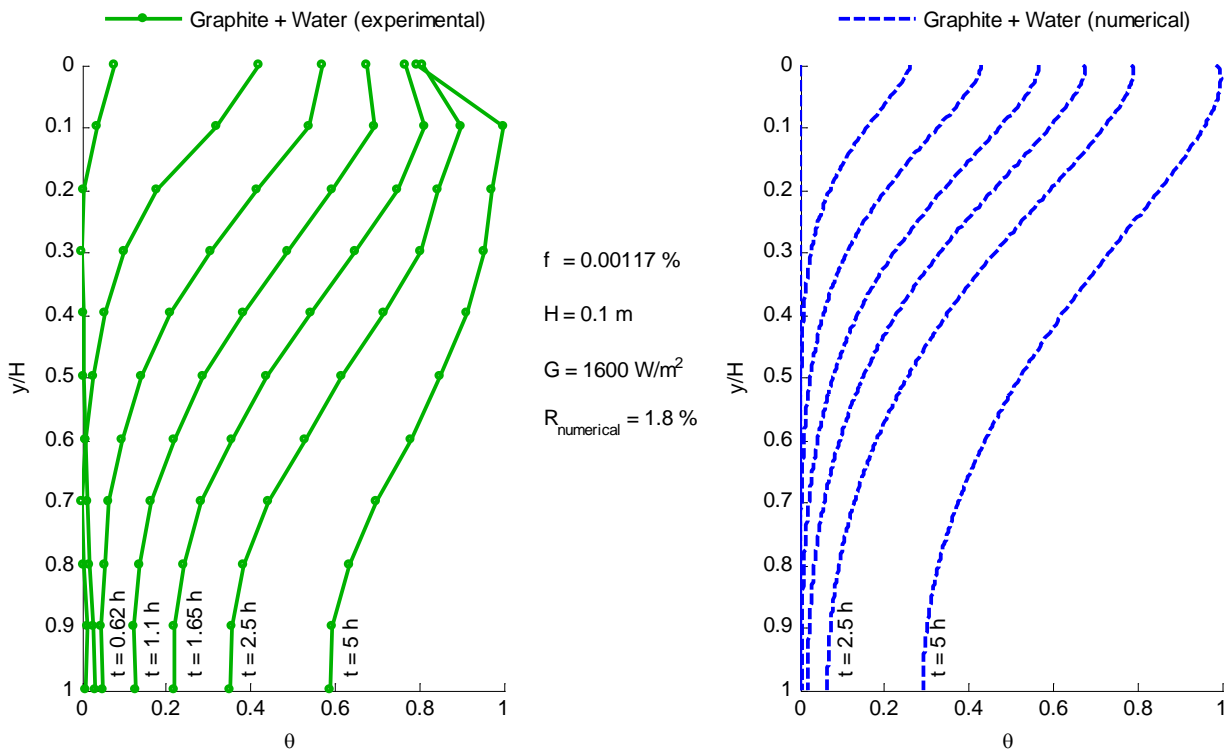


Figure 5.16 – Comparison of experimental and numerical results for graphite + water nanofluid

For both nanofluids, the reasonable agreement between the numerical model and the experimental results suggests that the developed model can be used to investigate the solar harvesting mechanisms featured by nanofluids.

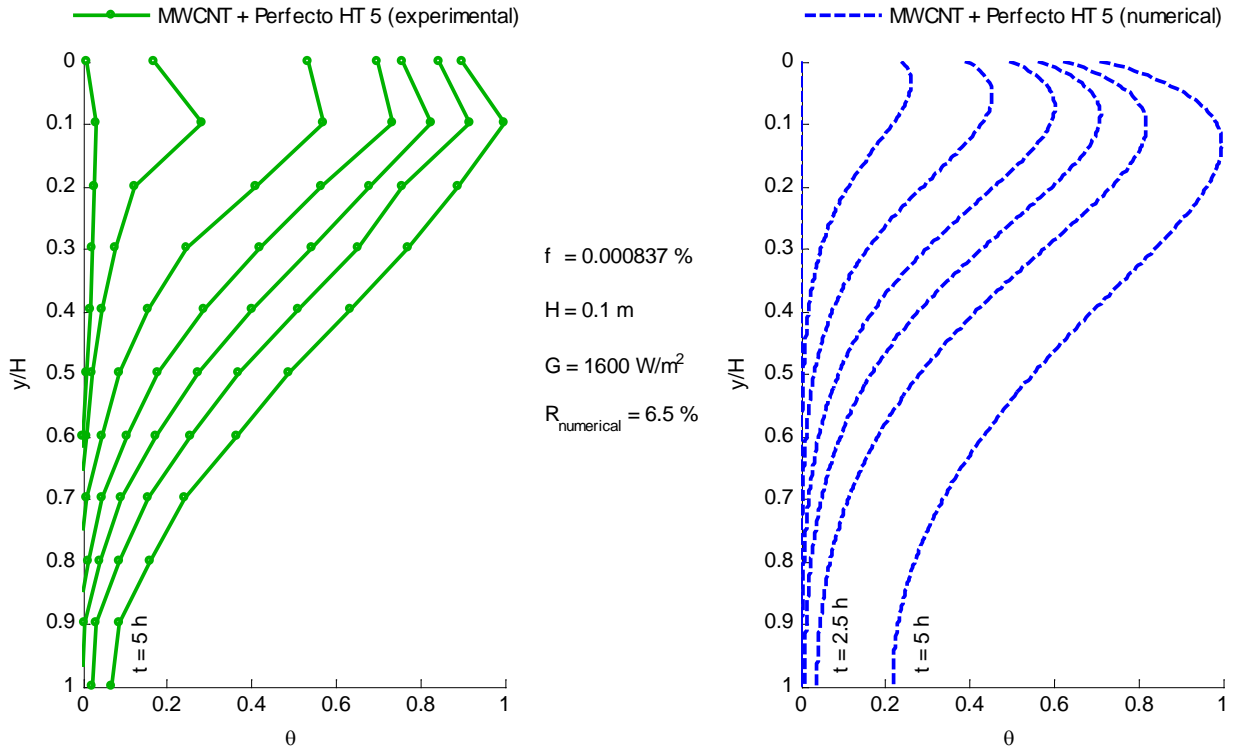


Figure 5.17 – Comparison of experimental and numerical results for MWCNT + Perfecto HT 5 nanofluid

6. MODELLING OF A VOLUMETRIC FLOW RECEIVER

The aim of this study was to evaluate the impact of nanofluids on a volumetric flow receiver. A two-dimensional model was created according to the schematic of Figure 6.1. The fluid enters the parallel plate configuration, of length L and height H , with a uniform temperature T_{in} and leaves the receiver with a mean temperature T_{out} . The radiative heat flux G is transmitted through a transparent cover and absorbed volumetrically by the nanofluid. The energy absorbed results in a volumetric heat release. The convective and radiative heat losses are only considered in the top surface of the receiver.

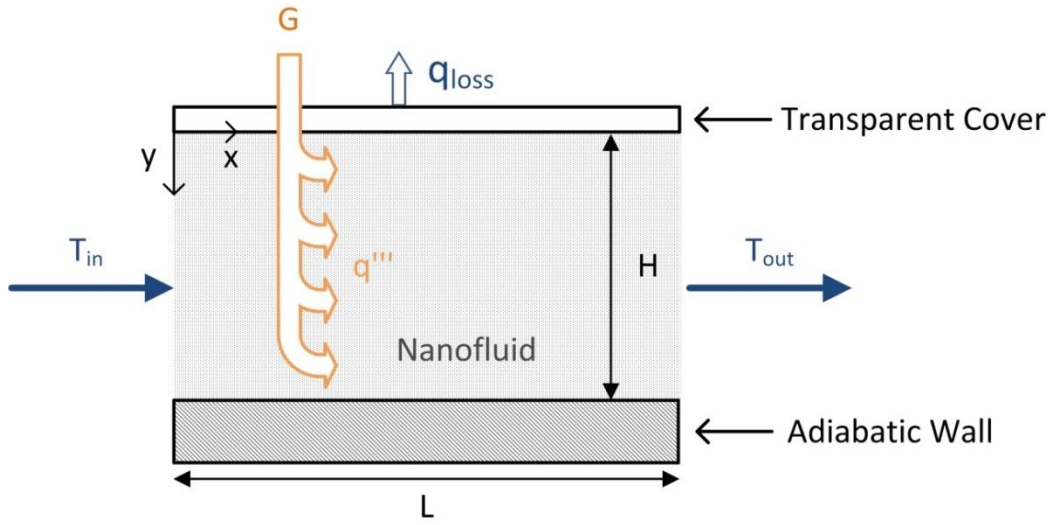


Figure 6.1 – Schematic for model formulation of a nanofluid-based solar receiver

6.1. Temperature profile

The energy equation for an infinitesimal element inside a homogenous and isotropic nanofluid is:

$$\rho c_p \left(\frac{\partial T}{\partial t} + v_x \frac{\partial T}{\partial x} + v_y \frac{\partial T}{\partial y} + v_z \frac{\partial T}{\partial z} \right) = k \left(\frac{\partial^2 T}{\partial x^2} + \frac{\partial^2 T}{\partial y^2} + \frac{\partial^2 T}{\partial z^2} \right) + q''' \quad (6.1)$$

Assuming that the flow is hydrodynamically fully developed, and that the variation of thermal conductivity with temperature and the heat diffusion on x and z directions are negligible, then:

$$v_y = v_z = 0$$

$$k \frac{\partial^2 T}{\partial x^2} = k \frac{\partial^2 T}{\partial z^2} = 0$$

Eq. (6.1) is simplified and we obtain:

$$\rho c_p \left(\frac{\partial T}{\partial t} + v_x \frac{\partial T}{\partial x} \right) = k \frac{\partial^2 T}{\partial y^2} + q''' \quad (6.2)$$

Rearranging Eq. (6.2) in order to get an expression to determine the temperature variation over time, we obtain:

$$\frac{\partial T}{\partial t} = \alpha \frac{\partial^2 T}{\partial y^2} - v_x \frac{\partial T}{\partial x} + \frac{q'''}{\rho c_p} \quad (6.3)$$

where α is the thermal diffusivity of the nanofluid given by Eq. (2.5).

This equation can be put in a dimensionless form by substituting its correspondent variables by:

$$\begin{aligned} T^* &= \frac{T}{T_{in}} & v_x^* &= \frac{v}{v_{mean}} \\ y^* &= \frac{y}{H} & t^* &= \frac{v_{mean}}{H} t \\ x^* &= \frac{x}{H} & q''''^* &= \frac{q''' H}{\rho c_p v_{mean} T_{in}} \end{aligned}$$

Resulting in:

$$\frac{\partial T^*}{\partial t^*} = \frac{2}{Pe} \frac{\partial^2 T^*}{\partial y^{*2}} - v_x^* \frac{\partial T^*}{\partial x^*} + q''''^* \quad (6.4)$$

in which $Pe = Re Pr$ is the Péclet number. Solving this equation for a grid of points inside the receiver volume, we can determine the evolution over time of the temperature profile on x and y directions.

6.2. Numerical model

The discretization of the two-dimensional domain between parallel plates was carried out according to a rectangular mesh (101x101 points), as shown in Figure 6.2. Once the temperature gradient is less accentuated on x direction, a lot of computation time can be saved by increasing the horizontal step size distance.

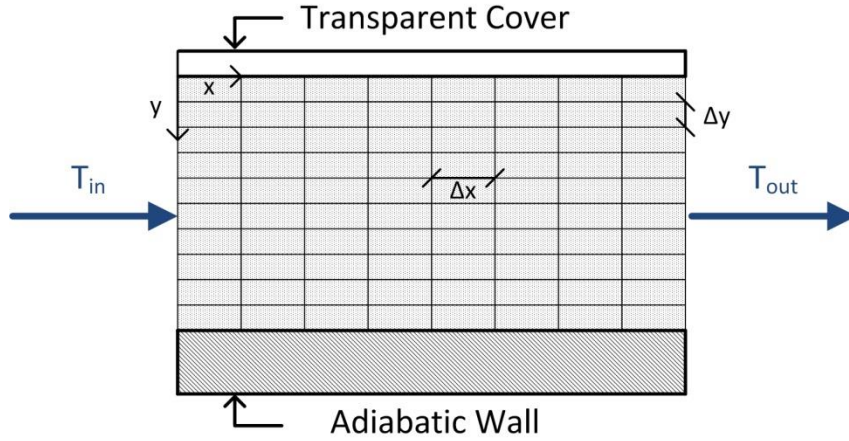


Figure 6.2 – Bi-dimensional mesh for receiver domain discretization

A fully developed laminar flow was assumed throughout the length of the receiver. Given the schematic shown in Figure 6.3, the parabolic velocity profile between parallel plates was determined using the following expression [32]:

$$v(y) = \frac{3}{2} v_{mean} \left[1 - \left(\frac{y}{H/2} \right)^2 \right] \quad (6.5)$$

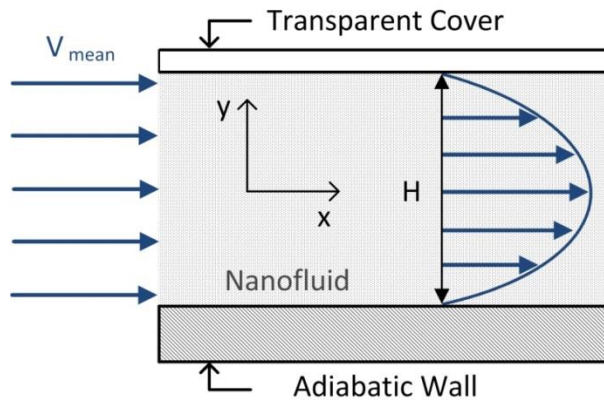


Figure 6.3 – Velocity profile between parallel plates

To guarantee that a laminar flow was kept, Reynolds number was maintained below 2300 and the mean velocity was obtained from Eq. (6.6):

$$Re = \frac{\rho v_{mean} D_h}{\mu} \quad (6.6)$$

In which the hydraulic diameter D_h equals twice the distance between the parallel plates. The density and dynamic viscosity of a nanofluid were determined as described in Chapter 2.

To obtain the temperatures in each point of the two-dimensional model, MacCormack’s technique [45] was implemented in *Matlab* according to the flowchart shown below. The inputs concern the environmental conditions, receiver geometry, time and space discretization, nanofluid properties, and flow parameters. The initial values are necessary for the numerical simulation to start, in which temperature values are assumed on both internal and boundary points.

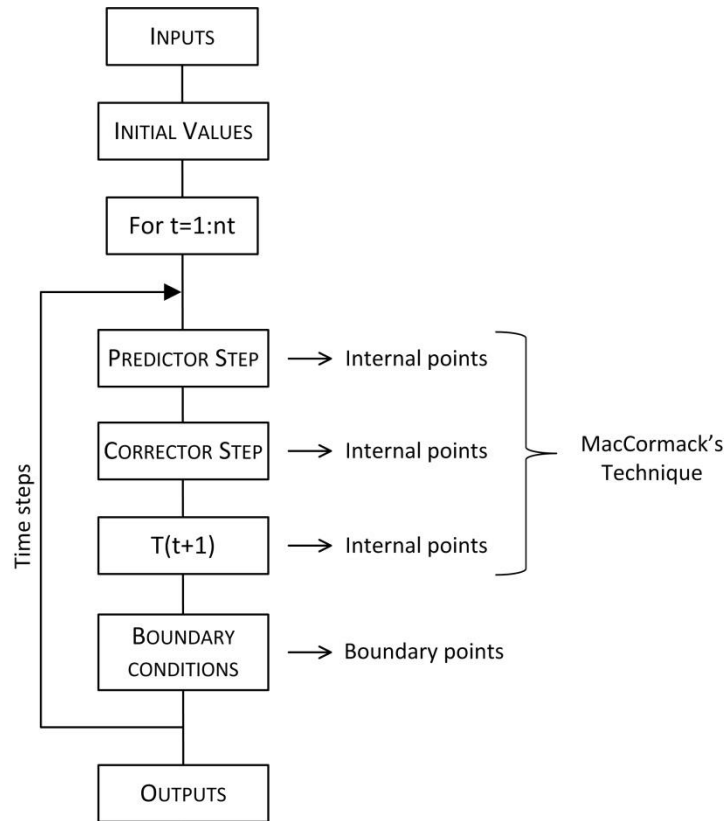


Figure 6.4 – Flowchart of the numerical model formulation

6.2.1. Internal points

MacCormack’s technique is an explicit finite difference method that allows the determination of the flow variables at the time $t + \Delta t$ on each grid point, assuming that these variables are known at the time t [45]. This technique works on the basis of a prediction step, a correction step, and finally, the determination of the average value of the time derivative, and calculation of the dependent variables. In this work we intend to determine the temperature on each grid point in transient regime. Let’s recall the energy balance equation, Eq. (6.3):

$$\frac{\partial T}{\partial t} = \alpha \frac{\partial^2 T}{\partial y^2} - v_x \frac{\partial T}{\partial x} + \frac{q'''}{\rho c_p}$$

In the predictor step, the spatial derivatives of Eq. (6.3) should be approximated by forward finite differences, resulting in $\left(\frac{\partial T}{\partial t}\right)_{i,j}^t$. Then, the prediction of the temperature at $t + \Delta t$ is obtained as follows:

$$(\tilde{T})_{i,j}^{t+\Delta t} = T_{i,j}^t + \left(\frac{\partial T}{\partial t}\right)_{i,j}^t \Delta t \quad (6.7)$$

in which Δt is the time step.

In the corrector step, the spatial derivatives of Eq. (6.3) should be approximated by rearward finite differences, however, using the values of the predicted temperature $(\tilde{T})_{i,j}^{t+\Delta t}$ from Eq. (6.7), resulting in $\left(\frac{\partial \tilde{T}}{\partial t}\right)_{i,j}^{t+\Delta t}$. The average value of the time derivative is obtained by calculating the arithmetic mean of forward and rearward derivatives:

$$\left(\frac{\partial T}{\partial t}\right)_{av} = \frac{1}{2} \left[\left(\frac{\partial T}{\partial t}\right)_{i,j}^t + \left(\frac{\partial \tilde{T}}{\partial t}\right)_{i,j}^{t+\Delta t} \right] \quad (6.8)$$

Finally, the temperature value at the time $t + \Delta t$ is determined using the following equation:

$$T_{i,j}^{t+\Delta t} = T_{i,j}^t + \left(\frac{\partial T}{\partial t}\right)_{av} \Delta t \quad (6.9)$$

6.2.2. Boundary points

To be able to implement the method, several additional constraints were imposed. These constraints were set at the boundary of the bi-dimensional mesh, as illustrated in Figure 6.5. Two possible situations can occur on each boundary: constant temperature or constant heat flux (q'').

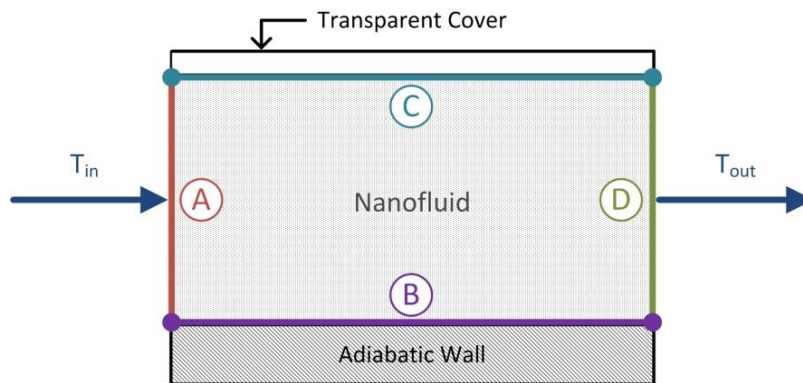


Figure 6.5 – Boundary conditions schematic

Which, in dimensionless form, reads as:

$$\begin{aligned}
 A \rightarrow T^*|_{x=0} &= 1 & C \rightarrow q''_{y=0} &= -k \frac{T_{in}}{H} \frac{\partial T^*}{\partial y^*} \\
 B \rightarrow q''_{y=H} &= 0 & D \rightarrow q''_{x=L} &= 0
 \end{aligned}$$

where $q''_{y=0}$ depends on the heat loss in the top surface, in a similar way as described in Chapter 3 as for example in Eq. (3.17).

6.3. Receiver efficiency

The collector efficiency can be evaluated by determining the ratio between the sensible heat gain of the nanofluid and the total solar radiation incident on the top surface of the receiver:

$$\eta = \frac{\sum_{j=1}^{j=nj} \dot{m} c_p (T_{i=L;j} - \bar{T}_{in})}{C G A} = \frac{\sum_{j=1}^{j=nj} v_j \rho dy c_p (T_{i=L;j} - \bar{T}_{in})}{C G L} \quad (6.10)$$

where $T_{i=L;j}$ represents the temperature on each point at the end of the receiver, and \bar{T}_{in} represents the mean inlet temperature. This corresponds to assume a uniform temperature and velocity in a height dy centered in each grid point at the exit boundary surface.

6.4. Numerical results

The eight nanofluids compared in the previous chapters will be investigated, but now under flowing regime between parallel plates. The same environmental conditions, incident spectral radiation, properties of the nanofluids, and optimized volume fractions were also maintained for a 1 cm height receiver. On this analysis, it was established that the length of the receiver was fixed at 1 meter, and the mean inlet velocity was adjusted between 0,01 and 0,1 m/s with a constant inlet temperature of 25°C. From the simulation results over 240 seconds, it was verified that the temperature profile obtained for the same mean velocity is very similar among each nanofluid. Thus, as an example, a temperature profile in transient regime is shown in Figure 6.6 for a volumetric receiver under a constant flow with a mean velocity of 0,01 m/s and a solar concentration factor of 14. As expected, the temperature increase near the top surface is visible. Examining the temperatures close to the inlet border, these present the same values after 20 seconds exposed to solar radiation. This

happens because the nanofluid cannot collect more energy during the period of time it has to go through the 1 cm length. However, at the outlet border of the receiver, the temperature increases over time with a maximum value near the top.

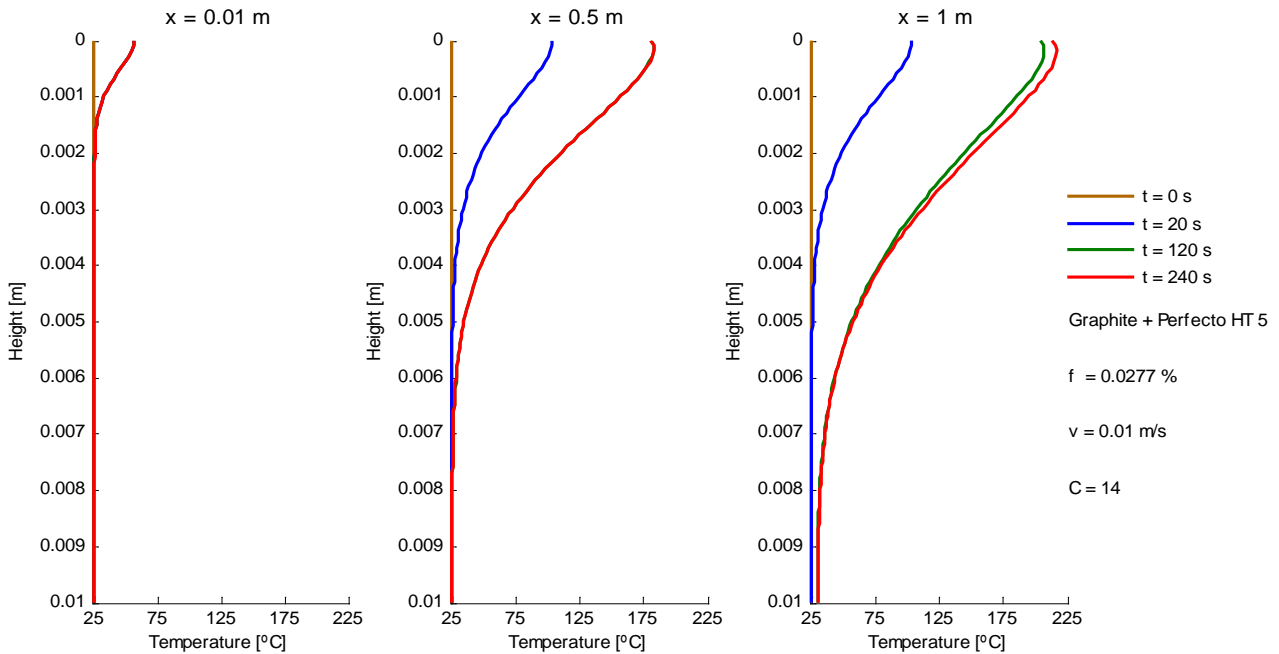


Figure 6.6 – Temperature profile in transient regime at different points of the receiver length

From these results, we can now determine the mean outlet temperature of a nanofluid in transient regime and study the impact of the solar concentration factor. For the same nanofluid and conditions as before, the solar concentration factor was varied between 1 and 14, where outputs are shown in Figure 6.7.

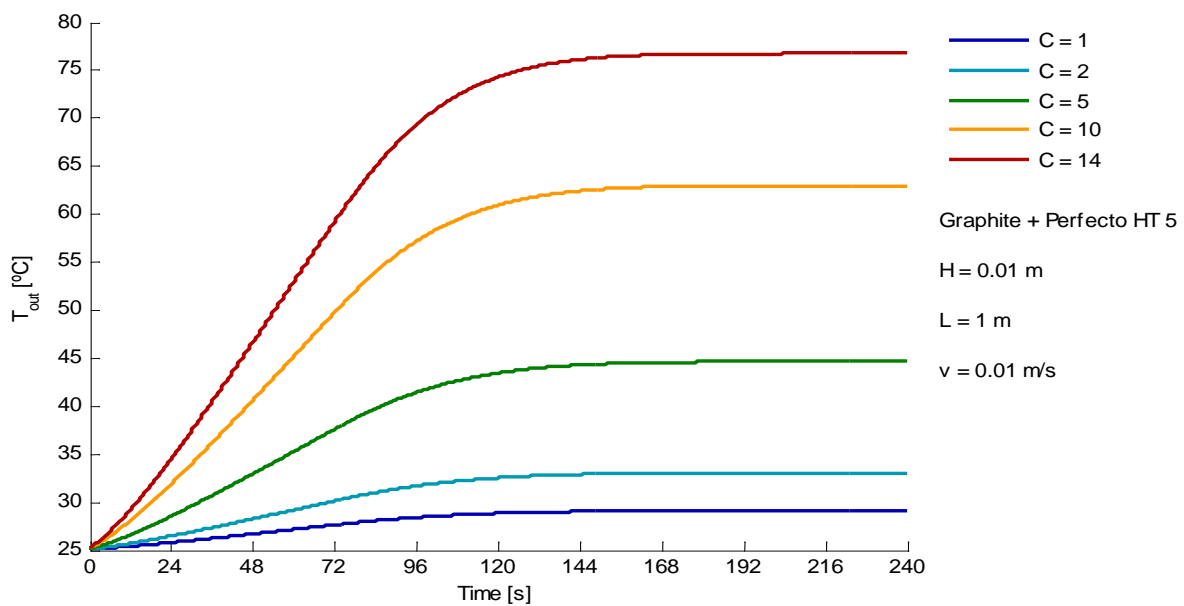


Figure 6.7 – Mean outlet temperature under different solar concentration factors

The same analysis was applied to the different nanofluids and the results show that the increase of the solar concentration factor will cause an increase on the outlet temperature. However, this increase is not linear.

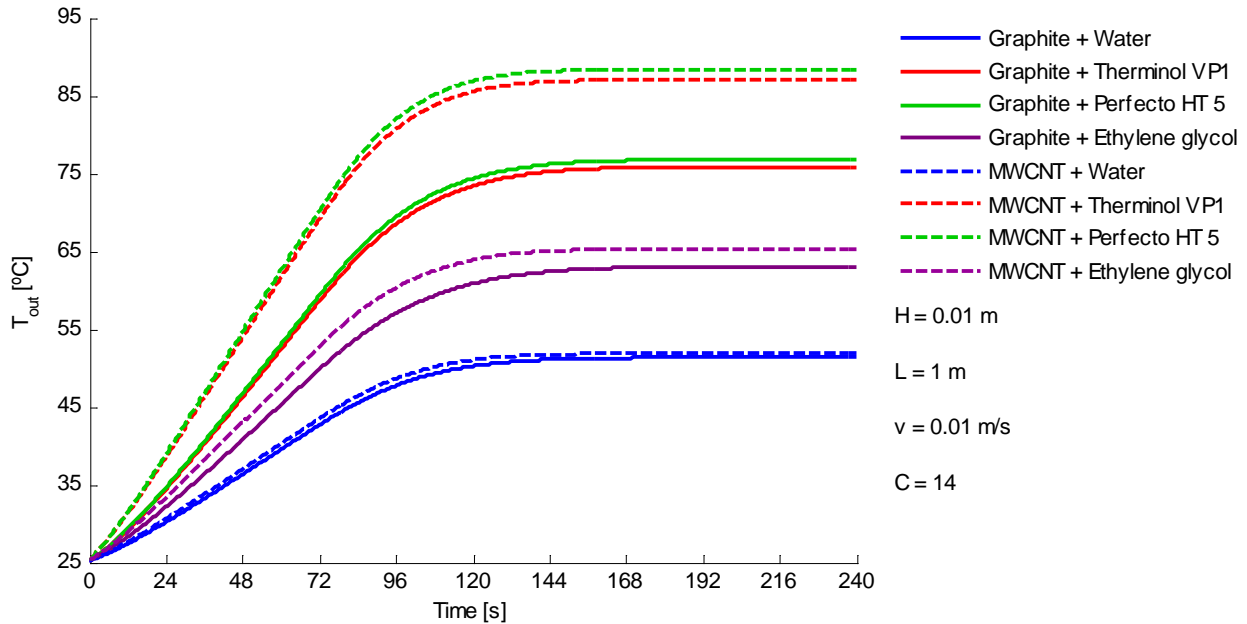


Figure 6.8 – Mean outlet temperature for different nanofluids

In Figure 6.8 it is evident that MWCNT suspended in Perfecto HT 5 reaches the higher temperatures under the same period of time, solar concentration factor and velocity. Furthermore, multiple simulations on this matter were carried out and results also show that this particular nanofluid has the highest temperatures for all the different solar concentration factors tested. The nanofluids with MWCNT solid particles also present a better performance compared to graphite solid particles with the same base fluid.

The efficiency of the volumetric receiver was determined according to the nanofluid used. In Figure 6.9 it is shown that a particular base fluid containing solid particles of MWCNT also has a better performance due to the higher efficiency values, when compared to graphite nanoparticles with the same base fluid. Efficiencies higher than 85% were obtained for water-based nanofluids. In addition, if graphite particles are considered, the base fluid that presents higher temperatures is the one with lower efficiency. This is due to the different thermodynamic properties of nanofluids, in particular the density and specific heat capacity for the optimal volume fraction of particles. The same argument is valid for a MWCNT-based nanofluid. An efficiency improvement of approximately 15% can be achieved by using MWCNT instead of graphite nanoparticles on thermal oils.

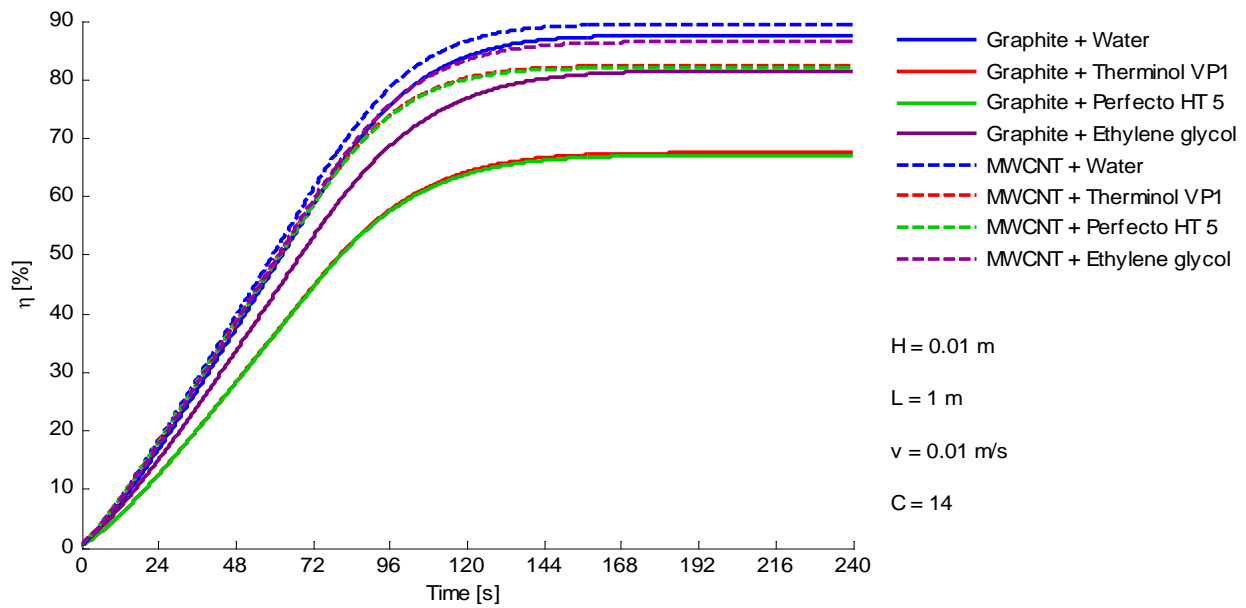


Figure 6.9 – Efficiency of the volumetric flow receiver for different nanofluids

The effect of the solar concentration factor on the efficiency of the receiver was also investigated. As expected, results demonstrate that the efficiency decreases when the solar concentration factor increases. This is caused by higher thermal losses to the environment. However, when increasing the solar concentration factor from 1 to 14, the impact on the efficiency decrease is less than 6% in all the nanofluids tested. This can be interpreted as a great advantage that is only possible due to the volumetrical absorption by the nanofluid. Note that, as seen in Figure 6.7, the temperature significantly increases with higher concentration factors, therefore energy collected is also increased with only 6% loss of efficiency. Special care should be paid when comparing the performance of two different nanofluids. For example, MWCNT and Perfecto HT 5 present both higher outlet temperatures and efficiency when compared to graphite suspended on ethylene glycol. On the other hand, the first nanofluid has lower efficiency when compared to graphite suspended on water. The physical properties of each nanofluid should also be at stake.

The previous analysis was carried out using a fixed value of velocity. To demonstrate its impact on the temperature of a volumetric receiver, Figure 6.10 plots the variation of the mean outlet temperature. Multiple simulations were carried out for each different mean velocity during a time period of 240 seconds. Results demonstrate that the mean outlet temperature decreases as velocity is increased. This behaviour was expected since the time during which nanoparticles are exposed to the solar radiation was reduced when velocity increased. In addition, for higher values of solar concentration factor, the temperature decrease is much more significant. These results were also verified in the case of the other nanofluids under study.

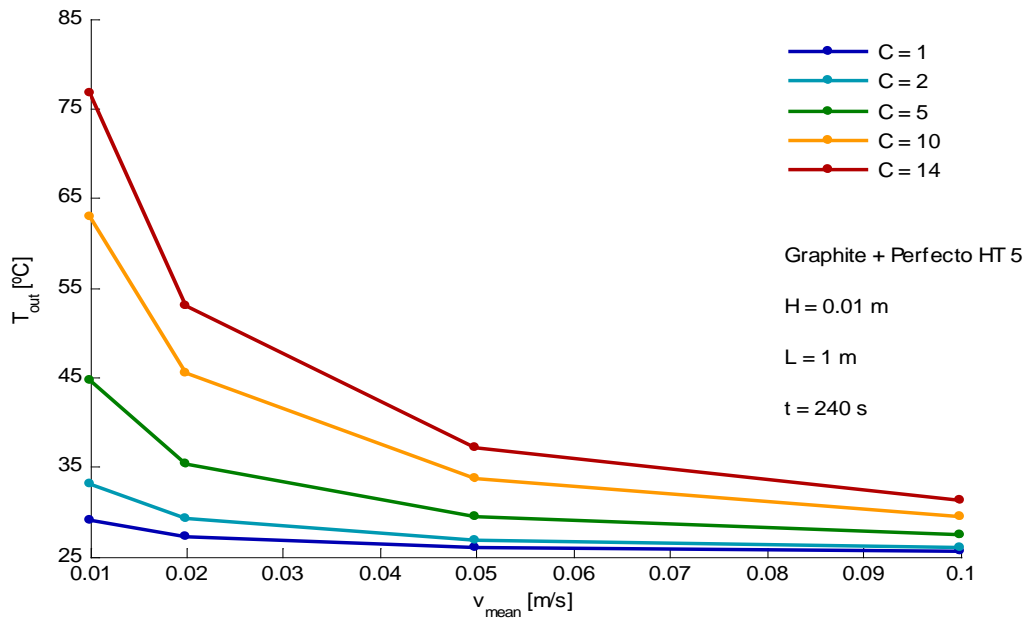


Figure 6.10 – Velocity impact on the receiver outlet temperature for different solar concentration factors

A study was also carried out in order to investigate how the outlet temperature as well as the efficiency of the receiver are influenced by the inlet temperature. In Figure 6.11 it is shown that the variation of the outlet temperature (slope) is basically the same for all the nanofluids studied.

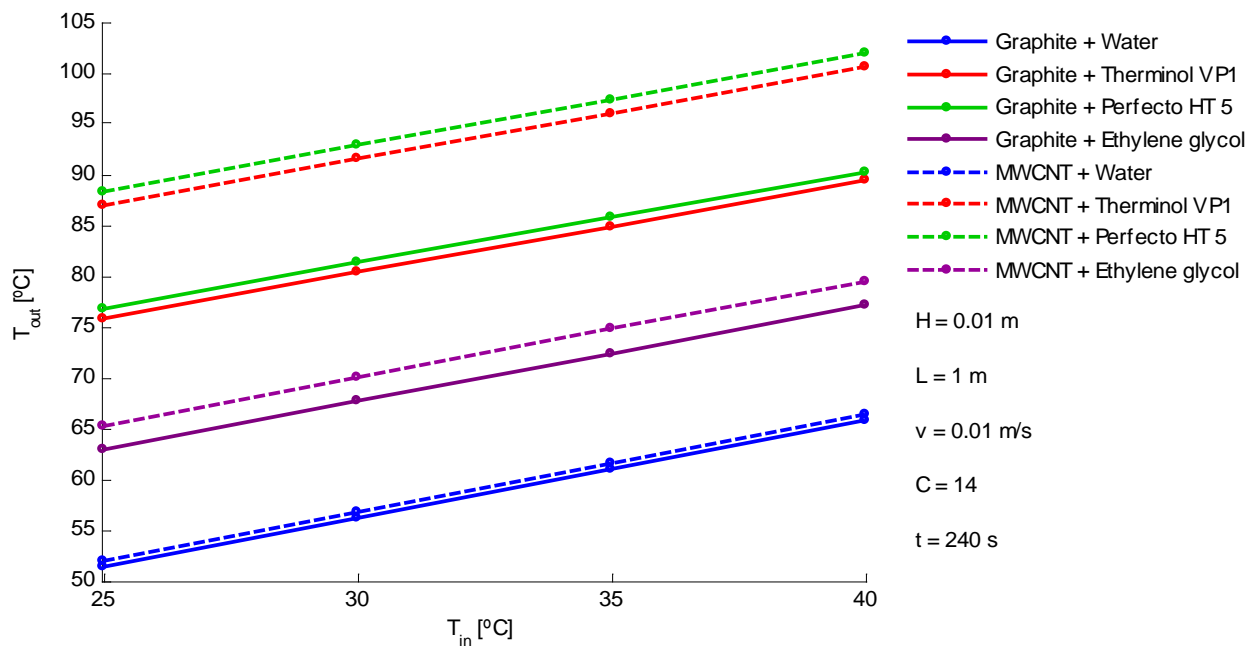


Figure 6.11 – Inlet temperature impact on the outlet temperature for different nanofluids

With respect to efficiency, a decrease is expected due to higher losses when inlet temperature increases. Considering a constant ambient temperature (25°C) and incident solar radiation (C=14), Figure 6.12 shows that this decrease is not pronounced (less than 2%) and similar slopes were obtained for the various nanofluids.

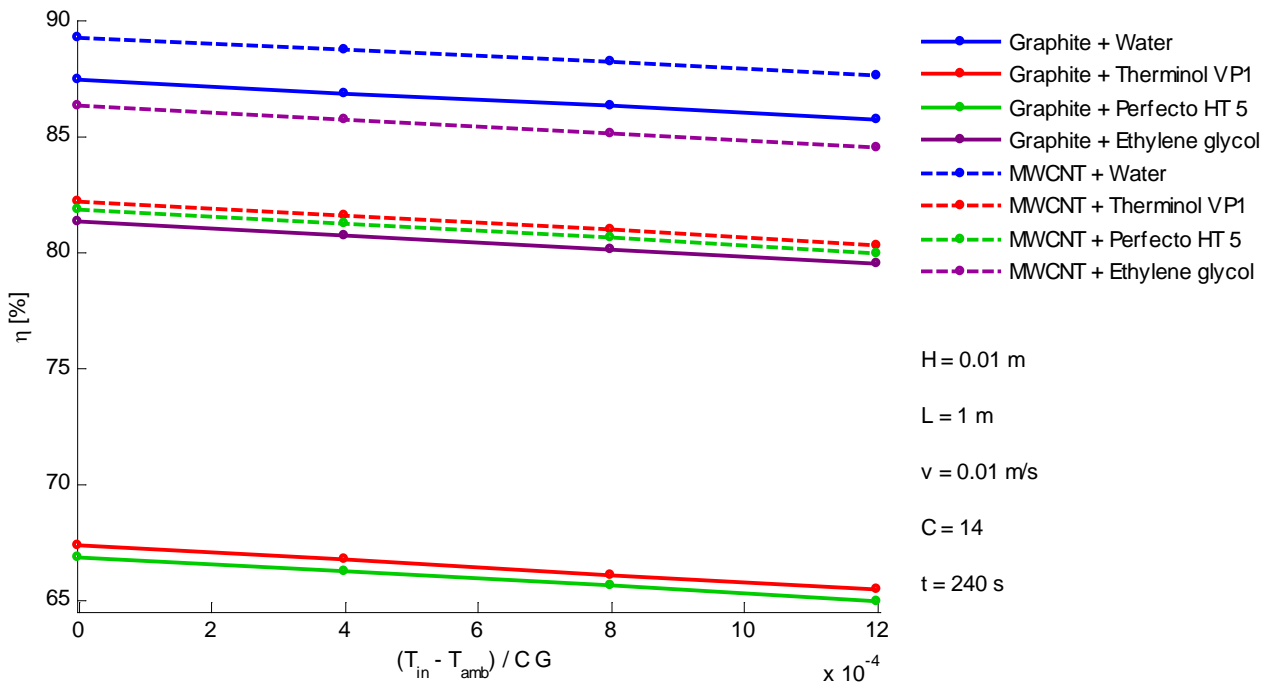


Figure 6.12 – Inlet temperature impact on the receiver efficiency for different nanofluids

Although a high performance was obtained, where a horizontal line represents an ideal performance and a higher slope implies a lower performance, for solar concentration factors under 14, the impact of the inlet temperature may severely decrease the efficiency of the receiver. As an example, Figure 6.13 shows that for an inlet temperature of 40°C, the predicted efficiency of graphite nanoparticles dispersed in water decreases approximately 15% when the solar concentration factor is reduced from 14 to 1.

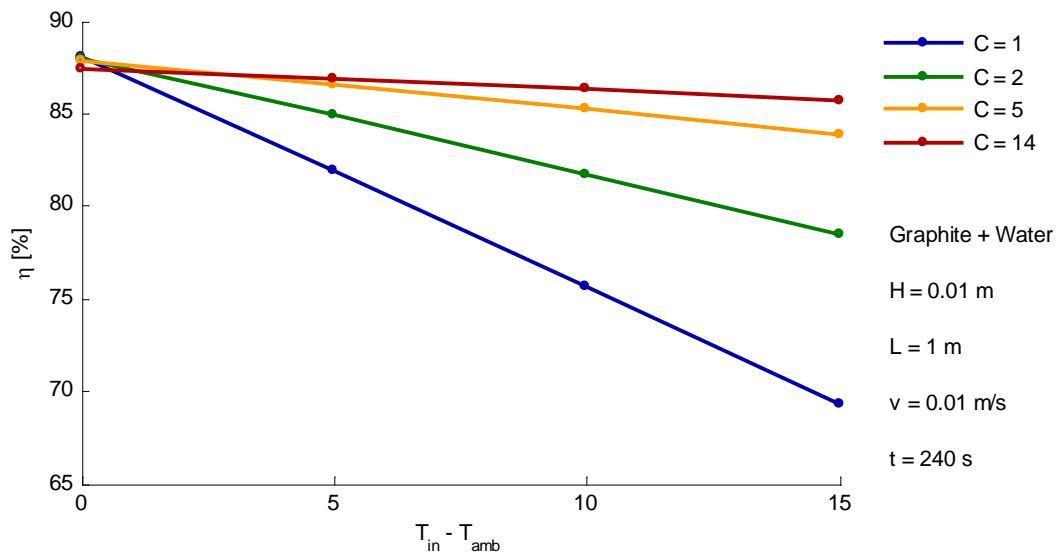


Figure 6.13 – Inlet temperature impact on the receiver efficiency for different radiation levels

According to S. A. Kalogirou [33] a typical flat plate collector under 1000 W/m^2 has the same efficiency of 70% for a 15°C difference between the inlet and ambient temperatures. However, the maximum efficiency is 80% as opposed to the one obtained for a volumetric receiver of 88%. Similar studies have also been carried out by other authors, as for example, H. Tyagi and P. Phelan [8] in which the order of magnitude of the efficiency for a low temperature nanofluid-based receiver containing water and aluminum nanoparticles is the same as the one obtained in this study for water-based nanofluids. However, it is important to highlight that these efficiencies may vary according to the geometry and the environmental and flow conditions. Note that, in Figure 6.6 the higher temperatures were obtained at the top surface of the receiver. Although the performance may vary, the opposite situation can be obtained by:

- **Reducing:** the height of the receiver, the inlet velocity, and the absorption efficiency.
- **Increasing:** the solar radiation level, the thermal losses at the top surface, the inlet temperature, and the receiver length.

As an example, Figure 6.14 shows the temperature profile at different points of the receiver length when changing some of the previous parameters. Now, when looking at the outlet boundary of the receiver, not only does the temperature increase over time, but its maximum value approaches the middle of the receiver height. Note that higher velocities also occur at the middle of the receiver, thus, increasing efficiency. At the last instant, it was shown that for a particular set of conditions, the temperature at the bottom is higher than that at the top of the receiver.

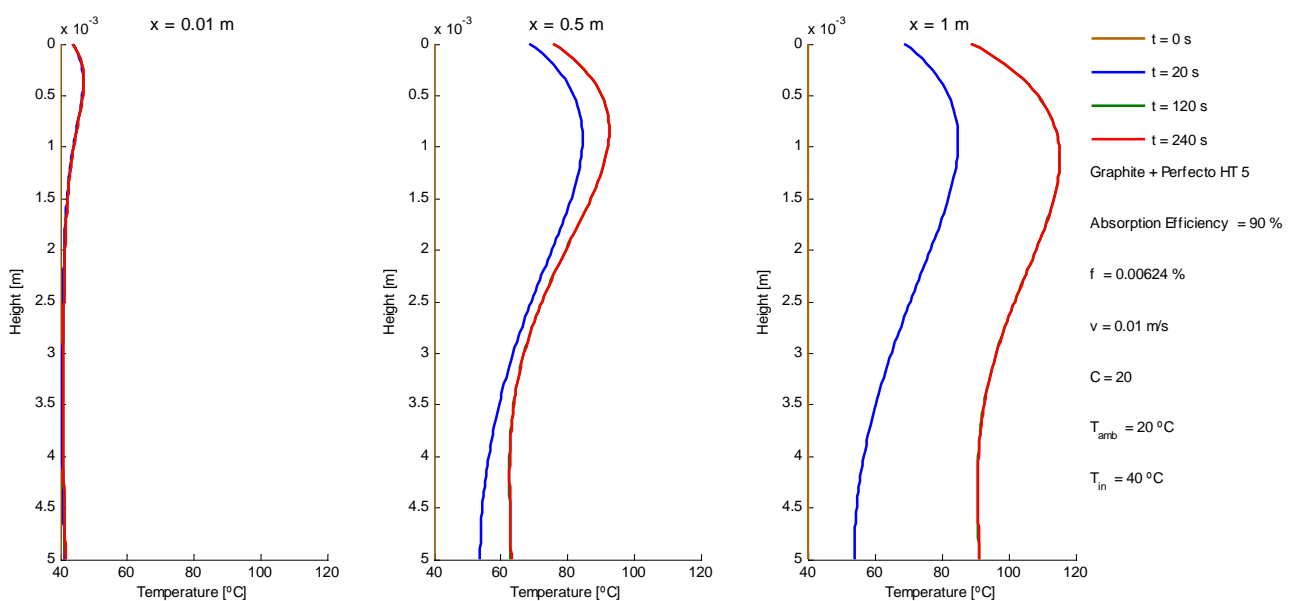


Figure 6.14 – Temperature profile in transient regime at different points of the receiver length

7. CONCLUSIONS AND FUTURE WORK

In the present work, nanofluid-based solar receivers have been investigated. These systems work on the principle of direct absorption of the solar radiation by a nanofluid through scattering and absorption mechanisms. A one-dimensional numerical model was developed to predict the temperature profile and performance for both selective surface-based and nanofluid-based receivers in a non-flowing receiver. The nanofluid-based systems have proven to distribute thermal energy more efficiently when compared to conventional collectors, in which heat transfer mechanisms to the working fluid are made through conduction and convection (indirect absorption). The numerical model was also used to explore the influence of varying the nanoparticle volume fraction, receiver height, and solar concentration factor on the efficiency of the system. The optimal conditions in which volumetric collectors perform the best were determined. However, under comparable operating conditions, the performance of the two types of receivers turned out to be very similar. Simultaneously, an experimental setup was arranged with the purpose of measuring the temperature profiles in a cylindrical receiver containing graphite and MWCNT suspensions in water and thermal oil, where results show good agreement with the numerical model results.

A two-dimensional numerical model was developed to simulate a volumetric flow receiver in which MWCNT presented a better performance, up to 15%, when compared to graphite nanoparticles. Nanofluid-based receivers also proved to have, under specific circumstances, a higher performance than the ones characteristic of surface-based receivers.

One can conclude that the primary contribution of this dissertation has been to emphasize the potential of harvesting solar energy through a nanofluid receiver based on direct absorption. Furthermore, although some simplifications were made in order to reduce the complexity, other contributions to the development of this technology can be accomplished since the numerical and experimental models allow different geometry configurations to be applied and/or different nanofluids to be tested. To what concerns the numerical model, some improvements can be made in the future to obtain more realistic results, such as, to consider convection on the non-flowing receiver, and to investigate the influence on performance of the thermo-physical properties variation with temperature. The study on the impact of the nanoparticle size diameter could also give an important contribution to the enhancement of solar energy collection. Future work in the development of an experimental apparatus for a volumetric flow receiver will allow the validation

of the numerical model created. Another interesting study that is worth carrying out is to take advantage of the low emissivity values, that are a characteristic feature of selective surfaces, and apply them on volumetric receivers. That is, to investigate the benefits of having nanofluids with selective coated nanoparticles. This is particularly important in the case of nanoparticle suspensions using gases as base fluid. A different approach from the one used in the optimization of the volume fraction, is to develop a model in which the solar radiation that is not absorbed by the nanofluid, is reflected from the bottom of the receiver. With this model, the volume fraction may be reduced without compromising the performance of the receiver and with the advantage of increasing volumetric heat release in the inner core of the fluid flow.

8. REFERENCES

- [1] M. A. Sadique, A. Verma, *Nano Fluid-based Receivers for Increasing Efficiency of Solar Panels*, International Journal of Advanced Mechanical Engineering 4 (2014) 77-82.
- [2] A. Lenert, E. N. Wang, *Optimization of nanofluid volumetric receivers for solar thermal energy conversion*, Solar Energy 86 (2012) 253-265.
- [3] O. Mahian, A. Kianifar, S. A. Kalogirou, I. Pop, S. Wongwises; *A review of the applications of nanofluids in solar energy*, International J. of Heat and Mass Transfer 57 (2013) 582-594.
- [4] A. Veeraragavan, A. Lenert, B. Yilbas, S. Al-Dini, E. Wanga, *Analytical model for the design of volumetric solar flow receivers*, Int. Journal of Heat and Mass Transfer 55 (2012) 556-564.
- [5] T. Otanicar, P. E. Phelan, R. S. Prasher, G. Rosengarten, R. A. Taylor, *Nanofluid-based direct absorption solar collector*, Journal of Renewable and Sustainable Energy 2, 033102 (2010).
- [6] V. Khullar, H. Tyagi, N. Hordy, T. Otanicar, Y. Hewakuruppu, P. Modi, R. A. Taylor, *Harvesting solar thermal energy through nanofluid-based volumetric absorption systems*, International Journal of Heat and Mass Transfer 77 (2014) 377-384.
- [7] A. Lenert, *Nanofluid-based Receivers for High Temperature, High-flux Direct Solar Collectors*, Masters Degree, Massachusetts Institute of Technology, June 2010.
- [8] H. Tyagi, P. Phelan, *Predicted efficiency of a low-temperature nanofluid-based direct absorption solar collector*, Journal of Solar Energy Engineering Vol. 131(4) (2009) p.041004 (Pre-Print).
- [9] R. Nasrin, M. A. Alim, *Performance of nanofluids on heat transfer in a wavy solar collector*, International Journal of Engineering, Science and Technology Vol. 5 No. 3 (2013) 58-77.
- [10] V. Khullar, H. Tyagi, *Solar Energy Harvesting Using Nanofluids-Based Concentrating Solar Collector*, Journal of Nanotechnology in Engineering and Medicine Vol. 3(3) (2012) p.031003.
- [11] D. C. Hernandez Aita, *Design and Optimization of volumetric solar receivers based on nanoparticles with supercritical CO₂*, Masters Degree, Delft University of Technology, 2014.
- [12] T. Otanicar and J. Golden, *Comparative Environmental and Economic Analysis of Conventional and Nanofluid Solar Hot Water Technologies*, Environ. Sci. Technol. 43 (2009) 6082-6087.
- [13] V. Khullar and H. Tyagi, *A study on environmental impact of nanofluid-based concentrating solar water heating system*, Int. J. of Environmental Studies, Vol. 69, No. 2, (2012) 220-232.

- [14] E. E. S. Michaelides, *Nanofluidics – Thermodynamic and transport properties*, Springer, 2014.
- [15] S. Mukherjee, S. Paria, *Preparation and Stability of Nanofluids - A Review*, Journal of Mechanical and Civil Engineering, Volume 9, Issue 2 (2013) 63-69.
- [16] A. Ghadimi, R. Saidur, H. Metselaar, *A review of nanofluid stability properties and characterization in stationary conditions*, International Journal of Heat and Mass Transfer 54 (2011) 4051-4068.
- [17] D. Incropera, L. Bergman, *Fundamentals of heat and mass transfer*, Wiley, sixth edition.
- [18] EASTMAN - Datasheet Therminol VP-1, group provoc T.B.S 10-04 (12/98) E.
<http://www.therminol.com/products/Therminol-VP1> (04/02/2015).
- [19] Castrol Limited - Datasheet Perfecto HT 5
[http://msdspds.castrol.com/bpglis/FusionPDS.nsf/Files/B7854044333136898025779600301F92/\\$File/Perfecto%20HT_5.pdf](http://msdspds.castrol.com/bpglis/FusionPDS.nsf/Files/B7854044333136898025779600301F92/$File/Perfecto%20HT_5.pdf) (04/02/2015).
- [20] GrafTech International Holdings Inc - *Advanced Graphite Powders*, 2013.
- [21] K. V. Mantena, *Electrical and mechanical properties of MWCNT filled conductive adhesives on lead free surface finished PCB's*, University of Kentucky Master's Theses, 2009.
- [22] N. R. Pradhan, H. Duan, J. Liang, G. S. Iannacchione, *The specific heat and effective thermal conductivity of composites containing single-wall and multi-wall carbon nanotubes*, Nanotechnology 20 (2009) 245705 (7pp).
- [23] The engineering toolbox - http://www.engineeringtoolbox.com/ethylene-glycol-d_146.html (15/03/2015).
- [24] Z. Said, M. H. Sajid, R. Saidur, M. Kamalisarvestani, N. A. Rahim, *Radiative properties of nanofluids*, International Communications in Heat and Mass Transfer 46 (2013) 74-84.
- [25] M. Modest, *Radiative Heat Transfer*, McGraw-Hill, second edition, 2003.
- [26] ASD, Inc - <http://www.asdi.com/products/fieldspec-spectroradiometers> (10/11/2014).
- [27] Lowel - Light Manufacturing, Inc - <http://lowel.tiffen.com/prolight/index.html> (10/11/2014).
- [28] KARTELL - <http://www.kartell.com/> (15/02/2015).

- [29] G. M. Hale, M. R. Querry, *Optical Constants of Water in the 200-nm to 200- μ m Wavelength Region*, Vol 12, 1973.
- [30] ASTM G173-03(2012), *Standard Tables for Reference Solar Spectral Irradiances: Direct Normal and Hemispherical on 37° Tilted Surface*, ASTM International, West Conshohocken, PA, 2012. (<http://www.astm.org/Standards/G173.htm>).
- [31] S. D. Conte, C. Boor, *Elementary Numerical Analysis - An Algorithmic approach*, McGraw-Hill, third edition, New York, 1980.
- [32] A. Bejan, *Heat Transfer*, John Wiley & Sons, 1994.
- [33] S. A. Kalogirou, *Solar Energy Engineering – Processes and systems*, first edition, 2009.
- [34] CAMPBELL SCIENTIFIC, INC - *CR10 measurement and control module operator's manual*, 1996.
- [35] CAMPBELL SCIENTIFIC, INC - <https://www.campbellsci.com/cr10x-ordering> (05/01/2015).
- [36] LABFACILITY, Ltd - *The new labfacility temperature handbook*, 2006;
<http://www.labfacility.co.uk/temperature-process-technology-downloads.html> (05/01/2015).
- [37] The Eppley Laboratory, Inc -
http://www.eppleylab.com/instrumentation/black_white_pyranometer.htm (05/01/2015).
- [38] ISO 9060-1990, *Solar energy - Specification and classification of instruments for measuring hemispherical solar and direct solar radiation*, 1990.
- [39] ISO 9847-1992, *Solar energy - Calibration of field pyranometers by comparison to a reference pyranometer*, 1992.
- [40] ASTM E490-00a(2014), *Standard Solar Constant and Zero Air Mass Solar Spectral Irradiance Tables*, ASTM International, West Conshohocken, PA, 2014. (<http://www.astm.org/Standards/E490.htm>).
- [41] IS 12762-9 (2010): Photovoltaic Devices, Part 9: Solar Simulator Performance Requirements.
- [42] H. Ferreira, M. Rangel, *Nanotechnology: general aspects and potential applications in catalysis*, Química Nova Vol. 32 no. 7 (2009)
- [43] NanoLab, Inc. - <http://www.nano-lab.com> (05/01/2015).
- [44] Branson - <http://www.bransoninc.com/en/product-features> (12/03/2015).

- [45] John D. Anderson, *Computational fluid dynamics*, McGRAW-Hill, New York, 1995.
- [46] A. Djurišić, E. Li, *Optical properties of graphite*, J. of Applied Physics 85 (1999) 7404-7410.
- [47] T. P. Otanicar, P. E. Phelan, J. S. Golden, *Optical properties of liquids for direct absorption solar thermal energy systems*, Solar Energy 83 (2009) 969–977.
- [48] H. El-Kashef, *The necessary requirements imposed on polar dielectric laser dye solvents*, Physica B 279 (2000) 295-301.
- [49] S. Lee and S. P. Jang, *Extinction coefficient of aqueous nanofluids containing multi-walled carbon nanotubes*, International Journal of Heat and Mass Transfer 67 (2013) 930-935.

9.APPENDIX

I. Radiative and optical properties of base fluids and nanoparticles

A. Graphite

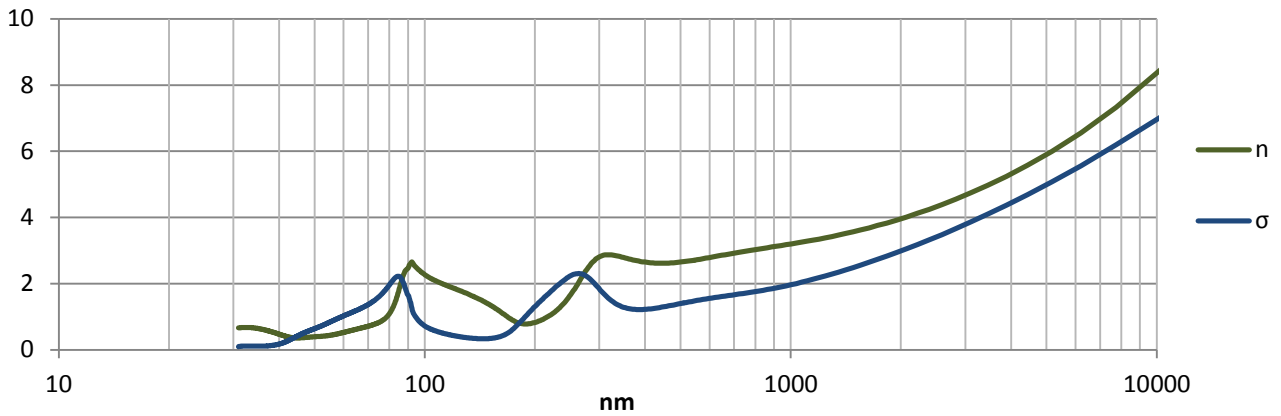


Figure 9.1 – Refractive index (n) and extinction coefficient (σ) of graphite [46]

B. Therminol VP1

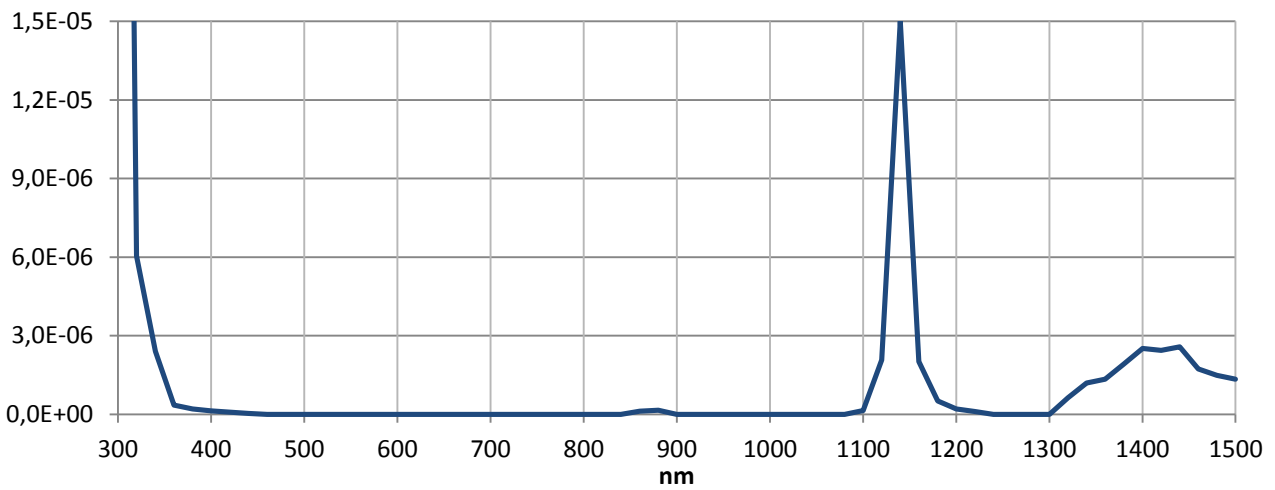


Figure 9.2 – Extinction coefficient (σ) of Therminol VP1 [47]

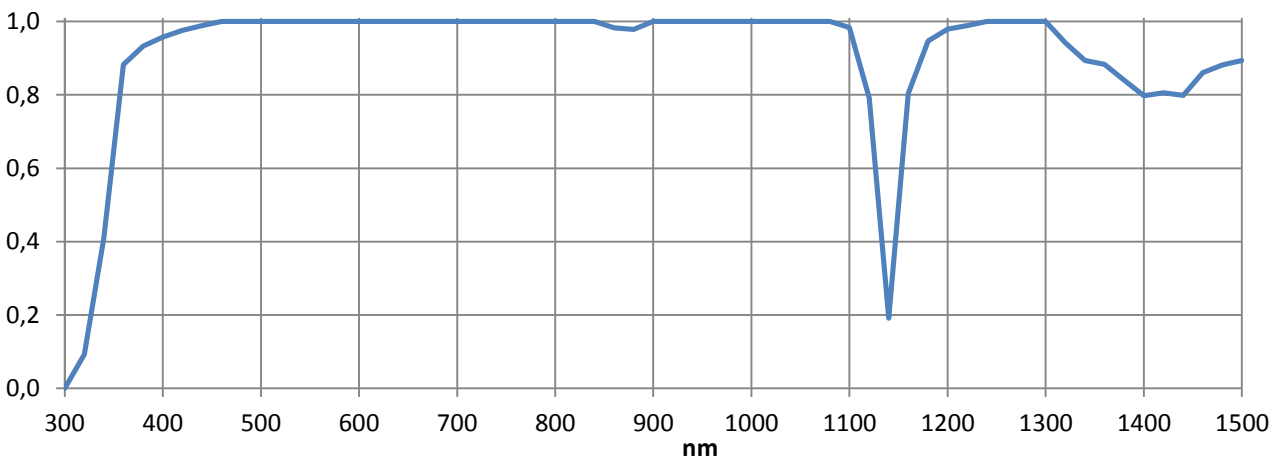


Figure 9.3 – Transmissivity (τ) of Therminol VP1 using Eq. (2.11)

C. Water

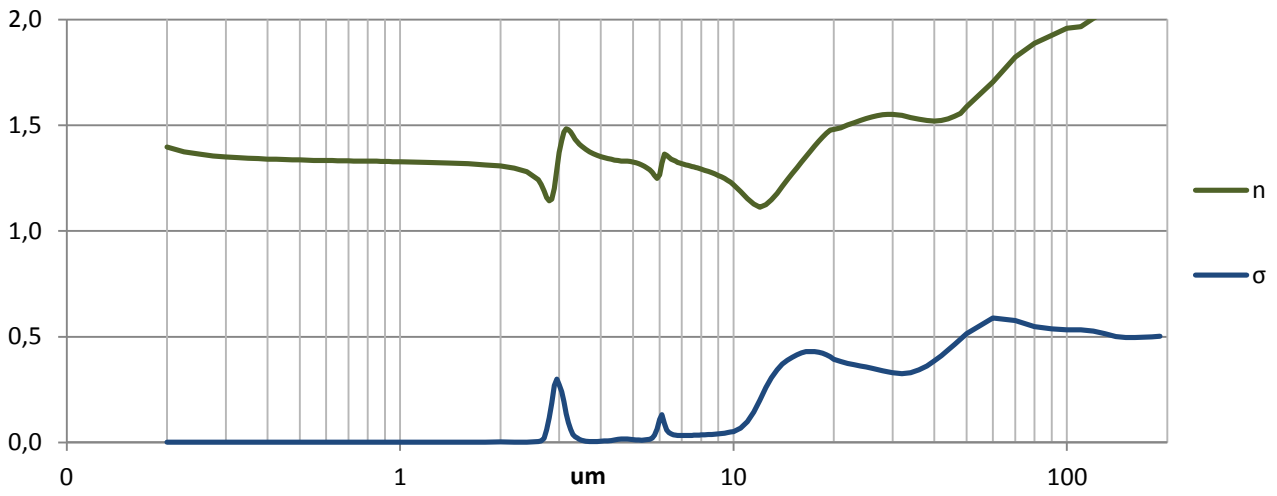


Figure 9.4 – Refractive index (n) and extinction coefficient (σ) of water [29]

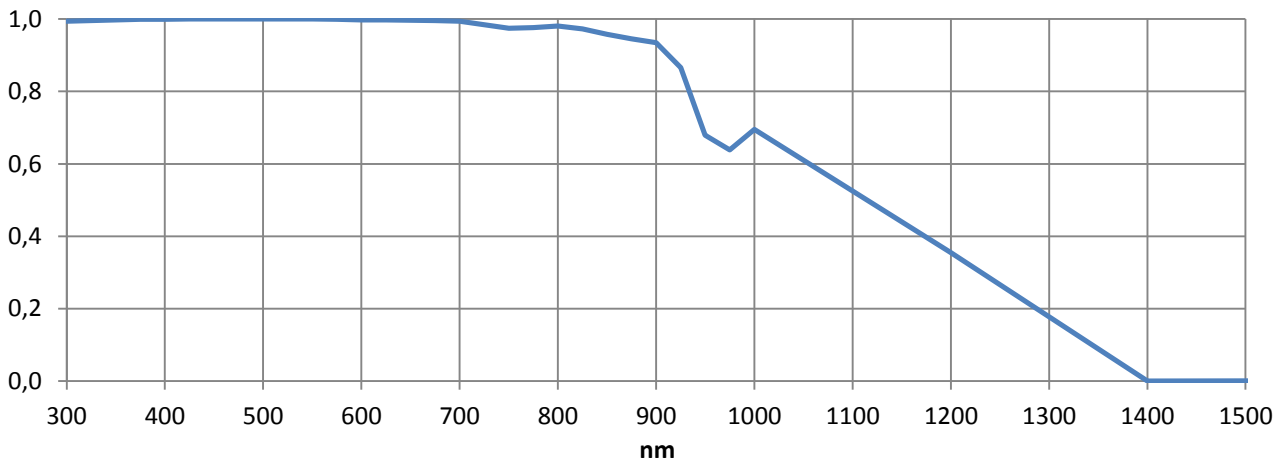


Figure 9.5 – Transmissivity (τ) of water using Eq. (2.11)

D. Ethylene Glycol

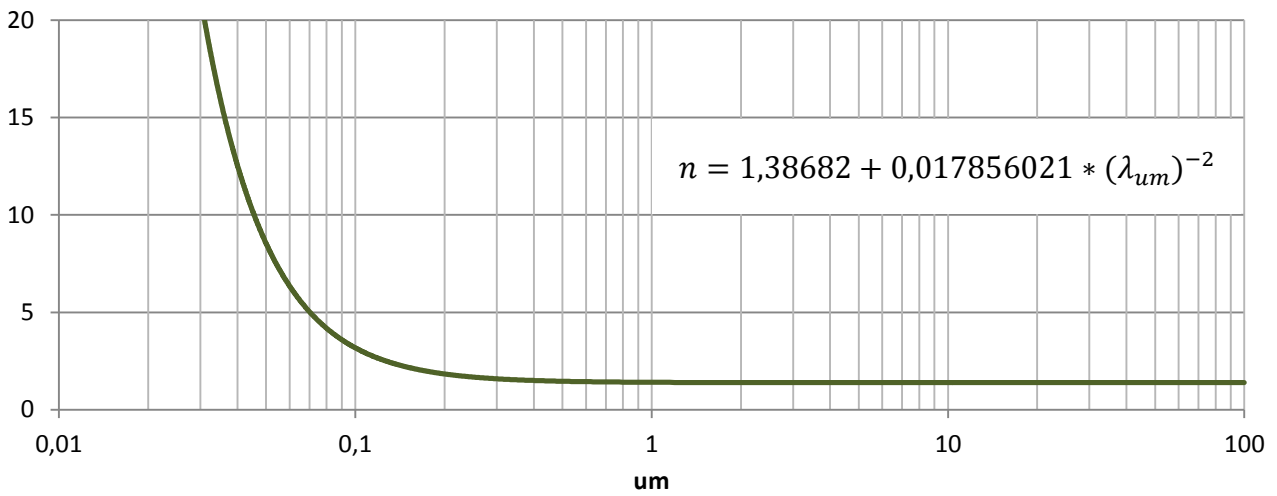


Figure 9.6 – Refractive index (n) of ethylene glycol [48]

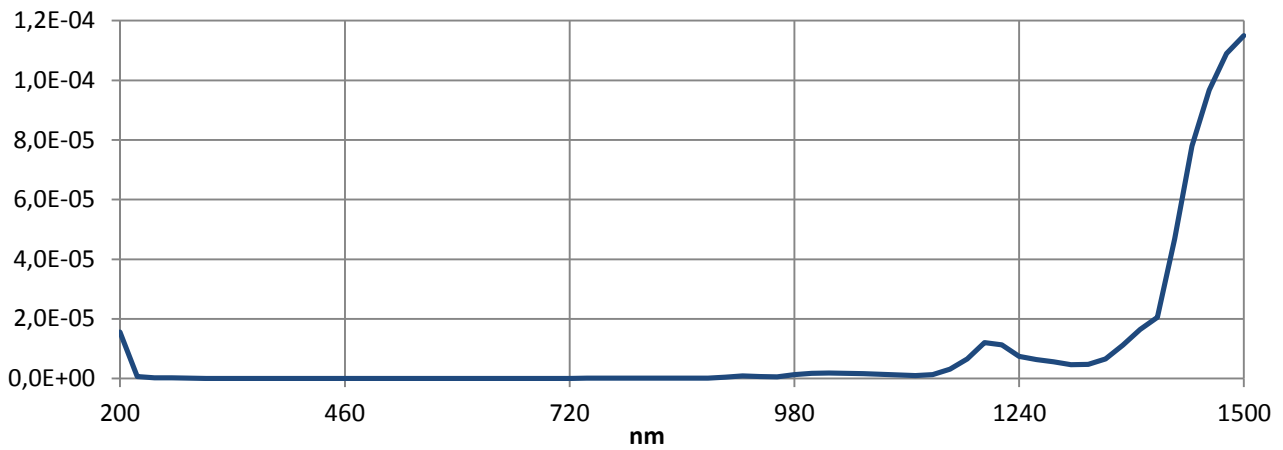


Figure 9.7 – Extinction coefficient (σ) of ethylene glycol [47]

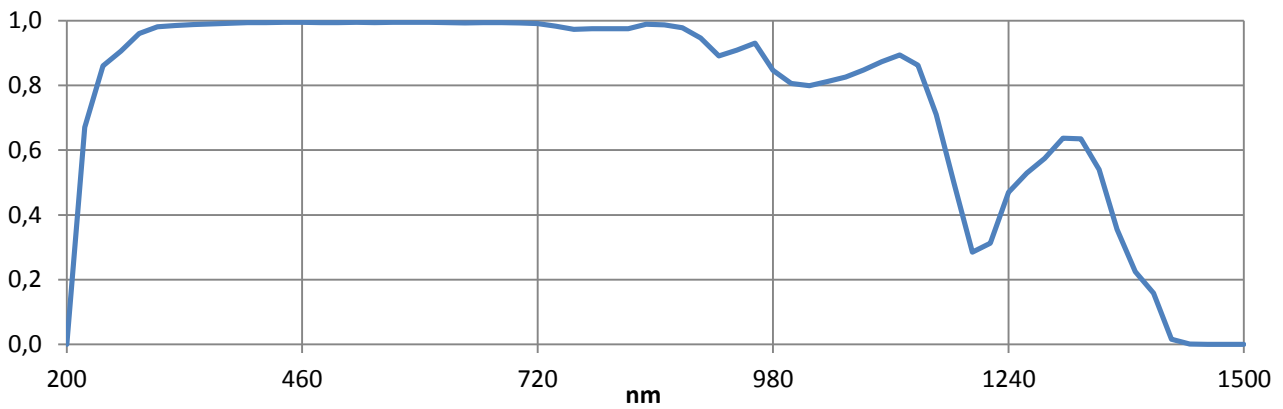


Figure 9.8 – Transmissivity (τ) of ethylene glycol using Eq. (2.11)

E. MWCNT

- The absorption coefficient values were obtained from experimental results carried out by S. Lee and S. P. Jang [49] for a fixed wavelength of 632,8 nm.
- The refractive index was considered to be the same as graphite.

II. RS3 software

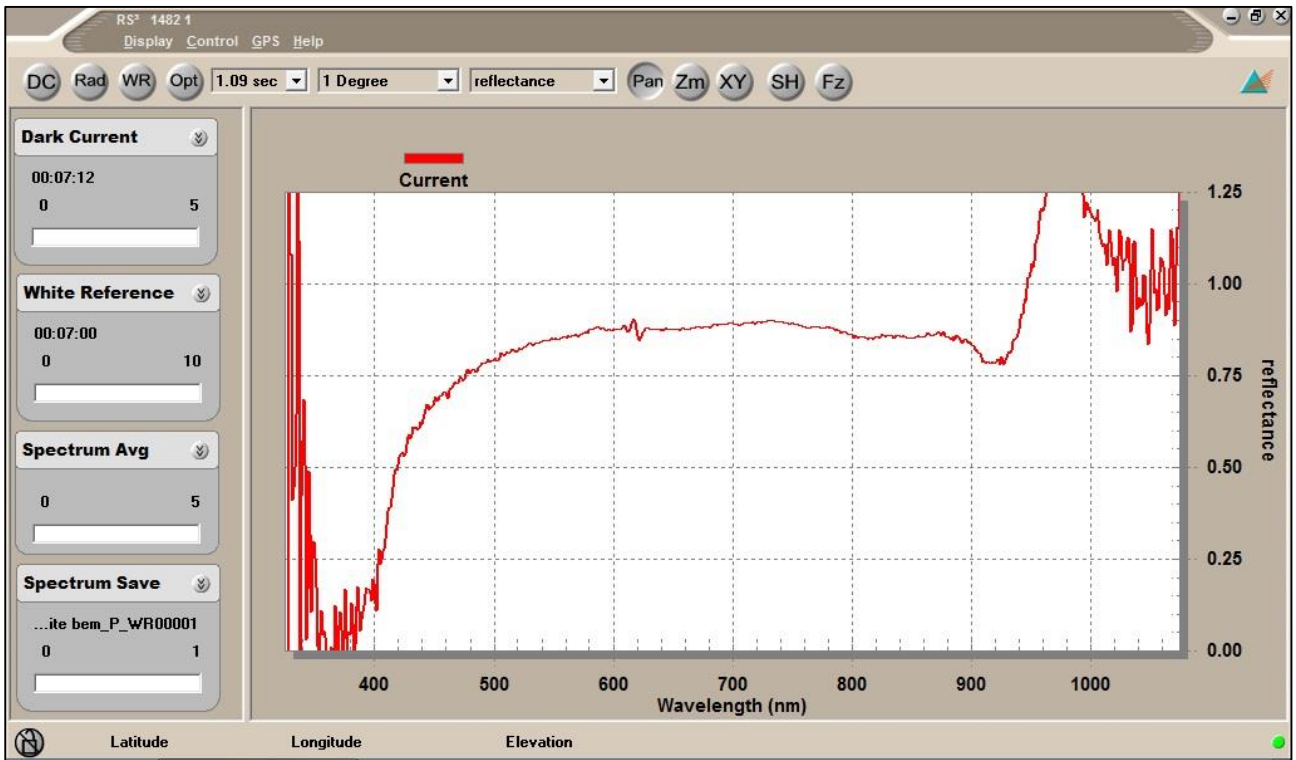


Figure 9.9 – Print screen of the RS3 software for spectrophotograms collection

III. Remarks on the explicit method

• Numerical residual in the q''' calculation

As referred before, when calculating the temperature distribution on y direction, the continuous spatial domain was discretized on a finite domain. For that reason, the values of heat generation (q''') were considered to be equal on a small volume around each point of the mesh. This approximation can significantly influence both temperatures and efficiencies. Thus, reducing the space between each point (Δy) will reduce volume and result in the decrease of the numerical error. As a consequence, this reduction may lead to a substantial increase in computation time to fully solve the numerical model. To quantify this numerical error, parameter R , also called residual, can be calculated in the following way:

$$R = \left| 1 - \frac{\sum_j^{n_j} q_j''' V_j}{\eta_{abs} C G A} \right| \quad (9.1)$$

Where C times G is the total incident radiation, A is the area perpendicular to solar radiation ($\Delta x \Delta w$), and V_j is the volume as function of height position. Note that for internal points, volume equals $\Delta x \Delta y \Delta w$, but at the top and bottom surfaces, volume equals $\Delta x \Delta y \Delta w / 2$. Therefore, the previous equation can be rewritten in the following way:

$$R = \left| 1 - \frac{q_{j=1}''' \frac{\Delta y}{2} + \sum_{j=2}^{n_j-1} q_j''' \Delta y + q_{j=n_j}''' \frac{\Delta y}{2}}{\eta_{abs} C G} \right| \quad (9.2)$$

In this form, R represents the relative numerical error, so it varies between zero and one. If the heat absorbed (based on the mesh geometry) equals the maximum solar radiation that can be volumetrically absorbed due to the presence of a given volume of suspended nanoparticles, R becomes null. The numerical error will increase if the estimated heat absorbed is greater or smaller than the actual heat absorption. It is also important to note that this error is the same regardless the solar concentration factor.

• **Numerical residual in the calculation of temperature**

Due to the discretization carried out to implement the explicit method, the numerical error associated with the calculation of the temperature distribution can be quantified by balancing the calculated absorbed energy, the theoretical absorbed energy and the estimated losses to environment:

$$R = |E''_{abs} - (\eta_{abs} C G t - Q''_p)| \quad (9.3)$$

which can also be calculated in terms of percentage as follows:

$$R [\%] = 100 \left| 1 - \frac{(\eta_{abs} C G t - Q''_p)}{E''_{abs}} \right| \quad (9.4)$$

where,

$$E''_{abs} = \sum_j^{nj} \rho(j) c_p(j) (T_f(j) - T_i(j)) \Delta y \quad (9.5)$$

$$Q''_p = \sum_k^{nk} (h_{conv}(k) + h_{rad}(k)) (T_f(k+1) - T_i(1)) \Delta t \quad (9.6)$$

The numerical error may vary with the increase of solar concentration factor.

IV. Remarks on the Newton's method

This method is commonly used in numerical analysis to find an approximate value of a function's root. Considering as an example, that we want to determine the volume fraction for a given absorption efficiency of 95% in the case of a nanofluid composed by suspended graphite nanoparticles and Therminol VP1 thermal oil. A possible function could be the difference between the desired absorption efficiency (95%) and the calculated absorption efficiency as function of the volume fraction ($F(f_n)$). For a fixed receiver height, this function has the following behaviour:

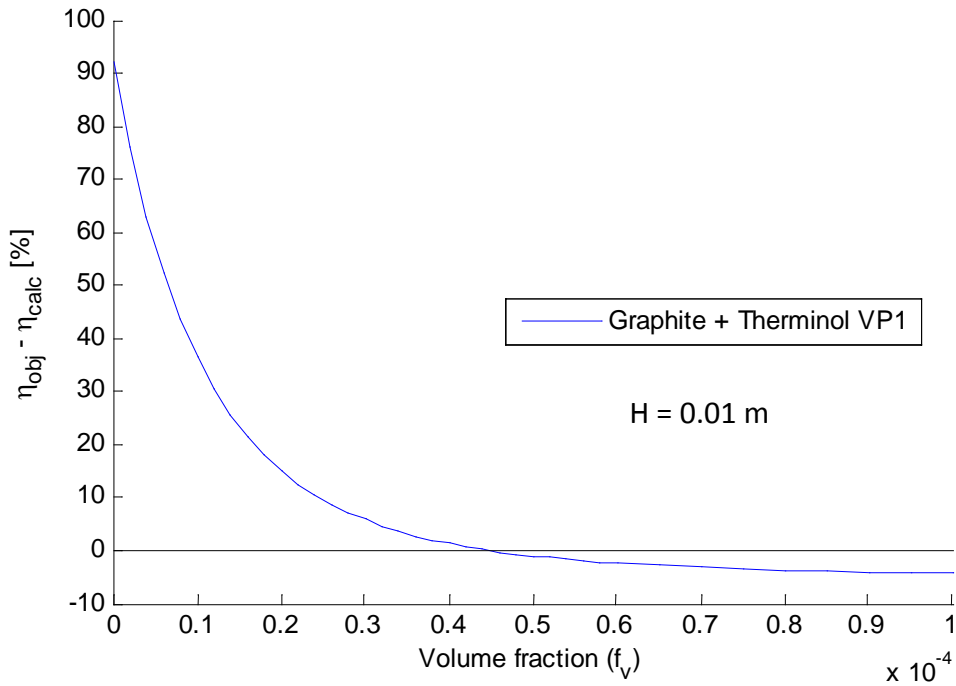


Figure 9.10 – Function for volume fraction optimization through the Newton method

When the function equals zero ($F(f_n) = 0$), it means that the calculated absorption efficiency is equal to the desired absorption efficiency (95%) and thus, the value of the volume fraction is determined. However, it is very hard to successfully achieve a volume fraction value that would result in an absorption efficiency of 95%, or it would take an excessive amount of calculations to determine the absorption efficiency for every volume fraction until the objective is reached. When applying Newton's method, an initial guess of the volume fraction value (f_n) has to be attributed. Then, using the expression below [31], the function is approximated by its tangent line (derivative), and the next volume fraction value (f_{n+1}) will be generated.

$$f_{n+1} = f_n - \frac{F(f_n)}{F'(f_n)} \quad (9.7)$$

The derivative can be calculated as an approximate value using a finite difference method:

$$F'(f_n) \approx \frac{F(f_n + \Delta x) - F(f_n)}{\Delta x} \quad (9.8)$$

In Figure 9.11 (a), the function $F(f_n)$ is shown in blue, and the tangent line in black. It is possible to see that f_{n+1} is closer to the solution than f_n . This process should be done again in the same exact way, but the next value f_{n+2} will be based on the previous value f_{n+1} , and so on, until a convergence criterion is fulfilled (b).

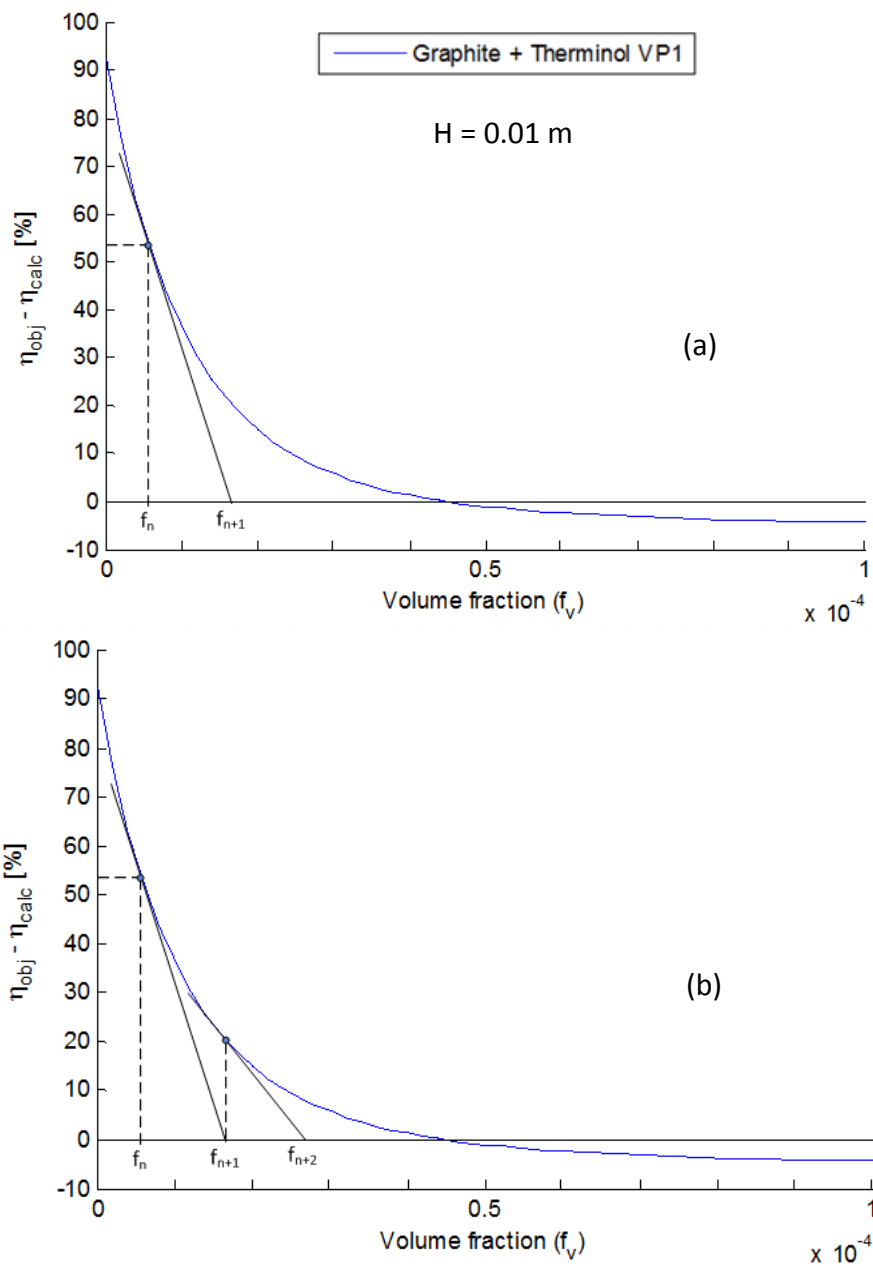


Figure 9.11 – Newton's method implementation

A possible convergence criterion for this case could be given by the step value ($f_{n+1} - f_n$) decrease. That is, if the difference between the next value and the previous one is smaller than a given tolerance, the iteration process should stop and the solution is considered to be achieved.

Changing the terms position in Eq. (9.7), we can find the step value difference:

$$f_{n+1} = f_n - \frac{F(f_n)}{F'(f_n)} \Leftrightarrow f_{n+1} - f_n = -\frac{F(f_n)}{F'(f_n)} \quad (9.9)$$

the convergence criterion could be:

$$|f_{n+1} - f_n| < tolerance \quad \text{or} \quad \left| -\frac{F(f_n)}{F'(f_n)} \right| < tolerance$$

Newton's method is a very effective and accurate iterative process to estimate the root of a given function, however, there are some constraints regarding its convergence, especially if a complex function is at stake. Not only can the initial guess of the volume fraction determine how fast the solution is obtained, it can also determine if convergence is accomplished or not. In this particular case of study, volume fraction can't be negative. Another reason for non-convergence lies on the function's derivability. For example, when increasing volume fraction, the limit of the calculated absorption efficiency is 100% (as shown in Figure 3.8) so the function becomes constant at -5% (95%-100%). This means that the derivative is null and so, Newton's method can't be used if values of volume fraction are higher than the ones that make the function constant.

V. Datalogger (CR10) programming

The screenshot displays the CR10 datalogger programming interface, divided into several sections:

- Progress:** A vertical list of steps: 1. New/Open, 2. Datalogger, 3. Sensors, 4. Outputs, 5. Finish.
- Wiring:** Options for 'Wiring Diagram' and 'Wiring Text'.
- Selected Sensors:** A table listing sensors and their measurements.

Sensor	Measurement
CR10	
Default	BattV
...	ProgSig
AM416	
1 Type T TC ...	Temp_C_1
2 Type T TC ...	Temp_C_2
3 Type T TC ...	Temp_C_3
4 Type T TC ...	Temp_C_4
5 Type T TC ...	Temp_C_5
6 Type T TC ...	Temp_C_0
7 Type T TC ...	Temp_C_6
8 Type T TC ...	Temp_C_7
9 Type T TC ...	Temp_C_8
10 Type T TC ...	Temp_C_9
11 Type T T...	Temp_C_10
12 Type T T...	Temp_C_11
13 Type T T...	T_amb
HalfBr3W	Rs_R0
VoltsDiff	Rad
User Entered	T_ref
- Processing Options:** A vertical stack of buttons: Average, ETo, Maximum, Minimum, Sample, StdDev, Total, WindVector.
- Selected Outputs:** Configuration for Array ID (101) and Scan Interval (5.0000 Seconds).

Sensor	Measurement	Processing	Output Label	Units
Default	n/a	n/a	Year_RTM	
			Day_RTM	
			Hour_Minu	
Type T TC	T_amb	Average	T_amb_AV	Deg C
User Enter	T_ref	Average	T_ref_AVG	
Type T TC	Temp_C_1	Average	Temp_C_1	Deg C
Type T TC	Temp_C_2	Average	Temp_C_2	Deg C
Type T TC	Temp_C_3	Average	Temp_C_3	Deg C
Type T TC	Temp_C_4	Average	Temp_C_4	Deg C
Type T TC	Temp_C_5	Average	Temp_C_5	Deg C
Type T TC	Temp_C_6	Average	Temp_C_6	Deg C
Type T TC	Temp_C_7	Average	Temp_C_7	Deg C
Type T TC	Temp_C_8	Average	Temp_C_8	Deg C
Type T TC	Temp_C_9	Average	Temp_C_9	Deg C
Type T TC	Temp_C_10	Average	Temp_C_1	Deg C
Type T TC	Temp_C_11	Average	Temp_C_1	Deg C
VoltsDiff	Rad	Average	Rad_AVG	W/m_2

Figure 9.12 – Programming window of CR10

VI. Solar simulator

To obtain collimated rays with the desired radiation spectrum, some components may be added between the lamp and the target area. The first component that should be added to the system is a set of optical integrators. Using this type of lenses will contribute significantly to the beam uniformity. The next component is usually a radiation filter, in this case, to allow only the spectral radiation matching the AM1.5 Global distribution to get through. Then, a light shutter enables to block or let radiation continue its optical path. However, light is not parallel, so a collimator should be added. A possible solar simulator could have a configuration as shown in Figure 9.13, in which the geometry and distances may vary due to the focal length of the lenses. A mirror (either ellipsoidal or spheric) is also commonly used near the lamp in order to increase light intensity directed toward to the target area.

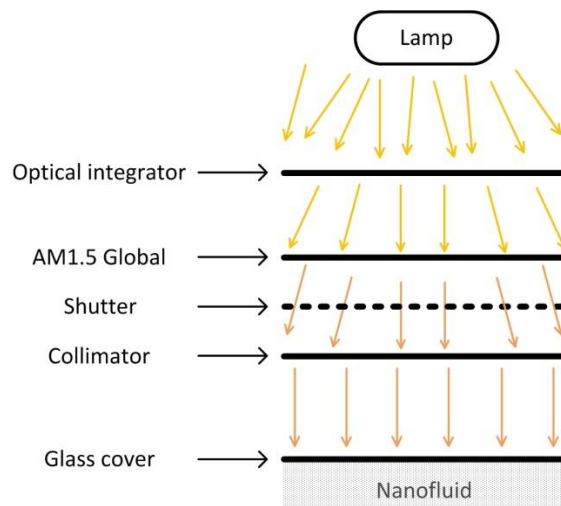


Figure 9.13 – Solar simulator components

As mentioned before, a glazing interface between the ambient and the nanofluid should exist to protect the nanofluid from external factors that could potentially damage it. Although this glazing does not take part of the solar simulator components, it may distort the spectrum distribution of the incoming radiation. This can be avoided by using a low reflectance glass with a constant transmittance over a large range of the radiation wavelengths, such as fused silica or quartz.